ALMA MATER STUDIORUM
UNIVERSITÀ DI BOLOGNA

Facoltà di Scienze Matematiche, Fisiche e Naturali
Dipartimento di Astronomia

Dottorato di Ricerca in Astronomia
Ciclo XXIII

# HYDRODYNAMICAL SIMULATIONS OF GALAXY CLUSTERS IN DARK ENERGY COSMOLOGIES

Tesi di Dottorato
di
**Cristiano DE BONI**

Coordinatore:
Prof.
**Lauro MOSCARDINI**

Relatori:
Prof.
**Lauro MOSCARDINI**
Dott.
**Stefano ETTORI**

Esame Finale Anno 2012

SCUOLA DI DOTTORATO IN SCIENZE MATEMATICHE, FISICHE E ASTRONOMICHE
Settore Concorsuale: 02/C1 – Astronomia, Astrofisica, Fisica della Terra e dei Pianeti
Settore Scientifico-Disciplinare: FIS/05 – Astronomia e Astrofisica

*A Bologna*
*alle torri*

# Contents

# Introduction

During the 20th century, our understanding of the Universe has significantly improved thanks to some discoveries that have become milestones of science. From a cosmological point of view, among that, the most important are 1916 Einstein's General Relativity, Lemaître's discovery and Hubble's confirmation of the Universe expansion in the late '20s and the 1964 detection of the cosmic microwave background (CMB) radiation by Penzias and Wilson. Einstein's theory unveiled the intrinsic connection between the geometry of spacetime and its matter-energy content, which ended in the formulation of the Friedmann-Robertson-Walker (FRW) model of the Universe. At the time, the Universe was thought to be static, and since the general solution of Einstein's equation is either an expanding or a contracting universe, Einstein's artificially added a cosmological constant term in order to obtain a static solution. Beside the fact that such a solution is unstable, the addition of a cosmological constant term was also unnecessary because, as discovered by Lemaître and Hubble, the Universe is indeed expanding. Still, for a twist of fate, this term, even if with a completely different meaning, is nowadays part of the concordance cosmological model. The discovery of the expansion of the Universe was an outstanding result, obtained by mixing up theoretical expectations from General Relativity and astronomical observations. Indeed, the observed redshift of nearby galaxies could have in principle been explained as a local phenomenon, but, thanks to the underlying theory, it was correctly interpreted as a general property of the Universe. The great question about the expansion of the Universe was linked to the fact that, if it is nowadays expanding, it should be contracting going back in time. If this is the case, then in the very first instants it should have been concentrated in a high-density/high-temperature small region, and now we should see the relics of these times in the actual Universe. The missing piece was found by Penzias and Wilson that, while searching for a completely different thing, observed an isotropic, diffuse radiation in the radio-wavelengths at 3K, interpreted as the background radiation cooled down by the expansion of the Universe. Along with other important discoveries, these three findings were the basis of the so-called hot Big Bang model.

One of the crucial parameter of the FRW model is the total matter-energy density of the Universe, in particular in relation to a quantity known as critical density, because the ratio of the two indicates if the Universe is open, closed or flat, *i.e.* if it will expand forever, it will eventually stop its expansion and then recollapse, or it will keep on expanding but with an asymptotically zero velocity. It had been known since the '30s, thanks to Zwicky and Smith, that luminous matter was not sufficient to explain the dynamical behaviour of galaxies and galaxy clusters. Thus, the presence of an electromagnetically non-interacting dark matter component had already been supposed at those times. Even the discovery of a hot, X-ray emitting plasma in the '60, which had a great impact on the study of galaxy clusters, was not sufficient to explain the dynamical missing mass, and so dark matter is still considered to be a major component of the total matter-energy budget of the Universe. Now the point is, how much matter is there in the Universe? It had been already known from

studies on galaxy clusters that a low matter density universe was favoured over a high matter density universe. Following results from CMB experiments also showed that the Universe was almost flat, thus highlighting a discrepancy between the need to have an almost critical density and the low matter density requirements from observations of astrophysical objects. In between, the discovery from Type Ia supernovae (SN Ia) observations that the Universe expansion is accelerating, opened a new possibility to fill the missing matter-energy density with a component responsible for this accelerated expansion.

Over the last decade great observational evidence (Riess et al., 1998; Perlmutter et al., 1999; Jarosik et al., 2011; Vikhlinin et al., 2009b) has shown that at the present time the Universe is expanding at an accelerated rate. This fact can be attributed to a component with negative pressure, which is usually referred to as dark energy, that today accounts for about 3/4 of the entire energy budget of the Universe. The simplest form of dark energy is a cosmological constant term $\Lambda$ in Einstein's equation, within the so-called $\Lambda$CDM cosmologies. Though in good agreement with observations, a cosmological constant is theoretically difficult to understand in view of the fine-tuning and coincidence problems. A valid alternative consists in a dynamical dark energy contribution that changes in time and space, often associated to a scalar field (the 'cosmon' or 'quintessence') evolving in a suitable potential (Wetterich, 1988; Ratra & Peebles, 1988). Dynamical dark energy allows for appealing scenarios in which the scalar field is the mediator of a fifth force, either within scalar-tensor theories or in interacting scenarios (Wetterich, 1995; Amendola, 2000; Boisseau et al., 2000; Pettorino & Baccigalupi, 2008; Mota et al., 2008, and references therein). In view of future observations, it is of fundamental interest to investigate whether dark energy leaves some imprints in structure formation, giving a practical way to distinguish among different cosmologies, as recently investigated in Hu & Sawicki (2007); Baldi et al. (2010), Zhao et al. (2010), Baldi (2011), Baldi & Pettorino (2011) and Wintergerst et al. (2010).

The dark energy problem is nowadays studied through many different methods, ranging from CMB observations (the outstanding results of the WMAP satellite are the basis of modern cosmology) to SN Ia studies, from galaxy cluster analysis to the promising baryonic acoustic oscillations (BAOs) technique. These methods provide in general orthogonal probes for the different cosmological parameters, and thus they are complementary one to each other. In Fig. 1 we show some recent results taken from Vikhlinin et al. (2009b), where it is clear that the combined use of different methods can significantly improve the quality of the constraints that we can put on the cosmological parameters. Despite these successful results, there can be degeneracies among different cosmological models. For example, deviations from the predicted $\Lambda$CDM mass function can be the results of a simple quintessence model, of a model in which there is a coupling between dark energy and gravity or between dark energy and dark matter, of primordial non gaussianities in the power spectrum or of some form of warm dark matter (*e.g.* neutrinos). To disentangle these degeneracies, it is fundamental to study other properties of the different sources of cosmological information.

In this work, we study the general properties of galaxy clusters in different dark energy cosmologies. Galaxy clusters are the largest virialized objects in the Universe and are considered to be a fair sample of the overall matter distribution of the Universe itself. They contain a large amount of gas in the form of diffused ionized plasma known as intracluster medium (ICM), which emits in the X-ray band. The X-ray properties of galaxy clusters such as luminosity and temperature trace the total mass of the cluster itself, and hence can be used to study global properties of these objects. A lot of observational work (*Chandra*, *XMM-Newton*) has been made in recent years, and future missions (*e.g.* Athena, eROSITA, WFXT) are under study to improve the characterization of these objects in the X-rays. The

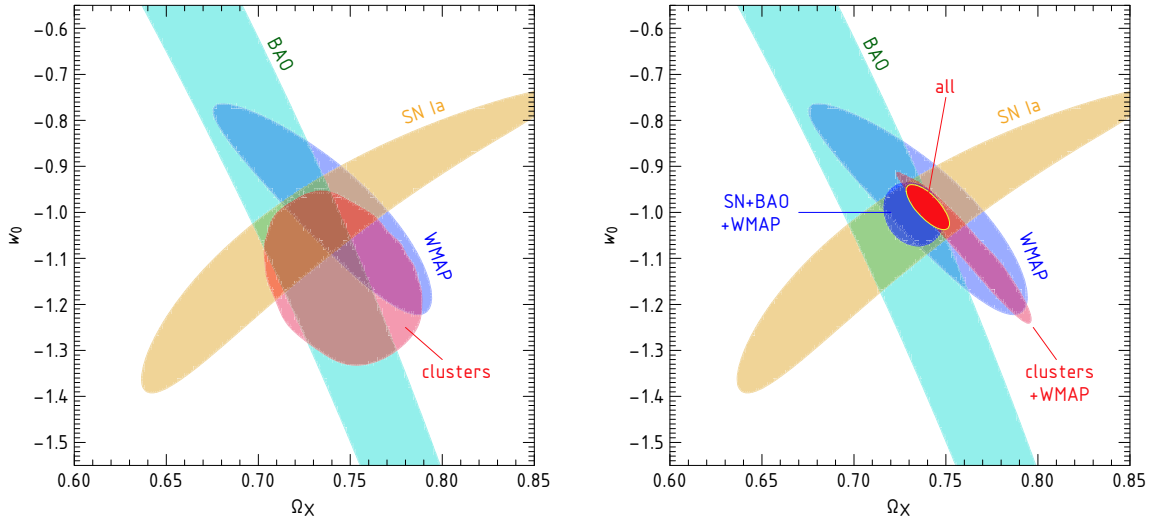


Figure 1: (Left panel) Comparison of the dark energy constraints from X-ray clusters and from other individual methods (SNe, BAOs, and WMAP). (Right panel) Dark energy constraints in a flat universe from the combination of all cosmological data sets. From Vikhlinin et al. (2009b).

properties of galaxy clusters, in particular their mass, can be investigated also in the optical region of the spectrum through gravitational lensing, which gives independent estimates from X-rays. Galaxy clusters are well suited for cosmological studies and their complex structure leave space to study the effect of different dark energy models on their internal properties, such as the concentration.

Since galaxy clusters occupy the highly non-linear regime of structure formation, we need numerical simulations to follow their evolution from a theoretical point of view. In this work we present the *Padme* simulation set, a set of $N$-body and hydrodynamical simulations of galaxy clusters in different dark energy cosmologies. This is the first set of cosmological simulations to treat baryon physics in extended quintessence models.

The work is organized as follows. In Chapter 1 we introduce and discuss the different dark energy models under investigation, namely a reference ΛCDM cosmology, two ordinary quintessence models and two extended quintessence models. In Chapter 2 we describe galaxy clusters both from a theoretical and an observational point of view, starting from the theory of structure formation and concluding with the observed X-ray quantities. After introducing the *Padme* simulation set, in Chapter 3 we discuss the general properties of the halos extracted from this set, in particular the mass function, the X-ray quantities and the baryon fraction. Chapter 4 is dedicated to the study of the concentration-mass ($c - M$) relation, with special attention to the role of baryons and dark energy in modifying the predictions for dark matter in ΛCDM. We discuss our results in Conclusions.

# Chapter 1

# Dark Energy

In this chapter we will present the different dark energy models under investigation in this work, namely a concordance ΛCDM model (Section 1.1), two models with dynamical dark energy, viewed as a quintessence scalar field (using a RP and a SUGRA potential form) (Section 1.2) and two extended quintessence models (EQp and EQn) where the quintessence scalar field interacts non-minimally with gravity (scalar-tensor theories) (Section 1.3). As a reference, we will also briefly discuss coupled quintessence (CQ) models, where the quintessence scalar field is coupled to dark matter (Section 1.4). Finally, we will compare some features of EQ and CQ models (Section 1.5). Useful references on these models can be found in Amendola & Tsujikawa (2010) and Pettorino & Baccigalupi (2008). For the derivation of the equations of General Relativity see Appendix A. In the following of the chapter, where not otherwise specified, we set $\hbar = c = 1$.

In General Relativity, the geometry of the Universe is linked to the matter-energy content of the Universe itself through the Einstein equation

$$G_{\mu\nu} \equiv R_{\mu\nu} - \frac{1}{2} R g_{\mu\nu} = 8\pi G T_{\mu\nu} \ . \tag{1.1}$$

The Einstein equation can be derived from the variation of the Hilbert action

$$S = \frac{1}{2\kappa} S_H + S_M = \int d^4x \left( \frac{1}{2\kappa} \sqrt{-g} R + \mathcal{L}_M \right) \tag{1.2}$$

with respect to the metric which is given, in an homogeneous and isotropic universe, by the Robertson-Walker metric

$$ds^2 = dt^2 + a^2(t) \left[ \frac{dr^2}{1 - kr^2} + r^2 (d\theta^2 + \sin^2 \theta d\phi^2) \right] \ , \tag{1.3}$$

where $a(t)$ is the scale factor and $k$ is the curvature of the universe[1].
The redshift $z$ is linked to the scale factor $a$ through

$$z = \frac{a_0}{a} - 1 \ , \tag{1.4}$$

[1] See equation (A.39)

where $a_0$ is the present time value of the scale factor and it is usually set $a_0 = 1$.
The general equations describing the evolution of a homogeneous and isotropic universe are the Friedmann equations

$$\frac{\dot{a}^2}{a^2} = \frac{8\pi G}{3}\rho - \frac{k}{a^2} \tag{1.5}$$

and

$$\frac{\ddot{a}}{a} = -\frac{4\pi G}{3}(\rho + 3p) \ , \tag{1.6}$$

that can be cast in the form

$$H^2 = H_0^2 \left[ \sum_i \Omega_{0i} \exp\left( -3 \int_{a_0}^{a} \frac{1 + w_i(a')}{a'} da' \right) + \left( \frac{a_0}{a} \right)^2 (1 - \sum_i \Omega_{0i}) \right] \tag{1.7}$$

and

$$\dot{H} + H^2 = -\frac{H_0^2}{2} \sum_i \Omega_{0i}(1 + 3w_i) \exp\left( -3 \int_{a_0}^{a} \frac{1 + w_i(a')}{a'} da' \right) \ . \tag{1.8}$$

Here, the Hubble parameter is defined as $H \equiv \dot{a}/a$ (where the dot denotes the derivative with respect to the cosmic time $t$), $\Omega_{0i} \equiv \rho_{0i}/\rho_{0c}$ is the current density parameter of the $i$-th component of the universe, $\rho_{0c} \equiv 3H_0^2/8\pi G$ is the critical density at the present time, $w_i$ is the equation of state parameter of the $i$-th component ($w_i \equiv p_i/\rho_i$) and the sum is taken over all components. The first term in equation (1.7) includes densities associated to each constituent of the universe while the second term accounts for any possible deviation from flat geometry.
The continuity equation

$$\dot{\rho} + 3H(\rho + p) = 0 \tag{1.9}$$

holds if the evolution of the universe is adiabatic.

For our Universe, there are three pieces of observational evidence:

- (a) the Universe is flat, *i.e.* $k = 0$ and $\sum_i \Omega_{0i} = 1$ ;
- (b) the Universe is now expanding at an accelerated rate, *i.e.* $\dot{a}_0 > 0$ and $\ddot{a}_0 > 0$ ;
- (c) $\Omega_{0m} \simeq 0.27$, *i.e.* matter is not nowadays dominating.

From (a):

$$H^2 = \frac{\dot{a}^2}{a^2} = \frac{8\pi G}{3}\rho = H_0^2 \sum_i \Omega_{0i} \exp\left( -3 \int_{a_0}^{a} \frac{1 + w_i(a')}{a'} da' \right) \ . \tag{1.10}$$

Thus equation (1.8) can be written as

$$\dot{H} = -4\pi G(\rho + p) \ . \tag{1.11}$$

From (b) and (c): there exists a *dark energy* (DE) component which nowadays dominates ($\Omega_{0\mathrm{DE}} \simeq 0.73$) and such that

$$\rho_{0\mathrm{DE}} + 3p_{0\mathrm{DE}} < 0 \ . \tag{1.12}$$

From continuity equation (1.9), this implies

$$-1 < w_{\mathrm{DE}} < -\frac{1}{3} \tag{1.13}$$

in order not to have $\dot{\rho}_{\mathrm{DE}} > 0$ (*phantom dark energy*).

We can assume that the Universe is constituted by three different components: matter [baryons and cold dark matter (CDM)], for which $w_m = 0$; radiation (photons plus relativistic matter) with $w_r = 1/3$, whose contribution is nowadays negligible as shown by CMB; dark energy (DE), which, in the simplest case, behaves as a fluid with negative $w_{\mathrm{DE}}$ and provides the present accelerated expansion of the Universe.
In Fig. 1.1 we show the evolution with redshift of the energy density of matter, radiation and dark energy ($\Omega_m$, $\Omega_r$, and $\Omega_\Lambda$, respectively) in four different cosmological models. As we will discuss in Chapter 2, structure formation is more important while $\Omega_m \approx 1$, because, in that epoch, positive density perturbations exceed the critical density. The redshift at which $\Omega_m$ equals $\Omega_r$ is earlier for larger present-day values of $\Omega_m$, while the redshift at which $\Omega_m$ starts to decline clearly depends on the dark energy model. Because structure formation is strongly influenced by these two epochs, observations of galaxy clusters evolution provide good opportunities to constrain $\Omega_m$, $\Omega_\Lambda$ and $w$.

The question we have to answer to is: what is the nature of dark energy?

For our analysis we will consider three possible sets of cosmological models. The first is the standard ΛCDM model, that we use as a reference model, where dark energy is represented by the cosmological constant. This model is in agreement with present observations, though theoretically it is intrinsically affected by fine-tuning and coincidence problems.
Alternatively, dark energy could be a dynamical component, seen as a quintessence scalar field rolling down a potential (Wetterich, 1988; Ratra & Peebles, 1988). If the scalar field is minimally coupled to gravity, this class of scenarios is still affected by fine-tuning and coincidence problems, as much as in the standard ΛCDM model. However it is interesting, for our analysis, to consider such dynamical cases, where a time varying equation of state is present. Numerical simulations of quintessential cold dark matter have been presented, for example, in Jennings et al. (2010).
More interestingly, the dynamical scalar field could be coupled to other species, as addressed in Wetterich (1995), Amendola (2000) and Pettorino & Baccigalupi (2008). We limit ourselves to the case in which the coupling involves universally all species, as it happens in scalar-tensor theories (Boisseau et al., 2000). The latter have been also investigated within $F(R)$ theories in Schmidt et al. (2009) and Oyaizu et al. (2008). $N$-body simulations of extended quintessence were studied in Li et al. (2011).

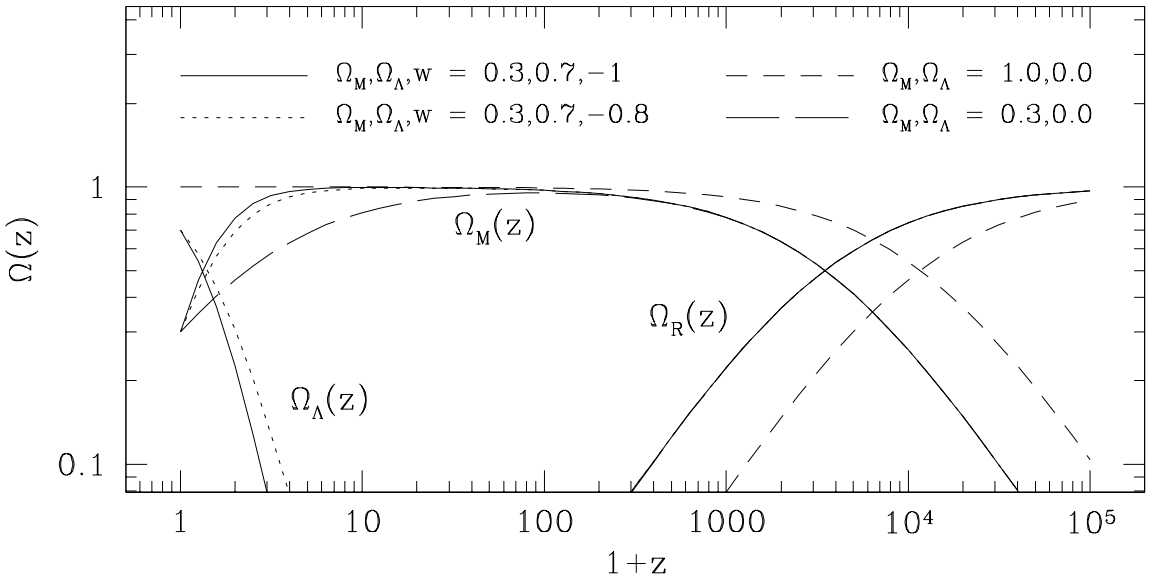


Figure 1.1: Evolution with redshift of $\Omega_m$, $\Omega_r$, and $\Omega_\Lambda$ in four different cosmological models: a concordance ΛCDM model with $\Omega_m = 0.3$, $\Omega_\Lambda = 0.7$, and $w = -1$ (solid lines); a flat dark energy model with $\Omega_m = 0.3$, $\Omega_\Lambda = 0.7$, and $w = -0.8$ (dotted lines); a flat universe model with $\Omega_m = 1$ and $\Omega_\Lambda = 0$ (short-dashed lines); an open universe model with $\Omega_m = 0.3$ and $\Omega_\Lambda = 0$ (long-dashed lines). From Voit (2005).

## 1.1 Cosmological Constant

The simplest candidate for dark energy is the cosmological constant Λ, which is so called because its energy density is constant in time and space. From continuity equation (1.9), this implies $w_\Lambda = -1$. The evolution of a ΛCDM universe is thus given by equation (1.10)

$$H^2 = H_0^2 \left[ \Omega_{0m} \left( \frac{a_0}{a} \right)^3 + \Omega_{0r} \left( \frac{a_0}{a} \right)^4 + \Omega_{0\Lambda} \right] = \tag{1.14}$$

$$= \frac{8\pi G}{3} \left[ \rho_{0m} \left( \frac{a_0}{a} \right)^3 + \rho_{0r} \left( \frac{a_0}{a} \right)^4 + \rho_{0\Lambda} \right] . \tag{1.15}$$

Since the metric $g_{\mu\nu}$ satisfies $\nabla^\mu g_{\mu\nu} = 0$, it is possible to add the term $\Lambda g_{\mu\nu}$ to the Einstein equation

$$G_{\mu\nu} \equiv R_{\mu\nu} - \frac{1}{2} R g_{\mu\nu} = 8\pi G T_{\mu\nu} - \Lambda g_{\mu\nu} = 8\pi G \tilde{T}_{\mu\nu} , \tag{1.16}$$

where

$$\tilde{T}_{\mu\nu} = T_{\mu\nu} - \frac{\Lambda}{8\pi G} g_{\mu\nu} = \tilde{\rho} u_\mu u_\nu + \tilde{p} (g_{\mu\nu} + u_\mu u_\nu) , \tag{1.17}$$

and

$$\tilde{\rho} = \rho + \rho_\Lambda = \rho + \frac{\Lambda}{8\pi G} , \tag{1.18}$$

$$\tilde{p} = p + p_\Lambda = p - \frac{\Lambda}{8\pi G} . \tag{1.19}$$

The Lagrangian density for the ΛCDM model is simply given by the linear term in $R$ plus $\Lambda$. Actually, the variation of the action

$$S = \int d^4x \left[ \frac{1}{2\kappa}\sqrt{-g}(R - 2\Lambda) + \mathcal{L}_M) \right] \tag{1.20}$$

with respect to the metric $g_{\mu\nu}$ yields equation (1.16) if $\kappa = 8\pi G$.[2]
Using equations (1.18) and (1.19), equation (1.6) can be rewritten

$$\frac{\ddot{a}}{a} = -\frac{4\pi G}{3}(\rho + 3p) + \frac{\Lambda}{3} , \tag{1.21}$$

where it is clear that $\Lambda$ works as a repulsive force against gravity.

The matter density $\rho_m$ coincides with the cosmological density $\rho_\Lambda$ at

$$z_{coinc} = \left( \frac{\Omega_{0\Lambda}}{1 - \Omega_{0\Lambda}} \right)^{1/3} - 1 , \tag{1.22}$$

which, for $\Omega_{0\Lambda} \simeq 0.73$, is $z_{coinc} \approx 0.4$. The fact that dark energy started to dominate only at very recent times, suggesting that we are now in a particular moment in the history of the Universe, is one of the criticisms moved against the ΛCDM model and goes under the name of *coincidence problem*.

In order to realize the cosmic acceleration today, the cosmological constant $\Lambda$ is required to be of the order of the square of the present-day Hubble parameter $H_0 = 100h$ km sec$^{-1}$Mpc$^{-1}$:

$$\Lambda \approx H_0^2 = (2.13h \times 10^{-42}\text{GeV})^2 . \tag{1.23}$$

In terms of energy density, it is equivalent to

[2]Indeed

$$\begin{aligned} \delta S &= \frac{1}{2\kappa}\int d^4x \left[\sqrt{-g}R_{\mu\nu}\delta g^{\mu\nu} + (R - 2\Lambda)\delta(\sqrt{-g}) + \sqrt{-g}g^{\mu\nu}\delta(R_{\mu\nu})\right] + \delta S_m = \\ &= \frac{1}{2\kappa}\int d^4x \left[\sqrt{-g}(R_{\mu\nu} - \frac{1}{2}Rg_{\mu\nu} + \Lambda g_{\mu\nu})\delta g^{\mu\nu} + \sqrt{-g}\nabla^\mu v_\mu\right] + \delta S_m = \\ &= \frac{1}{2\kappa}\int d^4x \left[\sqrt{-g}(R_{\mu\nu} - \frac{1}{2}Rg_{\mu\nu} + \Lambda g_{\mu\nu} - 8\pi G T_{\mu\nu})\delta g^{\mu\nu} + \sqrt{-g}\nabla^\mu v_\mu\right] \end{aligned}$$

if $\delta S_m$ is given by equation (A.22) with $\alpha_M = 2\kappa$.

$$\rho_\Lambda \approx \frac{\Lambda m_{pl}^2}{8\pi} \approx 10^{-47}\mathrm{GeV}^4 \ , \tag{1.24}$$

with $h \approx 0.7$ and Planck mass $m_{pl} = \sqrt{\hbar c/G} \approx 10^{19}$GeV.
If the dark energy comes from the vacuum energy $\langle\rho\rangle$ of an empty space then

$$\rho_{vac} \approx \frac{k_{max}^4}{16\pi^2} \ , \tag{1.25}$$

where $k_{max}$ is a cut-off scale.
Indeed, the zero-point energy of some field of mass $m$ with momentum $k$ and frequency $\omega$ is given by $E = \omega/2 = \sqrt{k^2 + m^2}/2$ (in units of $\hbar = c = 1$).
Summing over the zero-point energies of this field up to the cut-off scale $k_{max}$ ($\gg m$), we obtain the vacuum energy density

$$\rho_{vac} = \int_0^{k_{max}} \frac{d^3k}{(2\pi)^3}\frac{1}{2}\sqrt{k^2+m^2} \ . \tag{1.26}$$

Since the integral is dominated by the modes with large $k$ ($\gg m$), we find that

$$\rho_{vac} = \int_0^{k_{max}} \frac{4\pi k^2 dk}{(2\pi)^3}\frac{1}{2}\sqrt{k^2+m^2} \approx \frac{k_{max}^4}{16\pi^2} \ . \tag{1.27}$$

General Relativity is believed to be valid up to the Planck scale $m_{pl}$. Taking the cut-off scale $k_{max}$ to be $m_{pl}$, the vacuum energy density is

$$\rho_{vac} \approx 10^{74}\mathrm{GeV}^4 \ , \tag{1.28}$$

about $10^{121}$ times larger than the observed value.
For the QCD scale $k_{max} \approx 0.1$GeV we have $\rho_{vac} \approx 10^{-3}\mathrm{GeV}^4$, still much larger than $\rho_\Lambda$.
The fact that the observed value of $\Lambda$ is many orders of magnitude lower than the theoretical value of the vacuum energy density, but still non-zero, is another criticism moved against the $\Lambda$CDM model, and goes under the name of *fine-tuning problem*.

In the framework of dark energy, despite the fine-tuning and coincidence problems, the cosmological constant $\Lambda$ is still the simplest model that is able to explain the observational constraints. For some arguments in favor of the $\Lambda$CDM model see Bianchi & Rovelli (2010).

## 1.2 Quintessence

The second case that we consider here is that of a dynamical dark energy, given by a quintessence scalar field $\phi$ with an equation of state $w = w(a)$ (Wetterich, 1988; Ratra & Peebles, 1988). Quintessence is a canonical scalar field $\phi$ with a potential $V(\phi)$ responsible for the late-time cosmic acceleration. It interacts with all the other components only through standard gravity. The quintessence model is defined by the action

$$S = \int d^4x\sqrt{-g}\left[\frac{1}{2\kappa}R + \mathcal{L}_\phi + \mathcal{L}_{fluid}\right] \ , \tag{1.29}$$

where

$$\mathcal{L}_\phi = -\frac{1}{2}\partial^\mu\phi\partial_\mu\phi - V(\phi) \ , \tag{1.30}$$

and we have defined $\mathcal{L}_{fluid} \equiv \mathcal{L}_M/\sqrt{-g}$ .

The evolution of the scalar field $\phi$ is described by the Klein-Gordon equation[3]

$$\partial_\mu\partial^\mu\phi - \frac{\partial V(\phi)}{\partial\phi} = 0 \ . \tag{1.31}$$

The energy-momentum tensor of quintessence is given by

$$T_{\mu\nu\ [\phi]} = -\frac{2}{\sqrt{-g}}\frac{\delta(\sqrt{-g}\mathcal{L}_\phi)}{\delta g^{\mu\nu}} = \partial_\mu\phi\partial_\nu\phi - g_{\mu\nu}\left[\frac{1}{2}\partial^\rho\phi\partial_\rho\phi + V(\phi)\right] \ . \tag{1.32}$$

In a FRW background, the energy density and pressure of the field are

$$\rho_\phi = T_{00\ [\phi]} = \frac{1}{2}\dot{\phi}^2 + V(\phi) \tag{1.33}$$

and

$$p_\phi = a^{-2}T_{xx\ [\phi]} = \frac{1}{2}\dot{\phi}^2 - V(\phi) \tag{1.34}$$

respectively, which give the equation of state

$$w_\phi \equiv \frac{p_\phi}{\rho_\phi} = \frac{\dot{\phi}^2 - 2V(\phi)}{\dot{\phi}^2 + 2V(\phi)} \ . \tag{1.35}$$

The evolution of a quintessence universe is given by

$$H^2 = \frac{\kappa}{3}\left[\rho_{0m}\left(\frac{a_0}{a}\right)^3 + \rho_{0r}\left(\frac{a_0}{a}\right)^4 + \rho_\phi\right] \ , \tag{1.36}$$

where

$$\rho_\phi = \rho_{0\phi}\exp\left[-3\int_{a_0}^{a}\frac{1+w_\phi}{a'}da'\right] \ . \tag{1.37}$$

[3]See equation (A.31.)

Combining the continuity equation (1.9) with equations (1.33) and (1.34), the evolution of the quintessence scalar field is given by the Klein-Gordon equation

$$\ddot{\phi} + 3H\dot{\phi} + \frac{\partial V(\phi)}{\partial \phi} = 0 \ . \tag{1.38}$$

During radiation- or matter-dominated epochs, the energy density $\rho_M$ of the fluid dominates over that of quintessence, *i.e.* $\rho_M \gg \rho_\phi$. We require that $\rho_\phi$ tracks $\rho_M$ so that the dark energy density emerges at late times. In order to realize the late-time cosmic acceleration, we require that $w_\phi < -1/3$, which translate in the condition $\dot{\phi}^2 < V(\phi)$. Hence the scalar potential needs to be shallow enough for the field to evolve slowly along the potential.
We note from equation (1.35) that when the kinetic term $\dot{\phi}^2/2$ is negligible compared to the potential term $V(\phi)$, then $w_\phi \to -1$ and the ΛCDM case is recovered.
We consider "freezing models" in which the field was rolling along the potential in the past, but the motion gradually slows down after the system enters the phase of cosmic acceleration. The representative potentials that belong to this class are the so called Ratra-Peebles (RP) potential

$$V(\phi) = \frac{M^{4+\alpha}}{\phi^\alpha} \ , \tag{1.39}$$

with $\alpha > 0$ and its generalization, suggested by supergravity arguments, known as SUGRA potential

$$V(\phi) = \frac{M^{4+\alpha}}{\phi^\alpha} \exp(4\pi G\phi^2) \ . \tag{1.40}$$

The first potential does not possess a minimum and hence the field rolls down the potential towards infinity. The second potential has a minimum at which the field is eventually trapped (corresponding to $w_\phi = -1$).
Equation (1.36) can be expressed as

$$H^2 = \frac{\kappa}{3}\left[\rho_M + \frac{1}{2}\dot{\phi}^2 + V(\phi)\right] \ , \tag{1.41}$$

where $\rho_M = \rho_m + \rho_r$.
If we introduce the dimensionless variables

$$x \equiv \sqrt{\frac{\kappa}{6}}\frac{\dot{\phi}}{H} \ , \qquad y \equiv \sqrt{\frac{\kappa V}{3}}\frac{1}{H} \ , \tag{1.42}$$

then equation (1.41) can be written as

$$\Omega_M \equiv \frac{\kappa\rho_M}{3H^2} = 1 - \frac{\kappa}{6}\frac{\dot{\phi}^2}{H^2} - \frac{\kappa V}{3}\frac{1}{H^2} = 1 - x^2 - y^2 \ . \tag{1.43}$$

We also define the energy fraction of dark energy

$$\Omega_\phi \equiv \frac{\kappa\rho_\phi}{3H^2} = x^2 + y^2 \ . \tag{1.44}$$

Equation (1.11) can be written as

$$\dot{H} = -\frac{\kappa}{2}(\dot{\phi}^2 + \rho_M + p_M) = -\frac{\kappa}{2}\left[\dot{\phi}^2 + \rho_M(1+w_M)\right] \ , \tag{1.45}$$

and we obtain

$$\frac{\dot{H}}{H^2} = -\frac{\kappa}{2H^2}\dot{\phi}^2 - \frac{\kappa}{2H^2}\rho_M(1+w_M) = -3x^2 - \frac{3}{2}(1+w_M)(1-x^2-y^2) \ . \tag{1.46}$$

In that case, the effective equation of state is given by

$$\begin{aligned} w_{eff} &= \frac{\rho_{tot}}{p_{tot}} = 1 - \frac{2}{3}\frac{\dot{H}}{H^2} = 1 + 2x^2 + (1+w_M)(1-x^2-y^2) = \\ &= w_M + (1-w_M)x^2 - (1+w_M)y^2 \ . \end{aligned} \tag{1.47}$$

The equation of state of dark energy (1.35) can be expressed as

$$w_\phi = \frac{x^2 - y^2}{x^2 + y^2} \ . \tag{1.48}$$

Differentiating the variables $x$ and $y$ with respect to the number of e-foldings $N = \ln a$, we obtain

$$\frac{dx}{dN} = f(x, y, w_M, \lambda) \ , \tag{1.49}$$

$$\frac{dy}{dN} = g(x, y, w_M, \lambda) \ , \tag{1.50}$$

where

$$\lambda \equiv -\frac{1}{\sqrt{\kappa}}\frac{1}{V}\frac{\partial V}{\partial \phi} \ . \tag{1.51}$$

The quantity $\lambda$ characterizes the slope of the field potential, which obeys the following equation

$$\frac{d\lambda}{dN} = -\sqrt{6}\lambda^2(\Gamma - 1)x \ , \tag{1.52}$$

where

$$\Gamma \equiv \frac{V}{(\partial V/\partial\phi)^2}\frac{\partial^2 V}{\partial \phi^2} \ . \tag{1.53}$$

If $\lambda$ is constant, the cosmological dynamics can be well understood by studying fixed points of the system, which can be derived by setting $dx/dN = dy/dN = 0$. If there are no attractors, the trajectories with respect to $x(N)$ and $y(N)$ run from unstable fixed points to stable points. Two important stable points are given by

- (c) $(x, y) = (\lambda/\sqrt{6}, [1 - \lambda^2/6]^{1/2})$, $\Omega_\phi = 1$, $w_{eff} = -1 + \lambda^2/3$, $w_\phi = -1 + \lambda^2/3$.
- (d) $(x, y) = (\sqrt{3/2}(1 + w_M)/\lambda, [3(1 - w_M^2)/\lambda^2]^{1/2})$, $\Omega_\phi = 3(1 + w_M)/\lambda^2$, $w_{eff} = w_M$, $w_\phi = w_M$.

The point (c) corresponds to a scalar-field-dominated solution, which exists for $\lambda^2 < 6$. The cosmic acceleration is realized if $w_{eff} < -1/3$, *i.e.* $\lambda^2 < 2$. In the limit that $\lambda \to 0$ (*i.e.* $V(\phi) \to V_0$) we recover the equation of state of cosmological constant ($w_{eff} = w_\phi = -1$).

The point (d) is the so-called scaling solution in which the ratio $\Omega_\phi/\Omega_M$ is a non-zero constant. The existence of the scaling solution demands the condition $\lambda^2 > 3(1 + w_M)$ from the requirement $\Omega_\phi < 1$. Since $w_\phi = w_M$ for scaling solutions, it is not possible to realize cosmic acceleration unless the matter fluid has an unusual equation of state ($w_M < -1/3$).

Let us consider a realistic case in which the equation of state of the fluid is in the region $0 \leq w_M < 1$. Then the stability of the fixed points is summarized as follows.

- Point (c): Stable for $\lambda^2 < 3(1 + w_M)$.
- Point (d): Stable for $\lambda^2 > 3(1 + w_M)$.

If $\lambda$ is not constant, the fixed points derived in the constant $\lambda$ case can be regarded as "instantaneous" fixed points changing in time, provided that the time scale for the variation of $\lambda$ is much smaller than $H^{-1}$. For the RP potential, $V(\phi) = M^{4+\alpha}\phi^{-\alpha}$ ($\alpha > 0$, $\phi > 0$), we have that $\Gamma = (\alpha + 1)/\alpha > 1$ and $x > 0$ (because $\dot{\phi} > 0$), in which case the quantity $\lambda$ ($> 0$ from equation (1.51) because $\partial V/\partial\phi < 0$) decreases with time from equation (1.52). This means that the so-called tracking condition $\Gamma > 1$ is always satisfied in this case and that the solutions finally approach the accelerated "instantaneous" point (c) even if $\lambda^2 > 2$ during radiation and matter eras.
The tracking condition can be derived in the following way. We first define the quantity

$$\xi \equiv \frac{1 + w_\phi}{1 - w_\phi} = \frac{\dot{\phi}}{2V} \ . \tag{1.54}$$

Taking the derivative of $\xi$ in terms of $N$ and using the definition (1.44), we find

$$\lambda = \sqrt{\frac{3(1 + w_\phi)}{\Omega_\phi}} \left(1 + \frac{1}{6}\frac{d\ln\xi}{dN}\right) \ , \tag{1.55}$$

where we take the plus sign of the square root because $\lambda > 0$ for the RP potential. Differentiating equation (1.55) with respect to $\phi$, we get the following relation:

$$\Gamma = 1 + \frac{3(1 - \Omega_\phi)(w_M - w_\phi)}{(1 + w_\phi)(6 + \gamma')} - \gamma' a(w_\phi, \gamma', \xi) - 2\gamma'' b(w_\phi, \gamma') \ , \tag{1.56}$$

where $\gamma' \equiv d\ln\xi/dN$. Let us consider the evolution during the radiation- and matter-dominated epochs where $\Omega_\phi$ can be negligible compared to unity. If $\Gamma$ varies slowly in time,

equation (1.56) implies that there is a solution in which $w_\phi$ is nearly constant and its derivatives ($\gamma'$ and $\gamma''$) are negligible. Hence the equation of state of quintessence is nearly constant:

$$w_\phi \simeq \frac{w_M - 2(\Gamma - 1)}{1 + 2(\Gamma - 1)} \ . \tag{1.57}$$

Since $\Gamma > 1$, we have $w_\phi < w_M$ so that the quintessence energy density evolves more slowly than the background energy density. Hence the tracking solution can be realized under the condition $\Gamma > 1$ for $\Gamma$ nearly constant ($|d(\Gamma - 1)/dN| \ll |\Gamma - 1|$).

The epoch of the late-time cosmic acceleration is quantified by the condition

$$\lambda^2 = \frac{1}{\kappa V^2} \left( \frac{\partial V}{\partial \phi} \right)^2 < 2 \ , \tag{1.58}$$

*i.e.*

$$\phi > \frac{\alpha}{4\sqrt{\pi}} m_{pl} \ , \tag{1.59}$$

which is independent of the mass scale $M$. From the Friedmann equation (1.41) we can estimate the present potential energy of quintessence to be $V(\phi_0) \approx H_0^2 m_{pl}^2$, where $\phi_0 \approx m_{pl}$. Then the mass $M$ is constrained to be

$$M \approx \left( \frac{H_0}{m_{pl}} \right)^{\frac{2}{4+\alpha}} m_{pl} \approx 10^{-\frac{46-19\alpha}{4+\alpha}} \mathrm{GeV} \ , \tag{1.60}$$

where we have used $H_0 \approx 10^{-42}$GeV. For $\alpha = 2$ and $\alpha = 4$ we have that $M \approx 10^{-1}$GeV and $M \approx 10^4$GeV, respectively. These energy scales can be compatible with those appearing in particle physics.

Beside fixed points, phase spaces can be characterized also by special trajectories that "attract" other trajectories. Tracking solutions have approximately constant $w_\phi$ and $\Omega_\phi$ along these specials attractors. A wide range of initial conditions converge to a common, cosmic evolutionary tracker.
Here we take into account both radiation (energy density $\rho_r$) and non-relativistic matter (energy density $\rho_m$) together with the quintessence field. In this case the total energy density $\rho_M$ and pressure $p_M$ of the fluids in equations (1.41) and (1.45) are given by $\rho_M = \rho_r + \rho_m$ and $p_M = \rho_r/3$, respectively. In addition to the variables $x$ and $y$ defined in equation (1.42) we introduce another variable:

$$z \equiv \sqrt{\frac{\kappa \rho_r}{3}} \frac{1}{H} \ . \tag{1.61}$$

Then the density parameters for quintessence, radiation, and non relativistic matter are

$$\Omega_\phi = x^2 + y^2 \ , \quad \Omega_r = z^2 \ , \quad \Omega_m = 1 - x^2 - y^2 - z^2 \ . \tag{1.62}$$

Equation (1.45) can be written as

$$\dot{H} = -\frac{\kappa}{2}\left(\dot{\phi}^2 + \rho_M + \frac{1}{3}\rho_r\right) \ , \tag{1.63}$$

and we obtain

$$\frac{\dot{H}}{H^2} = -\frac{\kappa}{2H^2}\dot{\phi}^2 - \frac{\kappa}{2H^2}\rho_M - \frac{\kappa}{6H^2}\rho_r = -3x^2 - \frac{3}{2}(1 - x^2 - y^2) - \frac{1}{2}z^2 \ . \tag{1.64}$$

The effective equation of state reads

$$w_{eff} = \frac{\rho_{tot}}{p_{tot}} = 1 - \frac{2}{3}\frac{\dot{H}}{H^2} = x^2 - y^2 - \frac{z^2}{3} \ . \tag{1.65}$$

The equation of state of quintessence is the same as equation (1.48).
The equations for $x$, $y$, and $z$ are

$$\frac{dx}{dN} = \tilde{f}(x, y, z, \lambda) \ , \tag{1.66}$$

$$\frac{dy}{dN} = \tilde{g}(x, y, z, \lambda) \ , \tag{1.67}$$

$$\frac{dz}{dN} = h(x, y, z) \ . \tag{1.68}$$

From equation (1.57) the equation of state of quintessence in the tracking regime is given by

$$w_\phi \simeq \frac{\alpha w_M - 2}{\alpha + 2} \ . \tag{1.69}$$

If the tracking occurs during the matter-dominated epoch ($w_M = 0$), then

$$w_\phi \simeq -\frac{2}{\alpha + 2} \ . \tag{1.70}$$

From equation (1.55) the following relation holds

$$\frac{1}{6}\frac{d\ln\xi}{dN} = \Delta(t) - 1 \ , \quad \text{where} \ \ \Delta(t) \equiv \lambda\sqrt{\frac{\Omega_\phi}{3(1 + w_\phi)}} \ . \tag{1.71}$$

From the definition of $\xi$ in equation (1.54) we also obtain

$$\frac{1}{6}\frac{d\ln\xi}{dN} = \frac{1}{3(1 - w_\phi^2)}\frac{dw_\phi}{dN} \ . \tag{1.72}$$

Since $w_\phi$ is nearly constant for tracker solutions, it follows from equations (1.71) and (1.72) that $\Delta \simeq 1$. Hence the tracker solution is characterized by

$$\Omega_\phi \simeq \frac{3(1+w_\phi)}{\lambda^2} \ , \tag{1.73}$$

where $w_\phi$ is given in equation (1.69). For fixed $\lambda$, the scaling fixed point (d) corresponds to $\Omega_\phi = 3(1+w_M)/\lambda^2$ and $w_\phi = w_M$. In this case the tracker solution (1.73) recovers the scaling solution in the regime $\lambda^2 > 3(1+w_M)$ (under which the scaling solution is stable). The accelerated fixed point (c) for constant $\lambda$ corresponds to $\Omega_\phi = 1$ and $w_\phi = -1+\lambda^2/3$. The tracker solution (1.73) also covers this case and the accelerated solution is stable for $\lambda^2 < 3(1+w_M)$. Hence the tracker solution can be regarded as a stable attractor. For constant $\lambda$ the stable scaling solution (d) does not exit to the accelerated attractor (c), but for decreasing $\lambda$ the transition to the stable accelerated phase occurs through the tracking solution.

To sum up, the RP potential $V(\phi) = M^{4+\alpha}/\phi^\alpha$ is characterized by $\lambda \propto \alpha/\phi$, decreasing with time. Thus, following the tracker solution, as long as $\lambda^2 > 3(1+w_M)$, in the scaling regime the quintessence is tracked by the dominant cosmological component, then, when $\lambda^2 < 3(1+w_M)$, it starts to dominate and the accelerated phase takes place.

Compared to the RP case, the SUGRA exponential correction flattens the potential shape noticeably at $\phi \simeq m_{pl}$, *i.e.* at the end of the tracking trajectory. That brings the present-day SUGRA equation of state close to $-1$ even for steep potentials, *i.e.* with large values of $\alpha$. In other words, a given equation of state at present is obtained for noticeably higher values of $\alpha$ than for RP (Dolag et al., 2004).

## 1.3 Extended Quintessence

Extensions to GR in which the dark energy might have an interaction to gravity via an explicit coupling between quintessence and the Ricci scalar (Jordan frame, JF) have been considered. This is the case of scalar-tensor theories, known as extended quintessence (EQ) scenarios in the framework of dark energy. Here we consider the case in which $\phi$ interacts non-minimally with gravity (Wetterich, 1988; Boisseau et al., 2000) and we refer in particular to the extended quintessence models described in Perrotta et al. (2000), Pettorino et al. (2005) and Pettorino & Baccigalupi (2008).

In the Jordan frame, a scalar-tensor theory in which EQ holds is in general described by the following action:

$$S = \int d^4x\sqrt{-g}\left[\frac{1}{2\kappa}f(\phi,R) - \frac{\omega(\phi)}{2}\partial^\mu\phi\partial_\mu\phi - V(\phi) + \mathcal{L}_{\rm fluid}\right] \ , \tag{1.74}$$

where $R$ is the Ricci scalar, the function $f(\phi,R)$ specifies the coupling between the quintessence scalar field and the Ricci scalar, $\omega(\phi)$ and $V(\phi)$ specify the kinetic and potential terms respectively and the Lagrangian $\mathcal{L}_{\rm fluid}$ includes all the components but $\phi$ and can be expressed as $\mathcal{L}_{\rm fluid} = -m_0\bar{\psi}\psi + \mathcal{L}_{kin,\psi}$, where $m_0$ is a constant. Here we assume for the sake of simplicity a standard form for the kinetic part, $\omega(\phi) = 1$, and we define the coupling function as $f(\phi,R) = \kappa F(\phi)R$. In the case of EQ with a quadratic coupling, we work within the so-called "non-minimally coupled" theories, in which $F(\phi)$ is the sum of a dominant constant term plus a part depending on $\phi$:

$$F(\phi) = \frac{1}{\kappa} + \xi(\phi^2 - \phi_0^2) \ . \tag{1.75}$$

Another very popular choice is represented by *induced gravity* (IG), in which only the quadratic coupling is considered and no constant term is present.

Compared to GR, the Lagrangian has been generalized by introducing an explicit coupling between the Ricci scalar and the scalar field, achieved by replacing the usual Ricci scalar $R$ with the function $f(\phi, R)$. This new term, which has the effect of introducing a spacetime dependent gravitational constant, may either be interpreted as an explicit coupling between the quintessence field $\phi$ and gravity (or equivalently, in the Einstein frame, between dark energy and matter), or as a pure geometrical modification of GR admitting a nonlinear dependence on $R$.
The EQ with a non-minimal coupling we consider is described by the action

$$S = \int d^4x\sqrt{-g}\left[\frac{1}{2\kappa}R + \frac{1}{2}\xi(\phi^2 - \phi_0^2)R - \frac{1}{2}\partial^\mu\phi\partial_\mu\phi - V(\phi) + \mathcal{L}_{\rm fluid}\right] \ . \tag{1.76}$$

Here $\kappa \equiv 8\pi G_*$, where $G_*$ represents the "bare" gravitational constant, which is in general different from the Newtonian constant $G$ and is set in such a way that locally $1/\kappa + \xi(\phi^2 - \phi_0^2) = 1/8\pi G$ in order to match local constraints on GR. The parameter $\xi$ represents the "strength" of the coupling. In particular we consider a model with positive coupling $\xi > 0$ (EQp) and one with negative $\xi < 0$ (EQn). The limit of GR is recovered when $\omega_{\rm JBD} \gg 1$, where

$$\omega_{\rm JBD} \equiv \frac{F(\phi)}{[\partial F(\phi)/\partial\phi]^2} \ . \tag{1.77}$$

Stringent constraints for this quantity come from the Cassini mission (Bertotti et al., 2003) on Solar System scales, where $\omega_{\rm JBD0} > 4 \times 10^4$. However, it has been noted that such constraints may not apply at cosmological scales (Clifton et al., 2005) where complementary bounds, obtained combining WMAP1 and 2dF large scale structure data, provide the less tight limit of $\omega_{\rm JBD0} > 120$ at 95% confidence level (Acquaviva et al., 2005).
In EQ models, from the conserved scalar field stress-energy tensor

$$\begin{aligned} T_{\mu\nu\ [\phi]} &= \partial_\mu\phi\partial_\nu\phi - g_{\mu\nu}\left[\frac{1}{2}\partial^\rho\phi\partial_\rho\phi + V(\phi)\right] + \\ &+ \nabla_\mu\nabla_\nu F(\phi) - g_{\mu\nu}\nabla^\rho\nabla_\rho F(\phi) + \\ &+ \left[\frac{1}{\kappa} - F(\phi)\right]G_{\mu\nu} \ , \end{aligned} \tag{1.78}$$

we can define a conserved density and pressure for the scalar field, given by:

$$\rho_\phi = \frac{1}{2}\dot\phi^2 + V(\phi) - 3H\dot F(\phi) + 3H^2\left[\frac{1}{\kappa} - F(\phi)\right] \ , \tag{1.79}$$

$$p_\phi = \frac{1}{2}\dot\phi^2 - V(\phi) + \ddot F(\phi) + 2H\dot F(\phi) - (2\dot H + 3H^2)\left[\frac{1}{\kappa} - F(\phi)\right] \ , \tag{1.80}$$

respectively (see Appendix). Combining the continuity equation (1.9) with equations (1.79) and (1.80), the evolution of the scalar field is given by the Klein-Gordon equation

$$\ddot{\phi} + 3H\dot{\phi} + \frac{\partial V(\phi)}{\partial \phi} = \frac{1}{2}\frac{\partial F(\phi)}{\partial \phi} R \ , \tag{1.81}$$

where the Ricci scalar is given by[4]

$$R = 6(\dot{H} + 2H^2) \ . \tag{1.82}$$

Indeed

$$\begin{aligned} & \dot{\rho_\phi} + 3H(\rho_\phi + p_\phi) = \\ = \ & \dot{\phi}\ddot{\phi} + \frac{\partial V}{\partial \phi}\dot{\phi} - 3\dot{H}\dot{F} - 3H\ddot{F} + 6H\dot{H}\left(\frac{1}{\kappa} - F\right) - 3H^2\dot{F} + \\ + \ & 3H\left[\dot{\phi}^2 - H\dot{F} + \ddot{F} - 2\dot{H}\left(\frac{1}{\kappa} - F\right)\right] = \\ = \ & \dot{\phi}\ddot{\phi} + 3H\dot{\phi}^2 + \frac{\partial V}{\partial \phi}\dot{\phi} - 3\dot{F}(\dot{H} + 2H^2) = 0 \ , \end{aligned}$$

and dividing by $\dot{\phi}$

$$\ddot{\phi} + 3H + \frac{\partial V}{\partial \phi} = \frac{3\dot{F}}{\dot{\phi}}(\dot{H} + 2H^2) = 3\frac{\partial F}{\partial \phi}(\dot{H} + 2H^2) \ . \tag{1.83}$$

Equation (1.79) can be generally very different from equation (1.33), mostly because of the gravitational term $(\kappa^{-1} - F)$. Under conditions in which $F$ differs from $\kappa^{-1}$, even by a small amount due to a nonzero value of $\phi$, the gravitational term switches on, feeding the scalar field energy density itself with a term proportional to $H^2$, which in turn is proportional to the *total* cosmological energy density. At sufficiently early times the gravitational term dominates the dynamics of $\rho_\phi$ and forces the scalar field to behave as the dominant cosmological component (Perrotta et al., 2000). This process, named "gravitational dragging", is also very important for the dynamics of the dark energy perturbations.
In EQ scenarios, equation (1.10) can be expressed as

$$H^2 = \frac{\kappa}{3}\left[\rho_{0m}\left(\frac{a_0}{a}\right)^3 + \rho_{0r}\left(\frac{a_0}{a}\right)^4 + \rho_\phi\right] \ , \tag{1.84}$$

where $\rho_\phi$ is the conserved energy density defined in equation (1.79).

Looking at equations (1.75), (1.79), (1.80) we notice that minimally coupled quintessence is recovered for $\xi \to 0$.

[4]See equation (A.52).

For an extensive linear treatment of EQ models we refer to Pettorino & Baccigalupi (2008). Here we only recall that EQ models behave like minimally coupled quintessence theories in which, however, a time dependent effective gravitational interaction is present. In particular, in the Newtonian limit, the Euler equation for CDM can be written as

$$\nabla \dot{v}_m + H \nabla v_m + \frac{4\pi \tilde{G} M_m \delta(0)}{a^2} = 0 \ , \tag{1.85}$$

in terms of the cosmic time, where we have redefined the gravitational parameter as

$$\tilde{G} = \frac{2[F + 2(\partial F/\partial\phi)^2]}{[2F + 3(\partial F/\partial\phi)^2]} \frac{1}{8\pi F} \ . \tag{1.86}$$

The latter formalism is general for any choice of $F(\phi)$. For the coupling given by equation (1.75) we have

$$\tilde{G} = \frac{\left[\frac{1}{8\pi G_*} + (1+8\xi)\xi\phi^2 - \xi\phi_0^2\right]}{\left[\frac{1}{8\pi G_*} + (1+6\xi)\xi\phi^2 - \xi\phi_0^2\right]} \frac{1}{\left[\frac{1}{G_*} + 8\pi\xi(\phi^2 - \phi_0^2)\right]} \ . \tag{1.87}$$

For small values of the coupling, that is to say $\xi \ll 1$, the latter expression becomes

$$\frac{\tilde{G}}{G_*} \sim 1 - 8\pi G_* \xi(\phi^2 - \phi_0^2) \ , \tag{1.88}$$

which manifestly depends on the sign of the coupling $\xi$.

If for the potential term $V(\phi)$ we consider a RP potential $V(\phi) = M^{4+\alpha}\phi^{-\alpha}$ ($\alpha > 0$, $\phi > 0$), then $\dot{\phi} > 0$ and so $\phi^2 < \phi_0^2$. Thus $\tilde{G} > G_*$ for a positive coupling $\xi$, while $\tilde{G} < G_*$ for a negative $\xi$. We note that, since the derivative of the RP potential in equation (1.39) with respect to $\phi$ is $\partial V(\phi)/\partial\phi < 0$, we have $\phi^2 < \phi_0^2$. This leads to the behaviour of $\tilde{G}/G_*$ discussed in Section 1.5.

## 1.4 Coupled Quintessence

Within the usual frame of GR (Einstein frame, EF), the effect of a coupling between dark energy and dark matter [coupled quintessence (CQ)] has been investigated. Hydro-simulations including a coupling to dark matter have been presented in Baldi et al. (2010), Baldi (2011) and Baldi & Pettorino (2011). $N$-body simulations for coupled dark energy have been investigated in Macciò et al. (2004) and Zhao et al. (2010). The action considered in this case appears as follows:

$$S = \int d^4x\sqrt{-g}\left[\frac{1}{2\kappa}R - \frac{\omega(\phi)}{2}\partial^\mu\phi\partial_\mu\phi - V(\phi) - m(\phi)\bar{\psi}\psi + \mathcal{L}_{kin,\psi}\right] \ . \tag{1.89}$$

The choice of $m(\phi)$ specifies the coupling to $\psi$ matter fields while $\mathcal{L}_{kin,\psi}$ includes kinetic contributions from all components different from $\phi$.

The equations used to describe the background evolution of each component $i$ involved in the interaction follow from the consideration that the coupling can be treated as an external source acting on each stress-energy tensor $T^{\mu}{}_{\nu\ [i]}$ in such a way that the total stress-energy tensor is conserved:

$$\nabla_{\mu} T^{\mu}{}_{\nu\ [CDM]} = -CT\partial_{\nu}\phi \ , \tag{1.90}$$

$$\nabla_{\mu} T^{\mu}{}_{\nu\ [\phi]} = CT\partial_{\nu}\phi \ , \tag{1.91}$$

where $C$ is a constant and $T$ is the trace of $T^{\mu}{}_{\nu\ [CDM]}$. Baryons do not couple with dark matter or dark energy. The constant coupling term used here can be achieved in the case in which the mass of cold dark matter field depends exponentially on $\phi$:

$$m(\phi) = m_0 e^{-C\phi} \ , \tag{1.92}$$

corresponding, in the JF, to IG cosmologies.
IG theories in the JF (or equivalently CQ models in the EF with an exponential coupling in the Lagrangian) force the coupling constant to be positive in order to get the right sign for attractive gravity in action (1.74).

In the Newtonian limit, along the attractor, the full correction to the gravitational constant assumes the following expression:

$$\tilde{G} = G_* a^{-2C^2} = G(1 + 2C^2) a^{-2C^2} \ . \tag{1.93}$$

This clearly shows how the correction behaves regardless of the sign of the coupling constant (see Section 1.5).

## 1.5 Comparison

CQ and EQ models are strictly related through a conformal transformation called Weyl scaling. Altering GR via a scalar-tensor theory (Jordan frame, JF) is mathematically equivalent to coupling a scalar field universally with all matter fields within GR (Einstein frame, EF). Weyl scaling consists in a conformal transformation of the metric which, joined to a redefinition of matter fields, allows one to rewrite the action (1.89) into (1.74) or vice versa:

$$g_{\mu\nu} = A^2(\phi)\tilde{g}_{\mu\nu} \ , \tag{1.94}$$

$$\sqrt{-g} = A^4(\phi)\sqrt{-\tilde{g}} \ , \tag{1.95}$$

$$R = A^{-2}(\phi)[\tilde{R} - 6\tilde{g}^{\mu\nu}\nabla_{\nu}(\ln A)\nabla_{\mu}(\ln A)] \ , \tag{1.96}$$

$$\psi = A^{-3/2}(\phi)\tilde{\psi} \ , \tag{1.97}$$

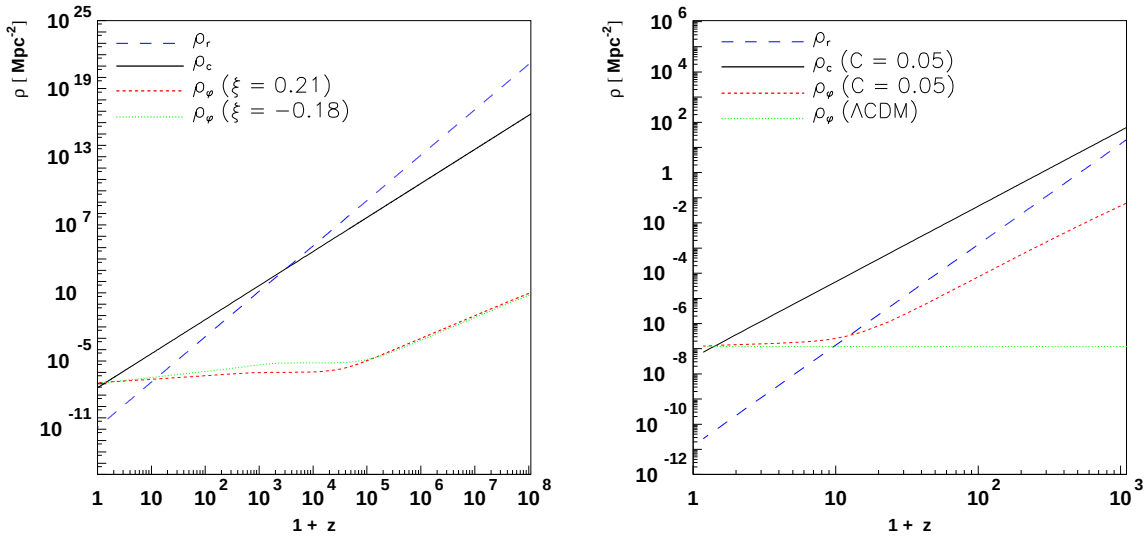


Figure 1.2: (Left panel) Evolution with redshift of radiation (blue), matter (black) and dark energy densities in EQ both for a positive (red) and negative (green) coupling corresponding to $\omega_{\rm JBD0} \sim 30$. (Right panel) Evolution with redshift of radiation (blue), matter (black) and dark energy densities in CQ with $C = 0.05$ (red) and $C = 0$ (green). From Pettorino & Baccigalupi (2008).

where we have used the tilde accent to identify quantities in the EF and distinguish them from those in the JF. Note also that the scaling factor $A(\phi)$ is related to the coupling $F(\phi)$ via the following relation:

$$A^2(\phi) = \frac{1}{\kappa F(\phi)} \ . \tag{1.98}$$

Going from one frame to the other must lead to the same identical observable effects, even if the description of the same model can be nasty in one frame and much simpler in the other. With this in mind, we can now compare some features of EQ and CQ models in comparison with ΛCDM, as discussed in Pettorino & Baccigalupi (2008).

At the background level, we show in Fig. 1.2 the energy densities of radiation, matter and dark energy as a function of redshift both for EQ (left panel) and CQ (right panel). For EQ, the energy density of the scalar field during the radiation-dominated era has a similar behaviour independently of the sign of $\xi$, while the two patterns detach a bit during the matter-dominated era. The effect of the coupling on the background evolution is an enhancement of the amount of the quantity of dark energy in the past, due to the gravitational dragging. For CQ, due to the coupling to cold dark matter, the dark energy density is attracted by the dark matter component. This effect is referred to as "dark matter dragging" in analogy to the gravitational dragging discussed in EQ.

Although the phenomenology and the energy density scaling are analogous for the EQ and CQ models shown in Fig. 1.2, it is important to stress that the sign of the coupling leads to different corrections to the Hubble expansion parameter, as we show in Fig. 1.3. We can see that, for the chosen CQ model, the Hubble parameter is bigger in the past than in the ΛCDM case, independently of the sign of the coupling. For the chosen EQ case, instead, depending on the sign of the coupling, the Hubble parameter can be either enhanced or reduced compared to the ΛCDM case. Moreover, the switch in sign does not lead to perfectly

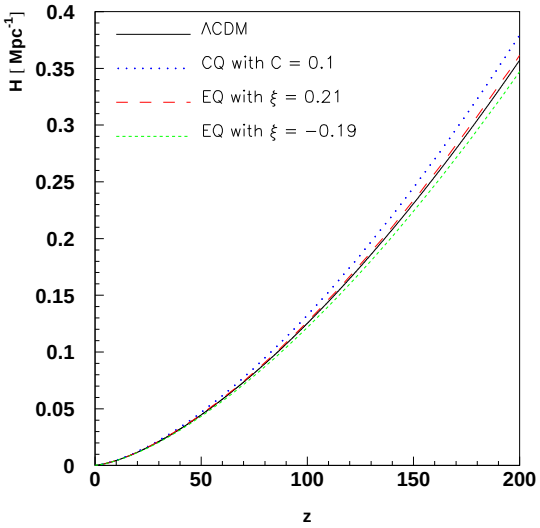


Figure 1.3: Evolution with redshift of the Hubble parameter in EQ (both for positive (red) and negative (green) couplings corresponding to $\omega_{\rm JBD0} \sim 30$) and CQ with $C = 0.1$ (blue). The ΛCDM case (black) is also shown as a reference. From Pettorino & Baccigalupi (2008).

opposite contributions: when the coupling is negative, the effect is bigger than in the case of a positive coupling with the same absolute value. An explanation for this fact can be that the extra term of the Klein-Gordon equation (1.81) adds to the usual potential for a negative coupling, thus favoring an enhancement in the dynamics of the field; on the contrary, for a positive coupling, the extra term contrasts the effect of the potential, making it more difficult to enhance the dynamics of the field.

At the linear perturbation level (see Section 2.1.1), the different couplings do affect the cosmological growth factor. In Fig. 1.4 we show the ratio between the density perturbation of cold dark matter and the scale factor, normalized to unity today. In the ΛCDM case, this quantity is almost constant during the matter-dominated era ($\delta(a) \propto a$) and then increases going back in time due to the presence of radiation. In the EQ case, $\delta(a)/a$ is higher than in the ΛCDM case, meaning that, for a fixed primordial normalization of the perturbations, the structure formation may be slower than in ΛCDM, depending on the sign and amplitude of the coupling $\xi$. Consistently with what we have shown before, the effect is stronger in the negative coupling case than in the positive coupling one. In the CQ case, the coupling to cold dark matter leads to a lower value of $\delta(a)/a$ than in the ΛCDM case, meaning that the the structure formation is enhanced compared to ΛCDM, independently of the sign of the coupling constant.
This behaviour can have important consequences in the nonlinear regime, that in fact can be used to constrain these theories, as we will see next.

Indeed, a coupling between dark energy and gravity or dark energy and cold dark matter could have observable effects on structure formation. In the Newtonian limit, as shown in equations (1.88) and (1.93), these couplings produce corrections to the gravitational constant. We show the behaviour of the correction in the EQ and CQ cases in Fig. 1.5. In the EQ case, the sign of the coupling has the effect of either increasing (positive coupling) or decreasing (negative coupling) the gravitational strength, as it is clear from equation (1.88). In the CQ case, the correction is independent of the sign of the coupling constant, and the gravitational

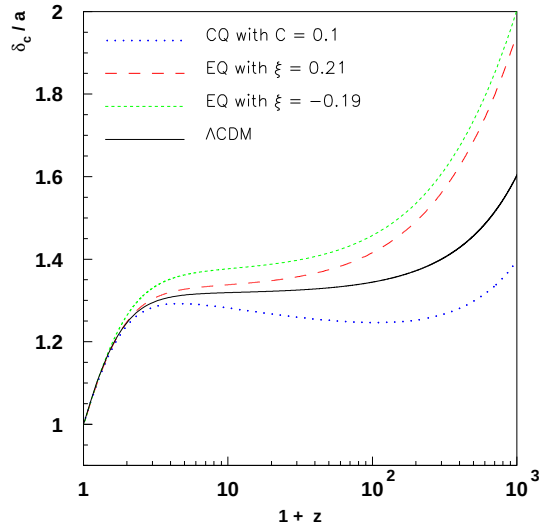


Figure 1.4: Evolution with redshift of the growth factor in EQ (both for positive (red) and negative (green) couplings corresponding to $\omega_{\rm JBD0} \sim 30$) and CQ with $C = 0.1$ (blue). The ΛCDM case (black) is also shown as a reference. From Pettorino & Baccigalupi (2008).

coupling is larger than the corresponding ΛCDM case, as it is evident from equation (1.93).

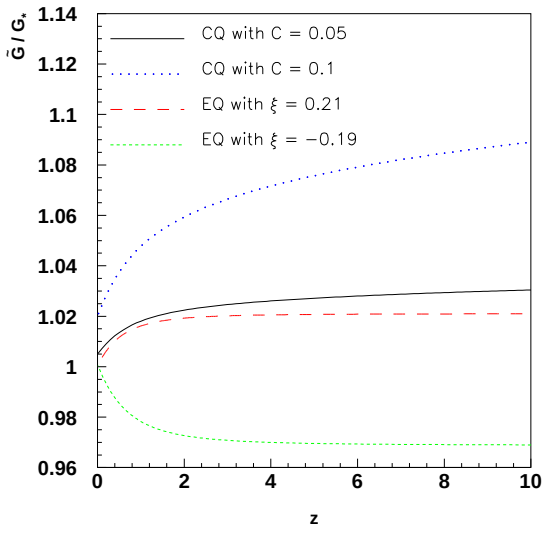


Figure 1.5: Evolution with redshift of the correction to the gravity constant in EQ (both for positive (red) and negative (green) couplings corresponding to $\omega_{\rm JBD0} \sim 30$) and CQ with $C = 0.1$ (blue) and $C = 0.05$ (black). From Pettorino & Baccigalupi (2008).

As the nonlinear regime is the interface to numerical simulations of structure formation in these scenarios, it is of fundamental importance to have convenient prescriptions to implement the features of these models into numerical codes. Pettorino & Baccigalupi (2008) present a list of all the needed input quantities for $N$-body simulations of EQ and CQ models. Since in this work we do not consider CQ models, here we will only recall the modifications needed

to run cosmological simulations of EQ models. In addition to the different expansion history represented by the Hubble parameter, that also enters in RP and SUGRA models, only the correction $\tilde{G}/G_*$ to the gravitational interaction between dark matter particles needs to be applied. In the case in which baryons are also considered, the same correction must be applied both to the interactions between baryon particles and between dark matter and baryon particles.

# Chapter 2

# Galaxy Clusters

Clusters of galaxies sit on top of the pyramid of hierarchical structure formation in the ΛCDM cosmological paradigm. They are the largest virialized objects that detached from the Hubble flow and formed in relatively recent times compared to the history of the Universe. The seeds of these structures were the small inhomogeneities of the primordial Universe that allowed clumps of dark matter (halos) to form and collapse under the action of the gravitational force. The gravitational potential of these halos started to attract baryons from the outside, eventually allowing the formation of the first stars and galaxies. From then on, the evolution of halos proceeded through minor and major mergers until the formation of the large galaxy clusters we see today. In this chapter we will review the theory of structure formation along with the main properties of baryons in galaxy clusters, using a multi-wavelength approach. In Section 2.1 we will concentrate on structure formation from the dark matter point of view, while in Section 2.2 we will discuss the observational properties of baryons inside dark matter halos. Useful references on these topics can be found in Allen et al. (2011) and Voit (2005).

## 2.1 Structure Formation

In the early Universe, despite the hypothesis of homogeneity and isotropy being valid at sufficiently large scales, the matter distribution was not perfectly uniform, but was characterized by some density fluctuations. If we indicate the mean matter density of the Universe with $\langle\rho_m\rangle$, then the density fluctuation field is expressed, as a function of position $\vec{x}$, by

$$\delta(\vec{x}) \equiv \frac{\rho_m(\vec{x}) - \langle\rho_m\rangle}{\langle\rho_m\rangle} \ , \tag{2.1}$$

which can be represented in the Fourier space as

$$\tilde{\delta}(\vec{k}) = \frac{1}{(2\pi)^{3/2}} \int \delta(\vec{x}) e^{i\vec{k}\cdot\vec{x}} d^3x \ . \tag{2.2}$$

The primordial power spectrum can be described as

$$P(k) = \langle|\tilde{\delta}(\vec{k})|^2\rangle \sim k^{n_s} \ , \tag{2.3}$$

with spectral index $n_s$ expected to be close to unity.

In general, $\delta(\vec{x})$ is considered to be a Gaussian random field, but other choices are also possible depending on the inflationary model. If $\delta(\vec{x})$ is also isotropic, then $P(k)$ is a complete statistical description of the initial perturbation spectrum. If we start from the power law expression (2.3) of the power spectrum and we consider the variance in mass $\sigma_M^2$ inside a given volume element, filtered with a spherical window function $W_R$, we find

$$\delta_M(\vec{x}) = \int \delta(\vec{y}) W_R(|\vec{x} - \vec{y}|) d^3y \ , \tag{2.4}$$

or, in Fourier space,

$$\sigma_M^2 = \frac{1}{(2\pi)^3} \int P(k) \tilde{W}_R^2(k) d^3k \ , \tag{2.5}$$

where $\tilde{W}_R(k)$ is the Fourier transform of the window function. For a top-hat spatial filtering

$$\tilde{W}_R(k) = 3 \left[ \frac{\sin(kR)}{(kR)^3} - \frac{\cos(kR)}{(kR)^2} \right] \ . \tag{2.6}$$

The shape of the power spectrum is fixed once the matter density parameter $\Omega_m$, the baryon density parameter $\Omega_b$ and the Hubble parameter $H_0$ are known, but its normalization must be fixed through observations of either the CMB radiation or the large-scale structure distribution. For historical reasons, this normalization is generally evaluated with respect to a top-hat window function having a comoving radius of 8 Mpc $h^{-1}$, and it is thus indicated with $\sigma_8$. The motivation for this choice is that the variance in galaxy number counts was found to be order of unity on this length scale. Moreover, the mass contained in the volume of the top-hat filter turns out to be $M \simeq 6 \times 10^{14}\ \Omega_m\ \mathrm{M}_\odot\ h^{-1}$, which is typical of a galaxy cluster. Therefore galaxy clusters can be used to constrain the normalization of the power-spectrum.

### 2.1.1 Growth of linear density perturbations

Once the seeds of the primordial density fluctuations are sown, they start to evolve under the action of the gravitational attraction driven by the overdense region itself. For small perturbations, in a universe with negligible density of radiation, the evolution of density perturbations $\delta \equiv \delta\rho/\rho$ is given by

$$\ddot{\delta} + 2\frac{\dot{a}}{a}\dot{\delta} = 4\pi G \langle \rho_m \rangle \delta \ . \tag{2.7}$$

This equation describes the growth of Jeans instabilities in a pressureless fluid, mitigated in some way by the term $2(\dot{a}/a)\dot{\delta}$ which describes the effect of the Hubble expansion of the Universe. The general solution of equation (2.7) can be expressed by

$$\delta(a) = \delta_+ D_+(a) + \delta_- D_-(a) \ , \tag{2.8}$$

where $D_+$ and $D_-$ describe the growing and decaying modes of the density perturbation, respectively. Conventionally, the linear growth factor is normalized such that $D_+(a) = 1$ at $z = 0$. The rate of perturbation growth does not depend on the scale of the perturbation. In

a flat matter-dominated universe, the perturbations evolve proportionally to the scale factor, $D_+(a) \propto a$. In a ΛCDM universe, the perturbation growth is frozen after the redshift at which the cosmic expansion rate becomes faster than the gravitational instability one, *i.e.* $1 + z = \Omega_m^{-1/3}$ (Borgani, 2006). The exact expression for the growth of perturbations is given by

$$D_+(z) = \frac{5}{2}\Omega_m E_z \int_z^\infty \frac{1+z'}{E_{z'}^3} dz' \ , \tag{2.9}$$

with $E_z = H_z/H_0$[1]. A simple parametrization of equation (2.7) is given by

$$\frac{d\ln\delta}{d\ln a} = {\Omega_m}^\gamma \ , \tag{2.10}$$

where $\gamma$ is the growth index. General Relativity predicts a scale-independent and nearly constant value of $\gamma \approx 0.55$.

### 2.1.2 Spherical Collapse

Cluster formation from perturbations of the cold dark matter density distribution is a hierarchical process. Small dark matter clumps are the first to detach from the Hubble flow and to undergo gravitational collapse. These small halos then merge to form progressively larger structures like cluster-sized objects.
The basics of cluster formation can be described by a spherically symmetric collapse model. In this model, the matter that forms a cluster starts as a low-amplitude density perturbation that at the beginning expands along with the rest of the universe. The perturbation's gravitational attraction gradually slows down the expansion of this matter and eventually stops and reverses the expansion. Then a clump of matter forms at the centre of the perturbation and, according to the initial radial density distribution of the perturbation, starts to accrete additional matter onto the halo.
A common toy model to describe the cluster formation process is the spherical top-hat model in which the perturbation leading to a cluster is assumed to be a spherical region of constant overdensity $\Delta = \rho/\rho_m$. In Newtonian mechanics, a shell of matter at distance $R$ from the centre of a spherical overdensity with uniform density $\rho$ moves according to

$$\frac{d^2R}{dt^2} = -\frac{GM(R)}{R^2} = -\frac{4}{3}\pi G\rho R \ . \tag{2.11}$$

Since, during the matter-dominated era, the background density scales as

$$\rho_m = \frac{3M(R_0)}{4\pi {R_0}^3 a^3} \ , \tag{2.12}$$

where $R_0$ is the initial size of the perturbation, we can define a density contrast

$$\delta = \left(\frac{aR_0}{R}\right)^3 - 1 \tag{2.13}$$

[1] See equation (A.79).

inside the shell and $\delta = 0$ outside. The crucial assumption is that $\delta$ is a top-hat function, which allows us to cancel out all spatial derivatives. Multiplying on both sides equation (2.11) by $2dR/dt$, the resulting equation can be integrated to obtain the cycloid equation

$$\left(\frac{dR}{dt}\right)^2 = \frac{2GM}{R} - C \ , \tag{2.14}$$

whose solution, for a positive integration constant $C$, can be parametrized through $\tau \in (0, 2\pi)$ as $R = GM(1 - \cos\tau)/C$ and $t = GM(\tau - \sin\tau)/C^{3/2}$. Substituting in equation (2.13) and choosing $C$ such that $\delta_{\tau=0} = 0$, we obtain, in the Einstein-de Sitter case ($\Omega_m = 1$ and $\Omega_{\rm DE} = 0$), for which $a = a_0(t/t_0)^{2/3}$,

$$\delta = \frac{9}{2}\frac{(\tau - \sin\tau)^2}{(1 - \cos\tau)^3} - 1 \tag{2.15}$$

and

$$\delta_L = \frac{3}{5}\left[\frac{3}{4}(\tau - \sin\tau)\right]^{2/3} \ , \tag{2.16}$$

where $\delta_L$ is the solution of the linearized equation. As expected, at first the radius $R$ increases (the perturbation expands with the cosmological background), then it reaches a turnaround value at $\tau = \pi$ and starts to decrease (the perturbation collapses under its own gravity). For $\tau = 2\pi$, in a time which is exactly twice the one required to reach the turnaround, the overdensity $\delta$ eventually collapses. This happens when

$$\delta_L = \delta_c = (3/5)(2\pi/2)^{2/3} \approx 1.686 \ . \tag{2.17}$$

The critical value $\delta_c$ of the linear fluctuation $\delta_L$ expressed by equation (2.17) is relevant in cosmological context because it is used in the Press-Schechter formalism to calculate the abundance of collapsed objects (see Subsection 2.1.3). In an Einstein-de Sitter universe, this value is independent of time. However, in other cosmological models, $\delta_c$ depends on time. An approximation for dark energy with a constant equation of state in a flat universe is given, *e.g.*, in Weinberg & Kamionkowski (2003).

For minimally coupled and extended quintessence models (see Chapter 1), $\delta_c$ grows slowly during the matter-dominated era, reaches a maximum, then decreases as soon as dark energy starts to dominate. In contrast with the minimally coupled case, in EQ models $\delta_c$ does not approach the Einstein-de Sitter value during the matter-dominated era, but it is higher for positive values of the coupling constant $\xi$ and lower for negative values of $\xi$. This is expected since, from equation (1.88), the effective gravitational constant which enters in equation (2.7) is $\tilde{G} > G_*$ for positive values of $\xi$ an vice versa. Thus, since

$$\delta_c = \lim_{a\to 0}\left[\frac{D_+(a_c)}{D_+(a)}\left(\Delta(a) - 1\right)\right] \ , \tag{2.18}$$

where $a_c$ is the scale factor at the time of collapse, the linear density contrast should be higher for models with higher values of the coupling constant.

Given that the matter overdensity of a top-hat perturbation can be approximated, in a flat universe with a nonzero cosmological constant, by (Bryan & Norman, 1998)

$$\Delta_{th} = 18\pi^2 + 82x - 39x^2 \ , \tag{2.19}$$

where

$$x = \left[\frac{\Omega_{0m}(1+z)^3}{E_z^2} - 1\right] \ , \tag{2.20}$$

the spherical top-hat model leads to a pragmatic definition of the virial radius of a halo as the radius $r_{th}$ within which the mean matter density is $\Delta_{th}\rho_c$,

$$R_{th} = \left(\frac{3M_{th}}{4\pi\Delta_{th}\rho_c}\right)^{1/3} \ . \tag{2.21}$$

However, since in a flat, matter-dominated universe, $\Delta_{th} = 18\pi^2 \approx 178$, other definitions are commonly used. In particular, $R_{200}$, within which the mean matter density is $200\rho_c$, and $R_{180m}$, within which the mean matter density is 180 times the mean background density $\Omega_m\rho_c$, are popular choices. As long as $\Omega_m \approx 1$, both $R_{200}$ and $R_{180m}$ are nearly identical to $R_{th}$, but since current data suggest now $\Omega_m \approx 0.3$, these radii are nowadays different, with $R_{200} < R_{th} < R_{180m}$. When generally speaking of virial radius, this multiplicity of definitions can indeed lead to some confusion.

### 2.1.3 Mass Function

A powerful tool to constrain cosmological parameters through the evolution of galaxy clusters is given by the cluster mass function, $n(M,z)$, which counts the number of halos of a given mass within a given volume. Expressed as a differential function of mass, it reads

$$\frac{dn(M,z)}{d\ln M} = \frac{\rho_m}{M}\left|\frac{d\ln\sigma}{d\ln M}\right| f(\sigma_M, z) \ , \tag{2.22}$$

where $\rho_m = \Omega_m\rho_c$ is the comoving[2] mean matter density and $f(\sigma)$ is a model-dependent function of the filtered perturbation spectrum (2.5). This function needs to be calibrated

[2]If we have, in physical coordinates,

$$\begin{aligned} \rho_m &= \rho_{0m}(1+z)^3 \ , \\ \rho_c &= \rho_{0c}E_z^2 \ , \\ \rho_{th} &= \Delta_{th}\rho_{0c}E_z^2 \ , \end{aligned}$$

then we have, in comoving coordinates,

$$\begin{aligned} \rho_m &= \rho_{0m} \ , \\ \rho_c &= \frac{\rho_{0c}E_z^2}{(1+z)^3} \ , \\ \rho_{th} &= \Delta_{th}\frac{\rho_{0c}E_z^2}{(1+z)^3} \ . \end{aligned}$$

against numerical simulations as done, *e.g.*, by Sheth & Tormen (1999) and Tinker et al. (2008). One way to obtain semianalytic prescriptions for this function is to combine the spherical top-hat collapse model with the growth function for linear perturbation theory, as done for example by Press & Schechter (1974). In a Press-Schechter-like formalism, where the density perturbations collapse and virialize if their density contrast does exceed a critical threshold $\delta_c$,

$$f(\sigma_M, z) = \sqrt{\frac{2}{\pi}} \frac{\delta_c}{\sigma_M(z)} \exp\left[-\frac{\delta_c^2}{2\sigma_M^2(z)}\right] \ . \tag{2.23}$$

Adopting this formalism with $\delta_c \simeq 1.69$ (see Subsection 2.1.2), independently of redshift, gives accepting results for the mass function at different redshifts, even if its derivation is rigorous only for spherical collapse. This expression has been generalized taking into account also non-spherical collapse in Sheth et al. (2001) and a formula from a fit of numerical results was proposed by Jenkins et al. (2001):

$$f(\sigma_M, z) = 0.315 \exp(-|\ln \sigma_M^{-1} + 0.61|^{3.8}) \ . \tag{2.24}$$

In minimally coupled and extended quintessence models, since the linear density contrast $\delta_c$ which appears in the exponent of equation (2.23) is different compared to the Einstein-de Sitter case (see Subsection 2.1.2), we expect visible changes in the mass function. In particular, higher values of the mass function are expected for lower values of the linear density contrast $\delta_c$ and vice versa.

The importance of the cluster mass function relies on the fact that by measuring it, one has a direct evaluation of $\sigma_M$ on scales of $10^{14}-10^{15}$ $M_\odot$ and is left only with a degeneracy between $\Omega_m$ and $\sigma_8$. Since the former can be measured through other methods, this degeneracy can be broken and the mass function can be used to evaluate $\sigma_8$.

### 2.1.4 Internal structure of dark matter halos

The ΛCDM paradigm predicts that dark matter halos are self-similar independently of their mass and that their profiles are different from the one describing a singular isothermal sphere. From numerical simulations, Navarro, Frenk & White (1996) (hereafter NFW) found that a two-parameter profile was a good description for the structure of dark matter halos. The NFW profile can be written as

$$\frac{\rho(r)}{\rho_c} = \frac{\delta_c}{(r/r_s)(1 + r/r_s)^2} \ , \tag{2.25}$$

where $\rho_c$ is the critical density, $r_s$ is the scale radius and $\delta_c$ is a characteristic density contrast. The two free parameter $r_s$ and $\delta_c$ are linked through the concentration of the halo with respect to a given overdensity $\Delta$,

$$c_\Delta \equiv \frac{R_\Delta}{r_s} \ , \tag{2.26}$$

by

$$\delta_c = \frac{\Delta}{3} \frac{c_\Delta^3}{[\ln(1+c_\Delta) - c_\Delta/(1+c_\Delta)]} \ . \tag{2.27}$$

It is possible to convert the halo concentration (2.26) defined at a given overdensity $\Delta_1$ with respect to the one defined at another overdensity $\Delta_2$ in an easy way, as shown by Hu & Kravtsov (2003), as long as the halo mass at the two overdensities is known:

$$c_{\Delta_2} = c_{\Delta_1} \left( \frac{M_{\Delta_2}}{M_{\Delta_1}} \frac{\Delta_1}{\Delta_2} \right)^{1/3} \ . \tag{2.28}$$

Besides the NFW profile and its three-parameter generalization

$$\frac{\rho(r)}{\rho_c} = \frac{\delta_c}{(r/r_s)^\alpha (1+r/r_s)^{3-\alpha}} \ , \tag{2.29}$$

other possibilities have been considered. In particular, Moore et al. (1999) proposed a slightly different two-parameter model

$$\frac{\rho(r)}{\rho_c} = \frac{\delta_c}{(r/r_s)^{1.5}[1+(r/r_s)^{1.5}]} \ , \tag{2.30}$$

while a completely different form is given by the Einasto profile

$$\ln\left[\rho(r)/\rho_{-2}\right] = (-2/\alpha)[(r/r_{-2})^\alpha - 1] \ , \tag{2.31}$$

where $r_{-2}$ marks the radius at which the logarithmic slope of the profile $\gamma(r) = -d\ln\rho/d\ln r$ equals the isothermal value, $\gamma = 2$, and $\rho_{-2}$ is the corresponding density, $\rho_{-2} \equiv \rho(r_{-2})$. Navarro et al. (2010) showed indeed that the latter profile is a better description of galaxy-sized halos than the original NFW one, arguing about the effective self-similiarity of dark matter halos. Moreover, it is known that cold dark matter halos have strongly triaxial shapes, with a slight preference for nearly prolate systems (Frenk et al., 1988; Jing & Suto, 2002; Allgood et al., 2006). This fact has important consequences both on the theoretical and on the observational side.

Because of the hierarchical nature of structure formation and the fact that collapsed objects retain information on the background average matter density at the time of their formation (Navarro, Frenk & White, 1996), concentration (2.26) and mass of a dark matter halo are related. Since low-mass objects form earlier than high-mass ones, and since in the past the background average matter density was higher, low-mass halos are expected to have a higher concentration compared to high-mass ones. These expectations have been confirmed by the results of $N$-body numerical simulations which find, at $z = 0$, a concentration-mass relation $c(M) \propto M^\alpha$, with $\alpha \sim -0.1$ (Gao et al., 2008; Zhao et al., 2010). For a given mass, the concentration evolution with redshift, if any, is still matter of debate (see *e.g.* Bullock et al., 2001; Eke et al., 2001; Neto et al., 2007; Duffy et al., 2008; Jing & Suto, 2002; Allgood et al., 2006; Prada et al., 2011).

## 2.2 Baryons in clusters

Beyond the simple picture outlined above, real galaxy clusters are indeed complex objects. What we call a galaxy cluster is a very different thing depending on the component we are considering, on the wavelength at which we are observing it and on the technique we are using to detect and analyze it. Regarding the dark matter component we have addressed so far, a galaxy cluster is a region which collapsed due to gravitational attraction, with density higher than the mean density of the Universe and mass of the order of $10^{14} - 10^{15}$ $M_{\odot}$. On the one hand, unfortunately, since cold dark matter does not emit electromagnetic radiation, this component, which counts for the large majority of a cluster mass, is not directly observable, even if it can be inferred from gravitational lensing measurements. On the other hand, the deep potential well of the dark matter halo does attract baryons from the outside permitting the formation of stars and galaxies, which are mainly visible in optical and infrared wavelengths. From this point of view, a galaxy cluster is a region in the sky where the abundance of galaxies is higher than the mean. Actually, this is the way in which galaxy clusters were originally identified and classified by Abell, and this is the reason why they are called in this way. Still, only a small per cent of the total baryon budget of a cluster is in the form of stars and galaxies. Most of the baryons reside in a diffuse gas component that goes under the name of intracluster medium (ICM). Due to the deepness of a cluster gravitational potential, this gas is in the form of a hot, almost completely ionized plasma which emits at X-ray wavelengths through bremsstrahlung. Galaxy clusters are characterized by having an extremely luminous, diffuse and extended X-ray emission. The presence of the ICM inside a cluster has an effect on the photons coming from the CMB and passing through it. This effect, known as Sunyaev-Zel'dovich (SZ) effect, results in a distortion of the blackbody spectrum of the CMB, produced through inverse Compton scattering by the high-energy electrons of the ICM. Thus, at mm-wavelengths, galaxy clusters can be detected and studied through the SZ effect. Finally, as predicted by General Relativity, the total mass distribution of a galaxy cluster bends the light coming from the sources beyond the cluster itself. This effect is known as gravitational lensing. In particular, if the projected mass density of the lens is high enough, as it happens in the central regions of galaxy clusters, the gravitational lensing produces multiple images, arcs and rings of the background sources (strong lensing). In the outer regions, where the projected mass density is lower, the gravitational lensing manifests itself as a statistical change in the orientation of the sources beyond the lens (weak lensing).
Thus, if we consider also the baryonic component, galaxy clusters are very complex systems, in which physics plays a crucial role at many different levels. But thanks to this, they contain a great amount of information that can be used in cosmological context. Moreover, the different cosmological constraints obtained from galaxy clusters are somehow orthogonal to the ones coming from other probes, allowing us to break some degeneracies in the parameters determination. As pointed out before, the most relevant physical quantity for a galaxy cluster is its mass, but unfortunately the total mass is not directly observable. So, it is mandatory to use other observable quantities as proxies for the mass and to have well calibrated scaling relations between those quantities and the mass itself.

### 2.2.1 Observational properties of galaxy clusters

Starting from the pioneering works by Zwicky (1933, 1937), Smith (1936) and Abell (1958), galaxy clusters were first identified through optical observations. Zwicky (1933) was the first to measure galaxy velocity dispersion inside the Coma cluster, concluding that the visible mass was not enough to explain the observed velocity dispersion and finding the first observational

evidence for the necessity of dark matter. Smith (1936) did find the same necessity in the Virgo cluster. They come to this conclusion by applying the virial theorem of classical mechanics, that holds for gravitationally bound systems. Abell was the first to systematically catalog galaxy clusters depending on the richness of galaxy in a given projected area. His catalog was built by taking all the galaxies in a given area with magnitude brighter than a given value, after subtracting the background level of galaxies taken from a cluster-free area of the sky. Basically, given the necessary improvement, this is still the approach used today for the optical identification of galaxy clusters.
A quantity which is usually linked to the optical galaxy richness is the cluster luminosity, generally studied through a luminosity distribution function. That function was first proposed by Schechter (1976) and takes the form

$$n(L)dL = N^*(L/L^*)^{-\alpha}\exp(-L/L^*)d(L/L^*)\ , \tag{2.32}$$

where $L^*$ is a characteristic luminosity ($L^* \approx 2 \times 10^{10}$ $L_\odot$) and $\alpha \simeq 5/4$.
Measuring galaxy velocity dispersion can help to disentangle projection effects and exclude non-cluster members. This can be done by supposing that the distribution of cluster galaxies is Gaussian and thus considering galaxies with velocities outside the best-fitting Gaussian as non-cluster members. Both the virial theorem and the velocity dispersion of galaxies can be used in principle to determine the mass of a galaxy cluster. But they rely on the assumptions that galaxy clusters are isolated, steady systems. In reality, clusters are quite young objects, often still undergoing their relaxation phase, and are not isolated from the rest of the Universe. Those facts have to be taken into account when applying those techniques to infer galaxy cluster mass.

Zwicky (1937) was also the first to recognize the importance of gravitational lensing to trace the dark matter component, even if the first results in this field came out almost thirty years later. Compared to other methods, gravitational lensing has the advantage that it does not rely on any assumption about the dynamical state of the cluster. Strong lensing measures the amount of mass contained in a cylinder limited by the Einstein radius of the system, which is about one tenth of the virial radius. For this reason it is a very powerful tool to evaluate the projected mass in the central region of clusters, but it is very sensitive to triaxiality if one wants to deproject the obtained results. Moreover, the existence itself of arcs in the strong lensing regime suggests that galaxy clusters should have steep central density profiles (Hammer & Rigaut, 1989). Weak lensing analysis relies instead on the statistical distortion of the shape and orientation of objects beyond the lens. This distortion, that can be split into convergence and shear, is proportional to the gradient of the underlying mass distribution. Thus weak lensing can be used to study the mass profile of the lens in the outer regions. Projected mass profiles obtained from weak lensing are generally well fitted by a singular isothermal sphere or by a NFW profile. An exhaustive review of gravitational lensing can be found in Bartelmann (2010).

As we already pointed out, galaxy clusters are characterized by a diffuse X-ray emission, with luminosities of the order of $10^{43} - 10^{45}$ erg s$^{-1}$, mainly due to bremsstrahlung radiation from the thermal hot plasma of the ICM. The ICM has typical temperatures of the order of $kT \sim 1 - 10$ keV and Hydrogen column densities of $N_H \lesssim 10^{22}$ cm$^{-2}$. The first property excludes that the emission can come from a non-thermal plasma with a power law electron energy distribution, such as the one responsible for radio emission, while the latter excludes that the origin of the emission resides in compact sources, confirming that the ICM is indeed diffuse. At temperatures of the order of $kT \sim 1 - 10$ keV ($T \sim 10^7 - 10^8$ K) and electron

density $n_e \sim 10^{-2} - 10^{-4}$ cm$^{-3}$ the ICM is completely ionized, with the exception of a small fraction of heavy elements, which are only partially ionized, like Fe which is responsible for a characteristic emission line at 7 keV. Since the mean free path of the electrons is far smaller than the typical dimension of a cluster, the plasma can be treated as a fluid.
The most important radiative process that happens in the ICM is bremsstrahlung radiation. If one integrates the emissivity $\epsilon(\nu)$ over all the frequencies $\nu$ and on the total volume $V$ of the cluster, the total luminosity in the X-ray band is given by

$$L_X = \int_V dV \int_{\Delta\nu} \epsilon(\nu) d\nu \ , \tag{2.33}$$

that at high temperatures can be approximated as

$$L_X \sim \langle n_e^2 \rangle T^{1/2} V \ . \tag{2.34}$$

That means that the X-ray luminosity of a cluster strongly depends on the gas density, while the dependence on the temperature is weaker. At densities typical of the ICM and scales typical of galaxy clusters, the plasma is optically thin and it is transparent to the X-ray radiation.
X-ray radiation is also the most efficient way of cooling galaxy clusters. The cooling time of the whole system is comparable to the Hubble time, thus cooling is not so relevant as a global feature, but plays a fundamental role in regulating the behaviour of galaxy cluster cores. In principle, in the inner regions of clusters, the densities are so high that the energy loss due to radiation is not negligible anymore. On the one hand, this is of crucial importance to permit the formation of stars and galaxies, that can emerge only from cold gas. On the other hand, if this cooling were not balanced by some form of heating, the system would not be able to support the external pressure of the gas, ending up with the collapse of the system itself. A fundamental role in balancing this cooling is played by the feedback from supernovae and active galactic nuclei (AGNs).
The gas cooling is also very useful for the morphological classification of clusters of galaxies in X-ray band. Clusters characterized by a well defined central peak in the luminosity also show a decrease of the temperature in the central regions ($r \lesssim 100$ kpc) and are referred to as cool-core clusters. They are somewhat representative of the population of relaxed objects, as opposed to non cool-core clusters which are in general unrelaxed.
The most usual way to describe the radial distribution of the ICM is an extension to the King model for the regular isothermal sphere (King, 1962) introduced in Cavaliere & Fusco-Femiano (1976) and known as $\beta$-model,

$$\rho_{gas}(r) \propto \left[1 + \left(\frac{r}{r_c}\right)^2\right]^{-3\beta/2} \ , \tag{2.35}$$

where $r_c$ is a core radius and

$$\beta = \frac{\mu m_p \sigma_r^2}{kT} \ , \tag{2.36}$$

where $\mu$ is the molecular weight, $m_p$ is the proton mass, $\sigma_r$ is the velocity dispersion and $T$ is the temperature of the plasma. This model is in general a good description of the observed

X-ray surface brightness profiles in the range $[1-3]r_c$ with $\beta_{fit} \approx 2/3$ and $r_c \sim 0.1 R_{vir}$ (Jones & Forman, 1984). Despite being a good approximation to observed data, the $\beta$-model is based on physical assumptions that are rather too simple and not always realized in nature. In particular, it is known that galaxy clusters are not isothermal but show a temperature profile $T(r)$, than in principle can influence the value of $\beta$. Basically, one can fit a polytropic model $T \propto \rho_{gas}^{\gamma-1}$, with polytropic index $\gamma$ running between 1 and 5/3, corresponding to the isothermal and adiabatic case, respectively.
Under the hypothesis of hydrostatic equilibrium, the total mass of a galaxy cluster can be determined once the radial profiles of the ICM density and temperature are known. Under this hypothesis, it is possible to recover the total gravitating mass as a function of radius through

$$M_{tot}(r) = -\frac{kT(r)r}{\mu m_p G}\left(\frac{d\ln\rho_{gas}}{d\ln r} + \frac{d\ln T}{d\ln r}\right) , \tag{2.37}$$

which shows a stronger dependence on gas temperature than on gas density.

### 2.2.2 Baryon fraction

The census of baryons inside galaxy clusters depends on both the radius within which we are considering the matter distribution and the total mass of the system. The gas-to-stellar mass ratio increases from nearly unity in cores of small groups ($\sim 10^{13}$ $M_\odot$) to a factor of five more at large radii of big clusters ($\sim 10^{15}$ $M_\odot$) (David et al., 1995; Gonzalez et al., 2007). Additionally, since the ICM is more diffuse than dark matter, the gas fraction $f_{gas} = M_{gas}/M_{tot}$ is increasing with radius in groups and clusters, reaching an almost constant value of about 0.13 at large radii of hot and massive clusters (David et al., 1995; White & Fabian, 1995; Allen et al., 2004; Vikhlinin et al., 2006; De Boni & Bertin, 2008). This value is somewhat smaller than the cosmological one of 0.17 by an amount that can be expressed through the depletion parameter $b_{gas} \equiv f_{gas}/(\Omega_{0b}/\Omega_{0m})$.

The gas fraction obtained from X-ray observations is an important quantity if one wants to use galaxy clusters as cosmological probes. There are two methods, orthogonal to the others involving different cosmological probes, which use galaxy clusters to constrain the amount of matter and the geometry of the Universe (see *e.g.* Allen et al., 2004; Ettori et al., 2009). On the one hand, together with independent determinations of $\Omega_b$ from CMB and primordial nucleosynthesis, $f_{gas}$ can be used to constrain the total amount of matter in the Universe through $\Omega_m = Y\Omega_b/f_{gas}$, where $Y$ is a factor, estimated from hydrodynamical simulations, accounting both for the depletion parameter and the fact that not all the baryons in a cluster are contained in the ICM. On the other hand, since $f_{gas} \propto {d_A}^{3/2}$, where $d_A(\Omega_m, \Omega_{\rm DE}, w_{\rm DE})$ is the angular distance of the cluster, its value can be used to constrain the geometry of the Universe, under the assumption that the gas fraction is constant with redshift. Allen et al. (2008) applied this method using *Chandra* measurements of 42 X-ray luminous, hot and relaxed galaxy clusters. In Fig. 2.1 we show a comparison between the apparent $f_{gas}$ value as a function of redshift in a flat $\Lambda$CDM cosmology ($\Omega_m = 0.3, \Omega_\Lambda = 0.7, h = 0.7$) and the one in a standard cold dark matter (SCDM) cosmology ($\Omega_m = 1, h = 0.5$). The gas mass fraction is evaluated at $R_{2500}$ which is the radius within which the matter density of the cluster is 2500 times the critical density. The results for $\Lambda$CDM are consistent with the hypothesis of no evolution of $f_{gas}$ with redshift, while the results for SCDM are clearly inconsistent with this prediction.

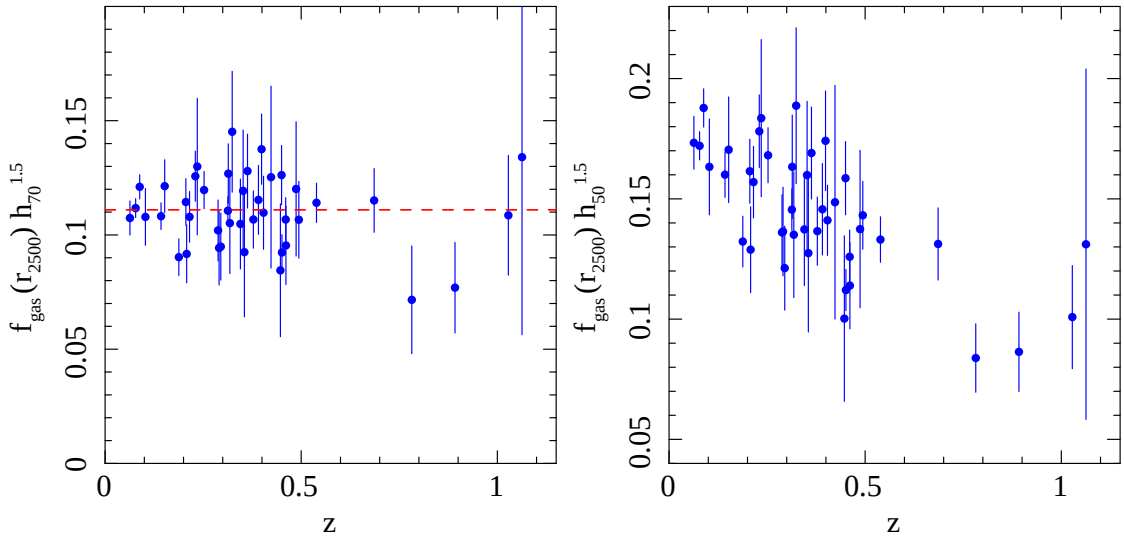


Figure 2.1: Apparent variation of the X-ray gas mass fraction within $R_{2500}$ as a function of redshift for (left panel) a ΛCDM cosmology ($\Omega_m = 0.3, \Omega_\Lambda = 0.7, h = 0.7$) and (right panel) a SCDM ($\Omega_m = 1, h = 0.5$) cosmology. From Allen et al. (2008).

### 2.2.3 Scaling relations

Since mass is not a directly observable quantity, one should rely on some proxies to infer the total mass of galaxy clusters, which is used to constrain cosmological parameters. Moreover, it is important to have robust, low-scatter scaling relations between these proxies and the mass. X-ray observables are in general good proxies because they are relatively easy to observe and are tightly correlated to total cluster mass.
Under the hypothesis of hydrostatic equilibrium,

$$\frac{d(\rho_{gas} T)}{dr} \approx \frac{\rho_{gas} G M_{tot}}{r^2} \ , \tag{2.38}$$

one has $M_{tot} \propto TR$ and, given the definition of the total mass at a given overdensity $\Delta_z$, $M_{tot} \propto E_z^2 \Delta_z R^3$,

$$E_z \Delta_z^{1/2} M_{tot} \propto T^{3/2} \ . \tag{2.39}$$

In the same way, one can relate the luminosity $L_X$ and the temperature $T$ of the plasma using the fact that, at high temperatures, its emissivity is linked to the temperature by

$$\epsilon \propto \Lambda(T) n_e^2 \propto T^{1/2} n_e^2 \ . \tag{2.40}$$

Then,

$$L_X \approx T^{1/2} n_e^2 R^3 \approx T^{1/2} f_{gas}^2 M_{tot}^2 R^{-3} \approx f_{gas}^2 T^2 \ , \tag{2.41}$$

using equation (2.39), as long as $f_{gas}$ is independent of temperature and total mass. Starting from these relations, one can derive a set of self-similar (not counting for additional heating

or cooling) scaling laws between the physical properties of galaxy clusters. In particular, combining all the cosmological dependence in the factor $F_z = E_z(\Delta_z/\Delta_{z=0})^{1/2}$, one gets the following scaling relations:

$$F_z M_{tot} \propto T^{3/2} \ , \tag{2.42}$$
$$F_z M_{gas} \propto T^{3/2} \ , \tag{2.43}$$
$$F_z^{-1} L_X \propto T^2 \ , \tag{2.44}$$
$$F_z^{-7/3} L_X \propto M_{tot}^{4/3} \ . \tag{2.45}$$

Kravtsov et al. (2006) introduced a new quantity as mass proxy, namely the X-ray equivalent of the SZ Compton parameter, $Y_X = M_{gas} \times T$. The corresponding scaling relation is given by

$$F_z^{2/5} M_{tot} \propto Y_X^{3/5} \ . \tag{2.46}$$

Using this proxy, which has a lower intrinsic scatter compared to the others, Vikhlinin et al. (2009a) built a mass function for galaxy clusters observed with *Chandra* in two redshift bins. The low-redshift sample contains 49 objects in the range $0.025 < z < 0.22$, while the high-redshift sample contains 36 objects in the range $0.35 < z < 0.9$, with mean redshift $\langle z \rangle \approx 0.55$. In Fig. 2.2 we show the measured mass functions at low and high redshifts compared with predictions for a flat ΛCDM model ($\Omega_m = 0.25, \Omega_\Lambda = 0.75, h = 0.72$) and an open cold dark matter model (OCDM) without dark energy ($\Omega_m = 0.25, \Omega_\Lambda = 0, h = 0.72$). In the ΛCDM case, the measured mass function is in good agreement with theoretical expectations in both redshift bins, while in the OCDM case the data are in tension with the predicted cluster number density in the high redshift bin.

An analysis of the X-ray luminosity scaling relations in a sample of 31 galaxy clusters from the Representative *XMM-Newton* Cluster Structure Survey (REXCESS) was presented in Pratt et al. (2009). In Fig. 2.3, Fig. 2.4, and Fig. 2.5 we show the results for the $L_X - T$, $L_X - Y_X$, and $L_X - M$ relations, respectively. The luminosity in the bolometric $[0.01 - 100]$ keV X-ray band is evaluated both for the entire cluster emission within $R_{500}$ and in the $[0.15 - 1]R_{500}$ aperture. $R_{500}$ is estimated iteratively from the $Y_X - M_{500}$ relation of Arnaud et al. (2007). For the REXCESS sample, the slopes of the $L_X - T$, $L_X - Y_X$, and $L_X - M$ best-fitting relations are all steeper than the self-similar expectations. The simple exclusion of the emission within $0.15\ R_{500}$ results in a reduction of the scatter in all the relations. The results strongly depend both on the fitting method and the dynamical state of the systems in the sample.

### 2.2.4 Observed $c - M$ relation

As we already said in Subsection 2.1.4, the concentration of a dark matter halo is linked to its mass through the $c - M$ relation. Numerical simulations generally agree with a power law relation with slope $\approx -0.1$, with a log-normal scatter ranging from 0.15 for relaxed systems to 0.30 for disturbed ones (Jing, 2000). This is true for idealized, dark matter only clusters, but in real objects the impact of baryon physics is strong, in particular in the inner regions. Indeed, even if the ICM is described by a cored $\beta$-model profile (2.35), in the central region it tends to cool and to form stars, which accumulate in the core of the cluster, thus increasing the total concentration. Moreover, it is supposed that this baryon contraction does also affect the

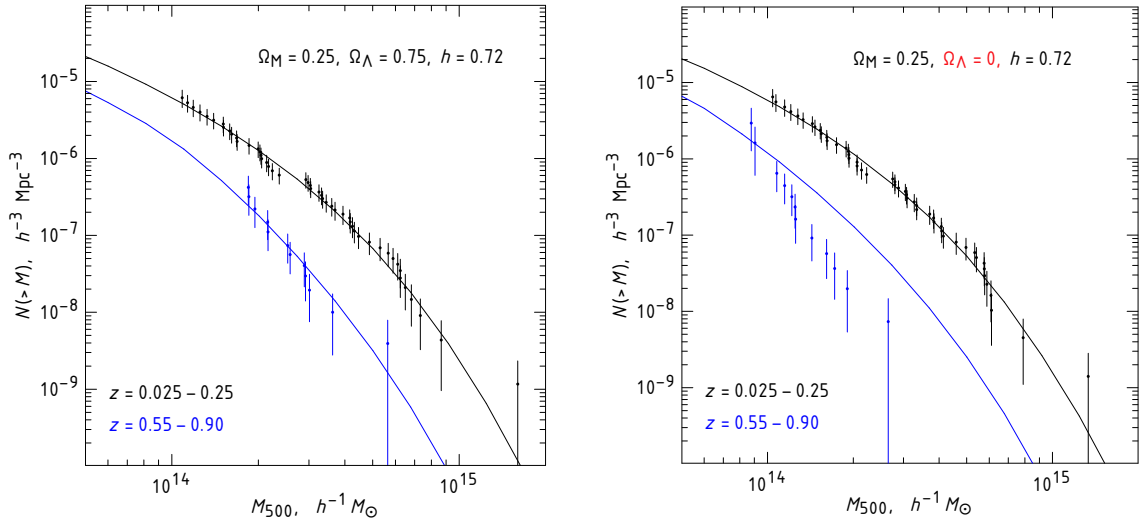


Figure 2.2: Measured mass functions and predicted models at low and high redshifts for (left panel) a ΛCDM cosmology ($\Omega_m = 0.25, \Omega_\Lambda = 0.75, h = 0.72$) and (right panel) an OCDM ($\Omega_m = 0.25, \Omega_\Lambda = 0, h = 0.72$) cosmology. In the right panel, both the data and the models at high redshift are changed relative to the ΛCDM case. From Vikhlinin et al. (2009a).

dark matter component, through an adiabatic contraction effect, leading thus to an increase of the dark matter concentration. The adiabatic contraction model has been described in Blumenthal et al. (1986) and Ryden & Gunn (1987), but, for an updated treatment, see also Fedeli (2011) and references therein. Numerical simulations to study the impact of baryon physics on the structure of dark matter halos were carried out in Duffy et al. (2010). The reason for that was to try to reconcile the discrepancy between the expectations from dark matter only simulations and the concentrations inferred from observations, as pointed out in Duffy et al. (2008). Actually, there is still poor agreement between the observed $c - M$ relation and the predicted one, with the first having, in general, a steeper slope and a higher normalization compared to the latter.

A census of the observed $c-M$ relation from different authors can be found in Fedeli (2011). In Fig. 2.6 we show, from that work, the comparison between the observed $c - M$ relations of Buote et al. (2007), Comerford & Natarajan (2007), Ettori et al. (2010), Oguri et al. (2012), Schmidt & Allen (2007), and Wojtak & Łokas (2010) with the predictions from Gao et al. (2008) at $z = 0$, namely a power law relation $c \propto M^{-\alpha}$ with $\alpha = 0.138$. Fedeli (2011) found that, in general, the observed $c - M$ relation is steeper than the one predicted from numerical simulations, independently of the way in which clusters are observed and selected. In the cases where the slope is consistent with theoretical predictions, *i.e.* Comerford & Natarajan (2007) and Wojtak & Łokas (2010), the normalization is too high to agree with a ΛCDM cosmology with $\sigma_8 \sim 0.8$.

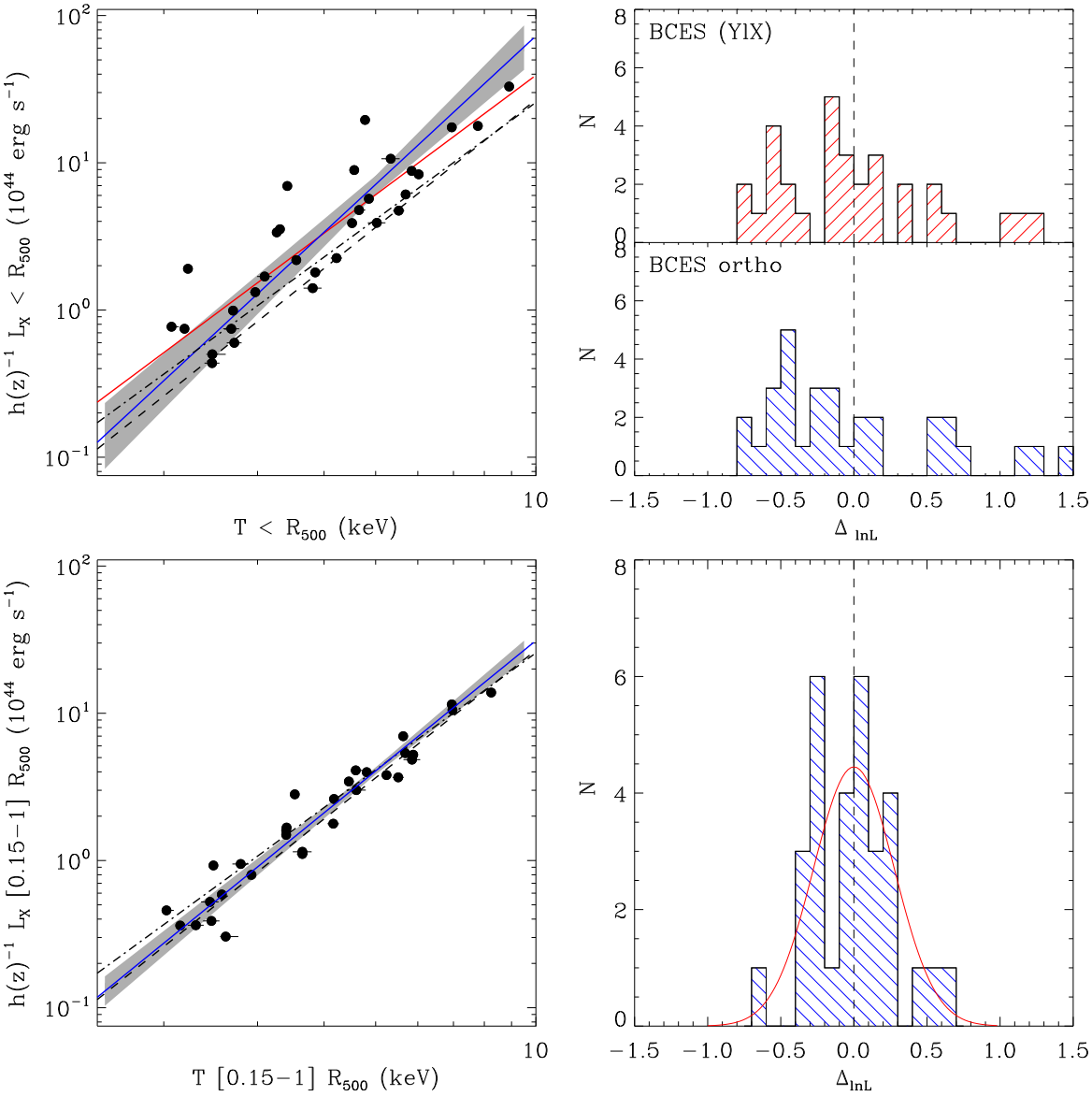


Figure 2.3: (Top-left panel) $L_X - T$ relation for the REXCESS sample (quantities derived from all emission within $R_{500}$). The best-fitting power law relations for two different methods are overplotted as solid red and blue lines. (Top-right panel) Histogram of the log space residuals about the best-fitting $L_X - T$ relation, derived for each fitting method. (Bottom-left panel) $L_X - T$ relation for the REXCESS sample (quantities derived from emission in the $[0.15 - 1]R_{500}$ aperture). The best-fitting power law relation is overplotted as a solid line. (Bottom-right panel) Histogram of the log space residuals about the best-fitting $L_X - T$ relation. For the details, see Pratt et al. (2009).

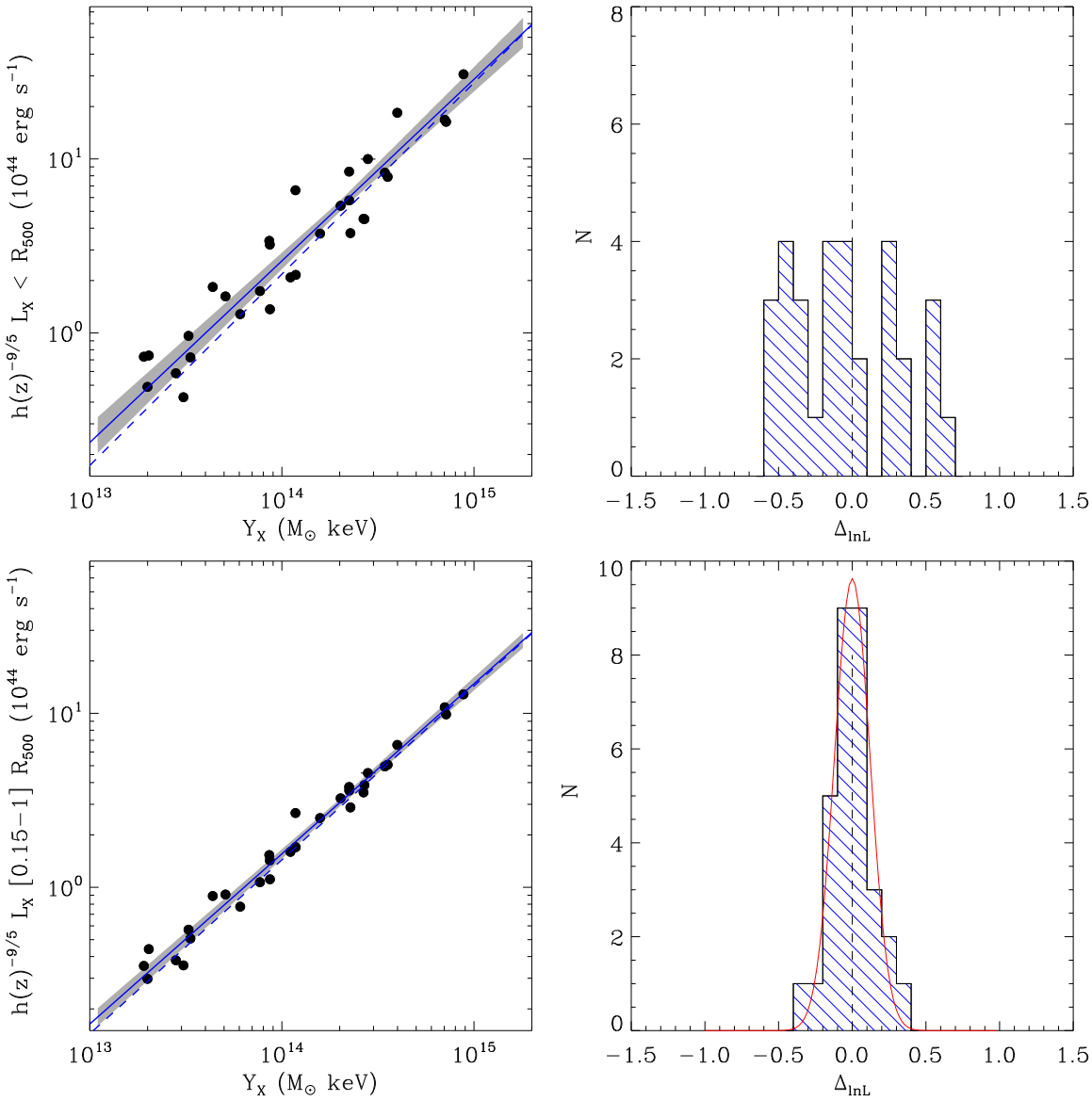


Figure 2.4: (Top-left panel) $L_X - Y_X$ relation for the REXCESS sample (luminosity derived from all emission within $R_{500}$). The best-fitting power law relation is overplotted as a solid line. (Top-right panel) Histogram of the log space residuals about the best-fitting $L_X - Y_X$ relation. (Bottom-left panel) $L_X - Y_X$ relation for the REXCESS sample (luminosity derived from emission in the $[0.15 - 1]R_{500}$ aperture). The best-fitting power law relation is overplotted as a solid line. (Bottom-right panel) Histogram of the log space residuals about the best-fitting $L_X - Y_X$ relation. For the details, see Pratt et al. (2009).

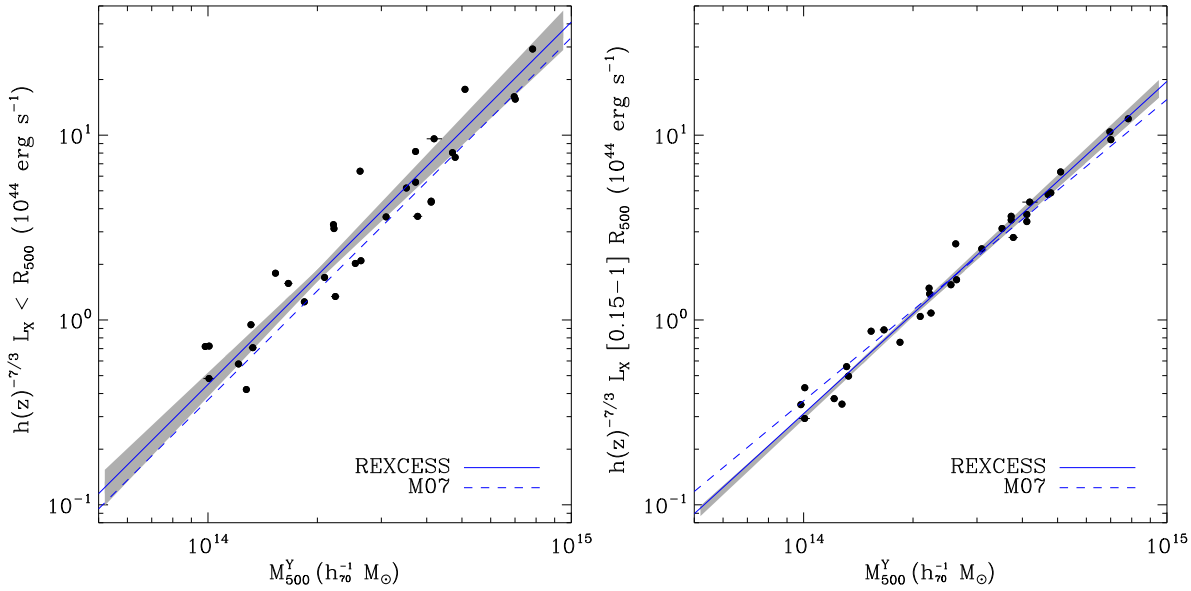


Figure 2.5: (Left panel) $L_X - M$ relation for the REXCESS sample, with the mass estimated from the $Y_X - M$ relation (luminosity derived from all emission within $R_{500}$). The best-fitting power law relation is overplotted as a solid line. (Right panel) $L_X - M$ relation for the REXCESS sample, with the mass estimated from the $Y_X - M$ relation (luminosity derived from emission in the $[0.15 - 1]R_{500}$ aperture). The best-fitting power law relation is overplotted as a solid line. For the details, see Pratt et al. (2009).

The first explanation for the discrepancy between the predicted and the observed $c - M$ relations can be searched in the fact that N-body simulations lack the contribution from baryonic physics. Numerical simulations including also hydrodynamics should give a more realistic representation of observed objects. In particular, the cooling of gas in the very central regions of halos and the consequent formation of galaxies should increase the concentration of the halos, in particular in low-mass objects, thus increasing the slope of the $c - M$ relation.

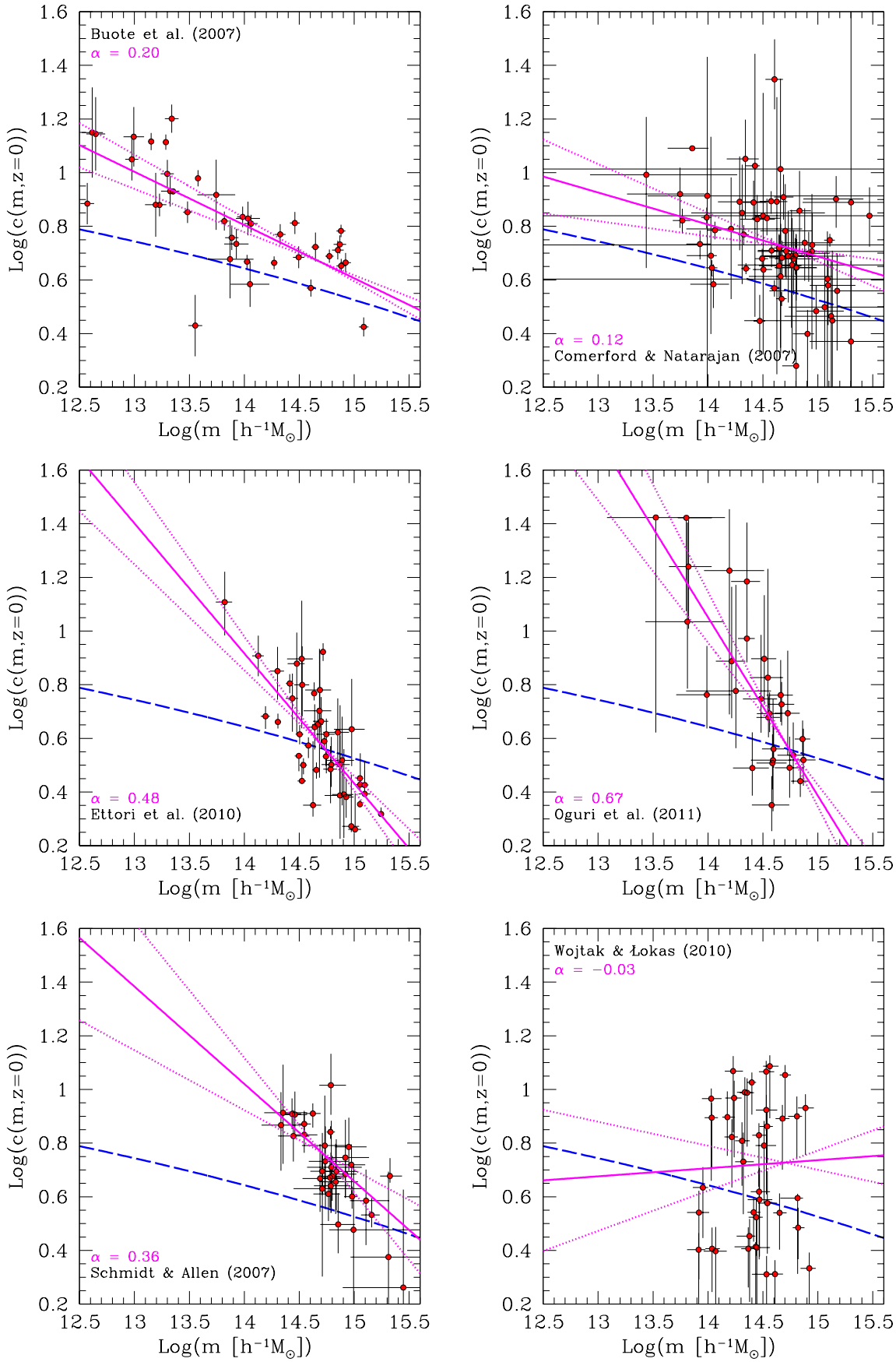


Figure 2.6: Observed $c - M$ relation for groups and galaxy clusters. The panels refer to different catalogs. In each panel, the solid pink line represents the best-fit of a power law relation $c \propto M^{-\alpha}$ to the observed points, with quoted slope $\alpha$, while the blue dashed line is the predicted $c - M$ relation from Gao et al. (2008). From Fedeli (2011).

# Chapter 3

# *Padme* Simulation: general properties

Since galaxy clusters occupy the highly non-linear regime of structure formation, we need numerical simulations to follow the evolution of density perturbations in this regime. In this chapter, we will introduce the *Padme* cosmological simulation set and discuss in detail its general properties. After a brief discussion of numerical simulations techniques in Section 3.1, in Section 3.2 the *Padme* simulation set will be discussed and in Section 3.3 the study of the mass functions of the selected sample will be analysed. Section 3.4 is centred on the analysis of the X-ray $L-T$ relation, while in Section 3.5 the X-ray observables functions will be studied. In Section 3.6 we will describe the analysis and the results of the study of the cluster baryon fraction, while conclusions will be drawn in Section 3.7. Most of the results presented in this chapter can be found in De Boni et al. (2011).

## 3.1 Numerical simulations

We begin this chapter by briefly reviewing the techniques used to perform cosmological numerical simulations similar to the ones used in this work. For extensive reviews, see Dolag et al. (2008) and Borgani & Kravtsov (2009). Depending on the problem under investigation, a numerical simulation is designed as a compromise between the simulated volume and the required resolution, given the amount of computational time. The typical sizes of the simulated volume range from 1 Mpc to 1 Gpc and the typical mass resolution varies from $10^5$ $M_\odot$ to $10^{10}$ $M_\odot$. Basically, numerical techniques can be split into two broad families: $N$-body codes to simulate the evolution of dark matter particles and hydrodynamical codes to simulate the behaviour of baryonic matter.

In $N$-body simulations, the cold dark matter can be described by a collisionless, non-relativistic fluid obeying the collisionless Boltzmann equation and the Poisson equation. The set of equations describing the motion of dark matter particles can be solved in different ways. The most straightforward way is to directly sum the contributions of dark matter particles to the gravitational potential. In principle, this should return the correct Newtonian potential, but, given the finite resolution of the simulations, it is necessary to introduce a softening length $\epsilon$ to reduce the two-body relaxation generated by the fact that the number of dark matter particles in the simulations is not big enough to fully represent a collisionless fluid. This method is the most accurate to solve the $N$-body problem but it is also computationally demanding, with the computing time scaling as $N^2$ if $N$ is the number of particles.
Another method to solve the $N$-body problem is the so-called tree algorithm. This method consists in grouping the particles into cells and treating distant groups as macroparticles. This reduces the computing time proportionality to $N \log N$. As a drawback, the final results

of the tree algorithm is only an approximation of the true gravitational force.
A third possibility is the Particle-Mesh (*PM*) method which computes the force on a mesh, by substituting differential operators with differences. The shortcoming of this technique is its limited resolution, counterbalanced by the fact that it is extremely fast. The computation time is proportional to $N + N_c \log N_c$, where $N_c$ is the number of mesh cells. Given the limited dynamical range, in cosmological simulations Adaptive Mesh Refinement (*AMR*) methods are required to follow the formation of individual objects.
Hybrid methods built by combining the particle-mesh and tree techniques can substantially improve the performance of the computation. In *TreePM* methods, the gravitational potential is split in a long-range term (computed with particle-mesh methods) and a short-range term (computed by tree algorithm). In comparison with the ordinary tree methods, in *TreePM* there is a gain in the accuracy of the long-range force. An example of a code using *TreePM* is the GADGET code (Springel, 2005), used here.

In hydrodynamical simulations, the baryonic content of the universe can be described as an ideal fluid obeying the Euler equation, the continuity equation and the first law of thermodynamics. Broadly speaking, the numerical schemes developed to solve the combined system of collisionless dark matter and collisional baryonic fluids fall into two categories: Eulerian (grid-based) methods and Lagrangian (particle-based) methods.
In Eulerian methods, the equations are solved on a grid representing the volume elements of the fluid, and the thermodynamical variables are evaluated at fixed points in the space. Modern methods do not consider the central value of the cell, but instead increase the order of accuracy through, *e.g.*, *piecewise parabolic method* (*PPM*). The main limitation of grid-based methods is given by spatial resolution, while they work remarkably well in describing shocks and both low- and high-density regions. Lagrangian methods are based on the smoothed particle hydrodynamics (SPH), which discretises the fluid in mass (particle) elements. SPH can achieve a good spatial resolution in high-density regions, but has limitations in low-density regions and has resolution problems in describing shocks, due to the presence of non-negligible artificial viscosity. Nevertheless, in cosmological context, the advantages of SPH compensate these drawbacks, making this scheme the most commonly used in cosmological hydrodynamical simulations. SPH methods are characterized by a smoothing length $h$ that, for each particle, describes the radius of a sphere containing $n$ neighbours particles. The choice of $n$, being a compromise between noise and systematics, depends on the problem under investigation.

Beyond these simple schemes of gravitational instability and hydrodynamical flows, in order to simulate more realistic cases, other astrophysical processes can be added in the numerical codes. Typical examples are cooling, star formation, supernova and AGN feedback, galactic winds. The inclusion of this additional physics is of fundamental importance if one wants to compare the results of numerical simulations with real observations.

## 3.2 *Padme* Simulation

In order to study the formation and evolution of large scale structures in the different cosmological scenarios introduced in Chapter 1, we use a set of cosmological simulations, called *Padme*, run by Klaus Dolag at the "Leibniz-Rechenzentrum" in Garching. *Padme* is a set of $N$-body and $N$-body + hydrodynamical simulations done with the GADGET-3 code (Springel et al., 2001; Springel, 2005), which makes use of the entropy-conserving formulation of SPH (Springel & Hernquist, 2002). We extended the dark energy implementation as described in Dolag et al. (2004) to allow the code to use an external, tabulated Hubble function as well as

a tabulated correction to the gravity constant needed for the extended quintessence models, as explained in Pettorino & Baccigalupi (2008). The hydrodynamical simulations include radiative cooling, heating by a uniform redshift-dependent UV background (Haardt & Madau, 1996), and a treatment of star formation and feedback processes. The prescription of star formation we use is based on a sub-resolution model to account for the multi-phase structure of the interstellar medium (ISM), where the cold phase of the ISM is the reservoir of star formation (Springel & Hernquist, 2003). Supernovae (SNe) heat the hot phase of the ISM and provide energy for evaporating some of the cold clouds, thereby leading to self-regulation of the star formation and an effective equation of state to describe its dynamics. As a phenomenological extension of this feedback scheme, Springel & Hernquist (2003) also included a simple model for galactic winds, whose velocity, $v_w$, scales with the fraction $\eta$ of the Type II SN feedback energy that contributes to the winds. The total energy provided by Type II SN is computed by assuming that they are due to exploding massive stars with mass $> 8$ M$_\odot$ from a Salpeter (1955) initial mass function, with each SN releasing $10^{51}$ ergs of energy. We have assumed $\eta = 0.5$, yielding $v_w \simeq 340$ km s$^{-1}$.

For the dark matter only $N$-body simulations, for each cosmological model, we simulated a cosmological box of size (300 Mpc $h^{-1}$)$^3$, resolved with $(768)^3$ dark matter particles with a mass of $m_{dm} \approx 4.4 \times 10^9$ M$_\odot$ $h^{-1}$. For the hydrodynamical simulations, for each cosmological model, we simulated a cosmological box of size (300 Mpc $h^{-1}$)$^3$, resolved with $(768)^3$ dark matter particles with a mass of $m_{DM} \approx 3.7 \times 10^9$ M$_\odot$ $h^{-1}$ and the same amount of gas particles, having a mass of $m_{gas} \approx 7.3 \times 10^8$ M$_\odot$ $h^{-1}$.

As in Dolag et al. (2004), we modified the initial conditions for the different dark energy scenarios adapting the initial redshift for the initial conditions in the dark energy scenarios determined by the ratio of the linear growth factors $D_+(z)$,

$$\frac{D_+(z_{\rm ini})}{D_+(0)} = \frac{D_{+,\Lambda{\rm CDM}}(z^{\rm ini}_{\Lambda{\rm CDM}})}{D_{+,\Lambda{\rm CDM}}(0)} \ . \tag{3.1}$$

Additionally, the peculiar velocities of the particles are corrected according to the new redshift to reflect a consistent application of the Zel'dovich approximation (Zel'dovich, 1970),[1]

$$\dot{x}(t) = \dot{D}_+(t) H(t) \nabla_q \Phi(\vec{q}) \ . \tag{3.2}$$

Finally we also correct the velocities of the particles due to the changed displacement field at the new redshift according to

$$\vec{v}^{\ {\rm ini}} = \vec{v}^{\ {\rm ini}}_{\Lambda{\rm CDM}} \frac{\dot{D}_+(z_{\rm ini})\, H(z_{\rm ini})}{\dot{D}_{+,\Lambda{\rm CDM}}(z^{\rm ini}_{\Lambda{\rm CDM}})\, H_{\Lambda{\rm CDM}}(z^{\rm ini}_{\Lambda{\rm CDM}})} \ . \tag{3.3}$$

Therefore, all simulations start from the same random phases, but the amplitude of the initial fluctuations is rescaled to satisfy the constraints given by CMB.

As a reference model we use the ΛCDM model, adapted to the WMAP3 values (Spergel et al., 2007), with the following cosmological parameters:

[1]Note that, unlike in previous works, here we do not use the approximation (2.10) $\Omega_m^{0.6}$ for $\dot{D}_+(t)$ as this would lead to small inaccuracies in some of the dark energy scenarios.

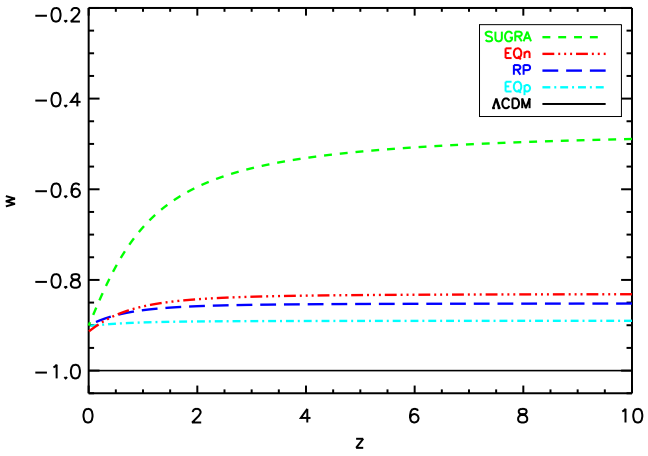


Figure 3.1: Redshift evolution of the equation of state parameter $w$ for the different cosmological models considered: ΛCDM (black), RP (blue), SUGRA (green), EQp (cyan), and EQn (red).

- matter density: $\Omega_{0m} = 0.268$
- dark energy density: $\Omega_{0\Lambda} = 0.732$
- baryon density: $\Omega_{0b} = 0.044$
- Hubble parameter: $h = 0.704$
- power spectrum normalization: $\sigma_8 = 0.776$
- spectral index: $n_s = 0.947$

We trimmed the parameters of the four dynamical dark energy models so that $w_0 = w(0) \approx -0.9$ is the highest value still consistent with observational constraints in order to amplify the effects of dark energy. Fig. 3.1 shows the evolution with redshift of $w$ in each cosmology. The parameters $\Omega_{0m}$, $\Omega_{0\Lambda}$, $\Omega_{0b}$, $h$, and $n_s$ are the same for all the models, but since we normalize all the dark energy models to CMB data from WMAP3, this leads to different values of $\sigma_8$ for the different cosmologies:

$$\sigma_{8,\mathrm{DE}} = \sigma_{8,\Lambda\mathrm{CDM}} \frac{D_{+,\Lambda\mathrm{CDM}}(z_{\mathrm{CMB}})}{D_{+,\mathrm{DE}}(z_{\mathrm{CMB}})} \ , \tag{3.4}$$

assuming $z_{\mathrm{CMB}} = 1089$. This fact, along with the different evolution of the growth factor $D_+$ (shown in Fig. 3.2), has an impact on structure formation. In Fig. 3.3 we plot the star formation rate density (SFRD) as a function of redshift for all the models considered. The SFRD in general follows the growth of the perturbations as shown in Fig. 3.2. Table 3.1 lists the parameters chosen for the different cosmological models.

In Fig. 3.4 we show a density slice of depth equal to 1/64 of the box size through the whole box for each of the five models considered at $z = 0$. At first sight, we can see that the structures form in the same place in the different cosmologies since the initial phases are the same. Moreover, the differences among the models are small and cannot be seen with the eye; indeed, an accurate statistical analysis is needed to understand the properties of the objects in the different models.

Table 3.1: Parameters chosen for the different cosmological models: $\alpha$ is the exponent of the inverse power law potential; $\xi$ is the coupling in the extended quintessence models; $w_{\rm JBD0}$ is the present value of the parameter introduced in equation (1.77); $w_0$ is the present value of the equation of state parameter for dark energy; $\sigma_8$ is the normalization of the power spectrum as in equation (3.4).

| Model | $\alpha$ | $\xi$ | $w_{\rm JBD0}$ | $w_0$ | $\sigma_8$ |
|---|---|---|---|---|---|
| ΛCDM | — | — | — | $-1.0$ | 0.776 |
| RP | 0.347 | — | — | $-0.9$ | 0.746 |
| SUGRA | 2.259 | — | — | $-0.9$ | 0.686 |
| EQp | 0.229 | $+0.085$ | 120 | $-0.9$ | 0.748 |
| EQn | 0.435 | $-0.072$ | 120 | $-0.9$ | 0.729 |

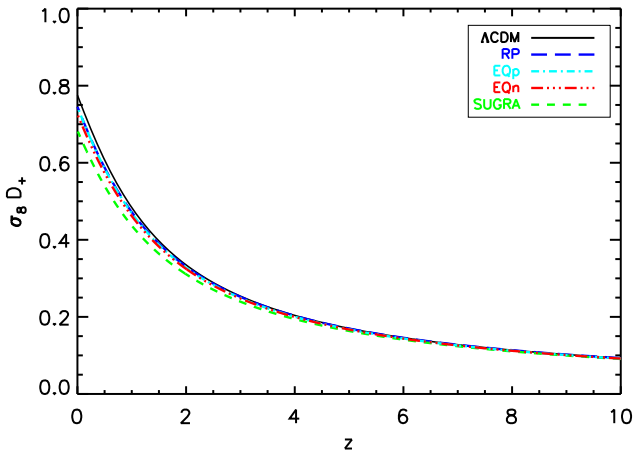


Figure 3.2: Redshift evolution of the growth factor $D_+$, normalized to the corresponding $\sigma_8$, for the different cosmological models considered: ΛCDM (black), RP (blue), SUGRA (green), EQp (cyan), and EQn (red).

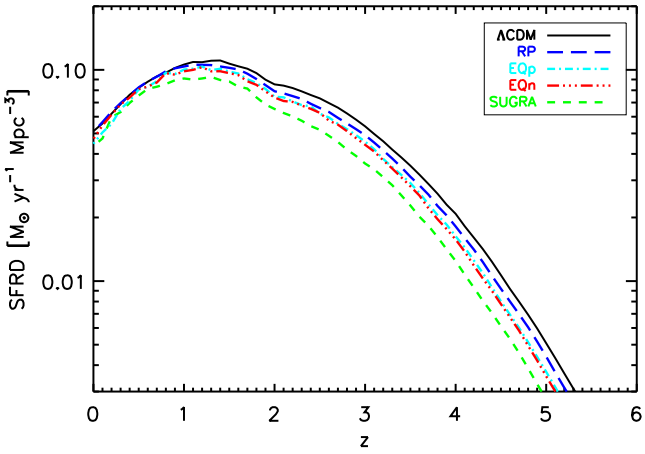


Figure 3.3: SFRD as a function of redshift for the ΛCDM model (black), RP (blue), SUGRA (green), EQp (cyan), and EQn (red) cosmologies.

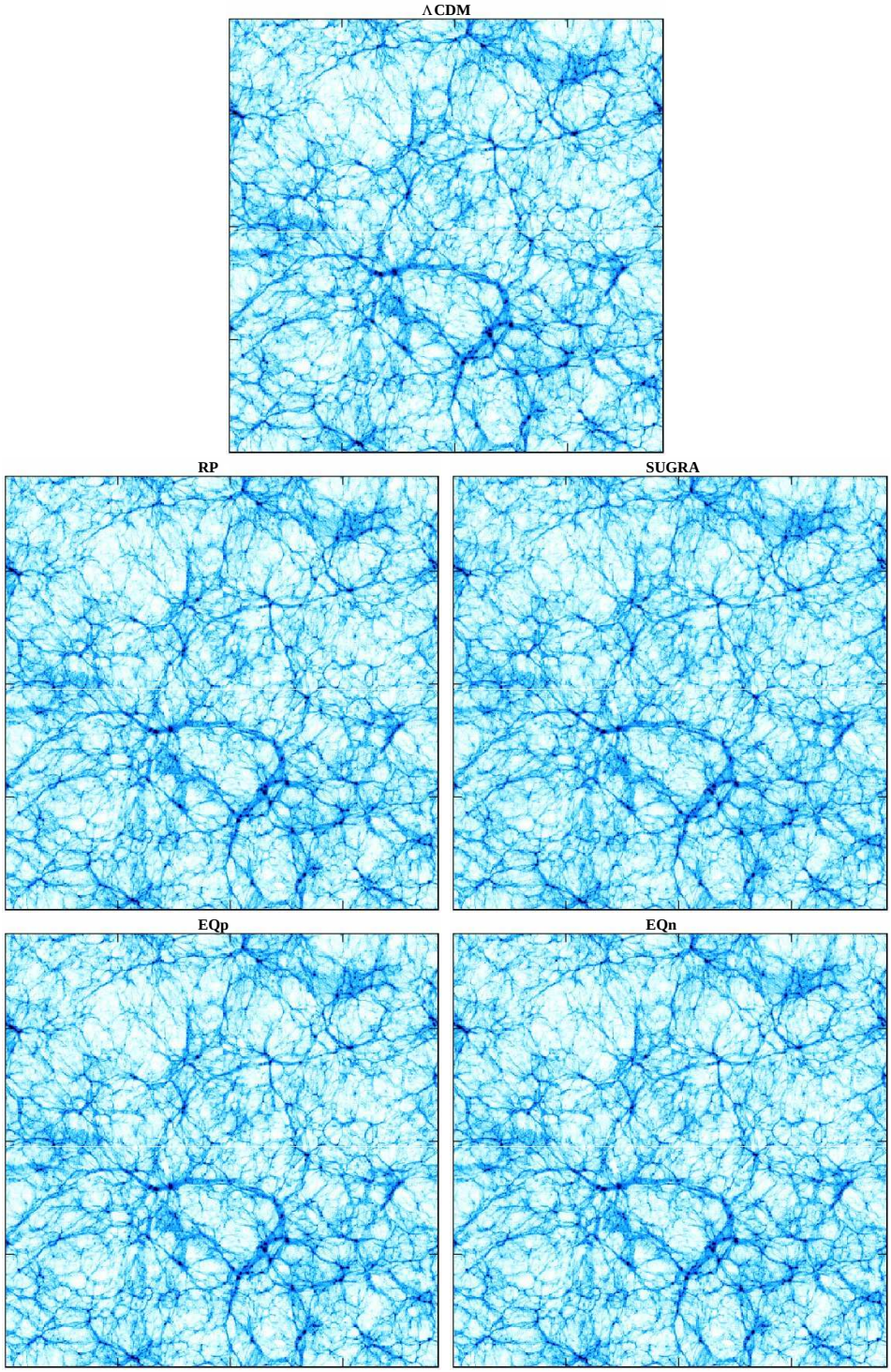


Figure 3.4: Density slice of depth equal to 1/64 of the box size through the whole simulation box for the five different models at $z = 0$.

Using the outputs of simulations, we extract galaxy clusters from the cosmological boxes, using the spherical overdensity criterion to define the collapsed structures. We take as halo centre the position of the most bound particle. Around this particle, we construct spherical shells of matter and stop when the total (*i.e.* dark matter plus gas plus stars) overdensity drops below 200 times the *mean* (as opposed to *critical*) background density defined by $\Omega_{0m}\rho_{0c}$; the radius so defined is denoted with $R_{200m}$ and the mass enclosed in it as $M_{200m}$. For this part of the work, we consider only halos that have $M_{200m} > 1.42 \times 10^{14}$ $M_\odot$ (corresponding to $M_{200m} > 10^{14}$ $M_\odot$ $h^{-1}$). We select and study objects at three different redshifts, $z = 0$, $z = 0.5$, and $z = 1$. For the following analysis, we also calculate for each cluster selected in this way the radius at which the overdensity drops below 200 (500) times the *critical* background density and denote it with $R_{200}$ ($R_{500}$). The corresponding mass is indicated as $M_{200}$ ($M_{500}$). Just as a reference, the most massive object of all the simulations has $M_{200m} = 3.15 \times 10^{15}$ $M_\odot$. The number of clusters at each redshift is different for each cosmology: for example, the sample at $z = 0$ is made up by 563 clusters in the ΛCDM cosmology, 484 in RP, 352 in SUGRA, 476 in EQp, and 431 in EQn. This fact directly reflects the different values of $\sigma_8$ and $D_+$ leading to differences in the formation history of the halos. No morphological selection has been made on the sample considered, so that clusters in very different dynamical state are included. Nevertheless, it is useful to define a quantitative criterion to decide whether a cluster can be considered relaxed or not because, in general, relaxed clusters have more spherical shapes, better defined centres and thus are more representative of the self-similar behaviour of the dark matter halos. We use a simple criterion similar to that introduced in Neto et al. (2007): first of all we define $x_{off}$ as the distance between the centre of the halo (given by the most bound particle) and the barycentre of the region included in $R_{200m}$; then we define as relaxed the halos for which $x_{off} < 0.07 R_{200m}$.

## 3.3 Mass function

As we have seen in Chapter 2, a standard way to use galaxy clusters as cosmological probe is the study of their mass function. Since the total mass of these objects is dominated by dark matter, it is a tracer of structure formation in different cosmological models. In the top panel of Fig. 3.5 we plot the cumulative mass functions for the different cosmologies at three different redshifts: $z = 0$, $z = 0.5$ and $z = 1$. This plot simply illustrates the number of halos per unit volume having a total mass greater than a given mass threshold. We can see that the shape and the properties of the mass functions are substantially the same at different redshifts (with the obvious exception of the maximum mass of the formed halos), with ΛCDM forming more clusters of a given mass compared to the other cosmologies; SUGRA is the cosmology which forms fewer clusters, while RP, EQp and EQn lie in between, with RP and EQp being the closest to ΛCDM. This fact seems to directly reflect the redshift evolution of the equation of state parameter $w$ (see Fig. 3.1) and of the growth factor (see Fig. 3.2), given the different value of $\sigma_8$ in the different models. Actually, for extended quintessence models, a positive value of the coupling $\xi$ leads to $\tilde{G} > G_*$ in the past, and vice versa for a negative $\xi$. Therefore, the linear density contrast is expected to be higher for EQp than for EQn. In a spherical collapse model like the Press-Schechter formalism (Press & Schechter, 1974), this implies a higher mass function for models with negative coupling (*i.e.* EQn) than for models with positive coupling (*i.e.* EQp), when all the other parameters are kept fixed (see Subsection 2.1.3). In our case, this effect is somehow mitigated by the different $\sigma_8$ used.

In the bottom panel of Fig. 3.5 we plot (always at $z = 0$, $z = 0.5$ and $z = 1$) the ratios between the number of clusters in a given dark energy model with respect to the corresponding

Table 3.2: Ratios between the number of clusters in the simulated volume for a given dark energy model with respect to $N_{\Lambda CDM}$ in the given $M_{200m}$ bin at different redshifts.

| $M_{200m}$ [$10^{14}$ $M_\odot$] | $z$ | $N_{\Lambda CDM}$ | RP | SUGRA | EQp | EQn |
|---|---|---|---|---|---|---|
| $> 1.42$ | 0 | 563 | 0.86 | 0.63 | 0.85 | 0.77 |
| $> 1.42$ | 0.5 | 202 | 0.81 | 0.52 | 0.80 | 0.69 |
| $> 1.42$ | 1 | 45 | 0.78 | 0.47 | 0.76 | 0.64 |
| | | | | | | |
| $1.42 - 5$ | 0 | 507 | 0.88 | 0.65 | 0.86 | 0.78 |
| $5 - 10$ | 0 | 45 | 0.69 | 0.42 | 0.69 | 0.67 |
| $> 10$ | 0 | 11 | 0.82 | 0.36 | 0.82 | 0.64 |

value in ΛCDM. For each cosmology, we consider only bins in which we have more than one object. The same results are summarized also in Table 3.2. At $z = 0$, RP, EQp, EQn, and SUGRA form 86%, 85%, 77%, and 63% the number of objects formed in ΛCDM, respectively. These numbers decrease with increasing redshift, reaching, at $z = 1$, 78%, 76%, 64%, and 47% for RP, EQp, EQn, and SUGRA, respectively. This fact indicates that the differences in the formation history are more evident at high redshift. If we consider different mass bins at $z = 0$, we see that the differences between ΛCDM and the other models are enhanced for very massive objects, in particular for SUGRA.

Note that we have considered here minimally coupled models and scalar-tensor theories, as illustrated in Chapter 1. Couplings with dark matter only, where, as in equation (1.85), an additional velocity-dependent term is present, have been shown to lead to different results (Baldi & Pettorino, 2011), increasing the number of massive clusters at high redshift. Differences between these sets of models have been illustrated in detail in Pettorino & Baccigalupi (2008).

In principle, if we can count all the clusters above a given mass threshold, or in a given mass bin, we can try to discriminate between different cosmologies just using cluster number counts coming from cosmological surveys. From a practical point of view, evaluating the mass of galaxy clusters requires the assumption of some hypotheses on their dynamical state, and in general it is not an easy task to perform. So it is better to consider cluster properties that are directly observable (like X-ray luminosity and temperature) in order to distinguish among different cosmologies. We discuss these topics in the next two sections.

In Fig. 3.6 we show the cumulative $M_{500}$ mass functions for our five cosmological models at $z = 0$ and $z = 0.5$ and, as a comparison, the observed ΛCDM mass functions for the $z = 0.025 - 0.25$ and $z = 0.45 - 0.55$ samples of Vikhlinin et al. (2009b) (see Subsection 2.2.3). If we take our ΛCDM model as a reference, we see that, within error bars, there is a good agreement between our mass function at $z = 0$ and both observed data and theoretical predictions. The discrepancy we see in the high-mass tail of the mass function is due to sample variance caused by the finite size of our cosmological box. We discuss in more detail the issue of the box size in Section 3.5, but we note here that the last three points of our mass function, corresponding to $6 \times 10^{14}$ $M_\odot$, $7 \times 10^{14}$ $M_\odot$, and $8 \times 10^{14}$ $M_\odot$, represent 4, 2, and 1 objects respectively. We are using Poissonian errors $\sigma_N = N^{1/2}$, where $N$ is the number of objects, but a better approximation when $N$ is small is $\sigma_N \sim 1 + (N + 0.75)^{1/2}$ (see *e.g.* Gehrels, 1986). At $z = 0.5$ there is a consistent agreement between our mass function and the predicted one, while there is some tension with the data, which show a deficit at intermediate masses as already noted by Vikhlinin et al. (2009b).

It is interesting to compare the observed mass function of Vikhlinin et al. (2009b) with the one that we can recover by applying their $M_{tot} - Y_X$ relation

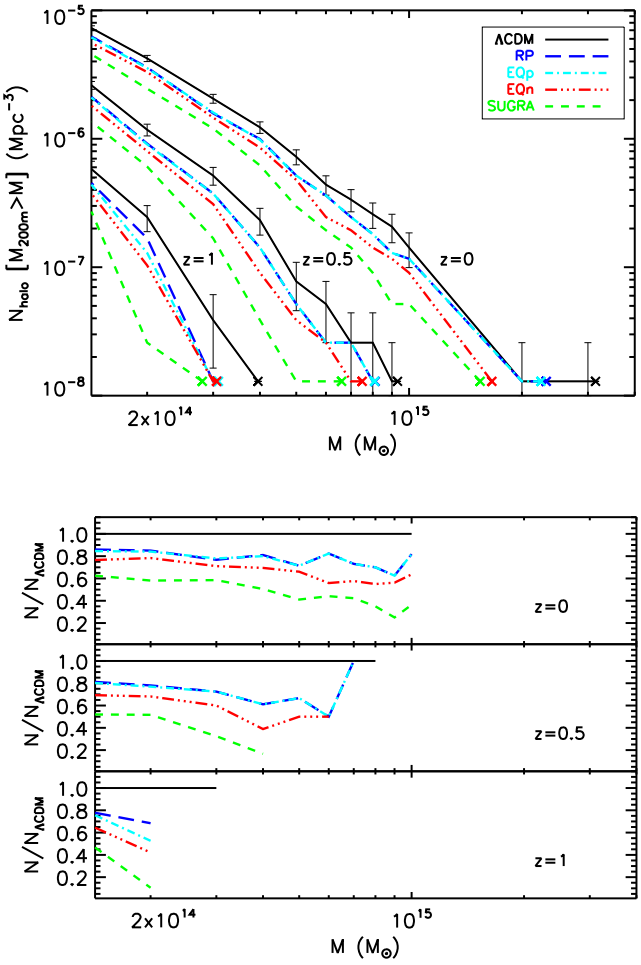


Figure 3.5: (Top panel) Cumulative mass function at $z = 0$, $z = 0.5$ and $z = 1$ for the ΛCDM (black), RP (blue), SUGRA (green), EQp (cyan), and EQn (red) cosmologies. For each cosmological model the mass of the most massive object at each redshift is marked by a cross. Error bars (shown only for ΛCDM for clarity reasons) are Poissonian errors for the cluster number counts. (Bottom panel) Ratios between the mass functions for different dark energy cosmologies and the corresponding values for ΛCDM at $z = 0$, $z = 0.5$ and $z = 1$.

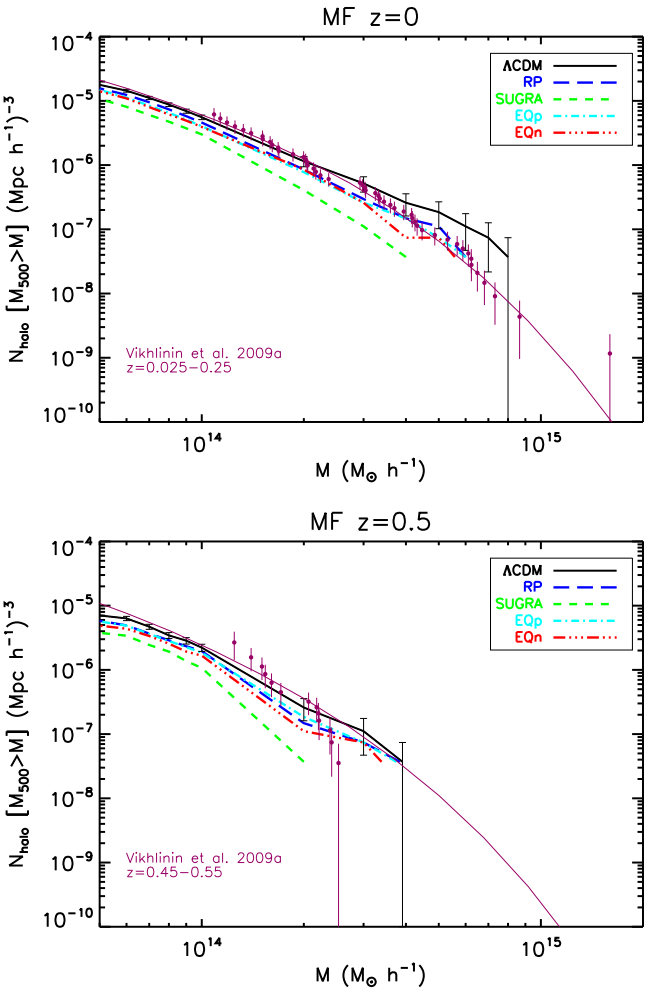


Figure 3.6: (Top panel) Cumulative $M_{500}$ mass function at $z = 0$ for the ΛCDM (black), RP (blue), SUGRA (green), EQp (cyan), and EQn (red) cosmologies. Error bars (shown only for ΛCDM for clarity reasons) are Poissonian errors for the cluster number counts. The violet points are observed data from the $z = 0.025 - 0.25$ sample of Vikhlinin et al. (2009b). The violet line shows the prediction from Tinker et al. (2008) for the adapted cosmological model ($\Omega_m = 0.28$, $\Omega_\Lambda = 0.72$, $h = 0.72$), with only $\sigma_8 = 0.746$ fit to the cluster data. (Bottom panel) The same as in the top panel, but for $z = 0.5$ and observed data from the $z = 0.45 - 0.55$ sample of Vikhlinin et al. (2009b).

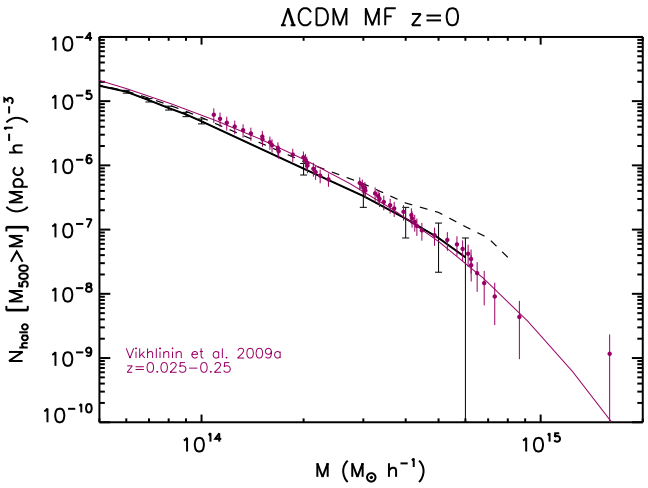


Figure 3.7: Cumulative $M_{500}$ mass function at $z = 0$ (dashed black line) and mass function recovered from the $Y_{X500}$ parameter (solid black line) for the ΛCDM cosmology. Error bars are Poissonian errors for the cluster number counts. The violet points are observed data from the $z = 0.025 - 0.25$ sample of Vikhlinin et al. (2009b). The violet line shows the prediction from Tinker et al. (2008) for the adapted cosmological model ($\Omega_m = 0.28$, $\Omega_\Lambda = 0.72$, $h = 0.72$), with only $\sigma_8 = 0.746$ fit to the cluster data.

$$M_{500} = 5.77 \times 10^{14}\ \mathrm{M}_\odot\ h^{1/2} (Y_X/3 \times 10^{14}\ \mathrm{M}_\odot\ \mathrm{keV})^{0.57} E(z)^{-2/5}\ , \tag{3.5}$$

to our clusters. We will discuss the X-ray properties of our simulated clusters in the next two sections, but we anticipate in Fig. 3.7 the results for the mass function. We see that the agreement between our recovered mass function, the observed data and the theoretical model is remarkable, while there is some discrepancy between the true mass function and the recovered one. Still, the differences at a given mass are of the order of few objects, well within the variance due to the finite size of the simulated box and the slightly different values of $\sigma_8$.

## 3.4 $L - T$ relation

Once we have analysed the general composition of our sample, we can now proceed with the study of the properties of the objects inside the sample. We recall that, when considering self-similar evolution of gravitational systems, we can derive simple scaling relations between their properties. The existence of such scaling relations is confirmed by observations, even if in general they have a different shape compared to the ones predicted by self-similarity, indicating an important role of some non-gravitational physics in the evolution of these systems (see Subsection 2.2.3). We use the hydrodynamical runs of the *Padme* simulation set in order to understand whether the baryon physics introduces any scale dependence that can break the self-similarity of the scaling relations. Since one of the aims of this work is to study whether there exist observable quantities that can be used to distinguish among the different cosmologies considered, we start studying the X-ray $L - T$ relation of our sample, also comparing it to observations to verify that the observed relation holds for our simulated objects too. In order to do that, for each cluster we want to analyse we produce 2D maps of (5 Mpc)$^2$ size of the X-ray luminosity $L_X$ and emission-weighted temperature $T_{ew}$ in the $[0.5 - 2]$ keV soft band. The latter is defined by

$$T_{ew} \equiv \frac{\int \Lambda(T) n^2 T dV}{\int \Lambda(T) n^2 dV} \ , \tag{3.6}$$

where $n$ is the gas density and $\Lambda(T)$ is the cooling function. As an example, we show in Fig. 3.8 the 2D X-ray luminosity and emission-weighted temperature maps of two objects extracted from the ΛCDM box at $z = 0$, one non cool-core cluster and one cool-core cluster (see Subsection 2.2.1). In particular, the non cool-core system is the most massive cluster in the whole *Padme* simulation set, while the cool-core one is a typical example of relaxed cluster.
Then, for each object, we evaluate the total luminosity and the emission-weighted temperature in the region $[0.15 - 1]R_{500}$. We decide to cut the core for two reasons: first of all, despite the fact we use accurate physical models to describe the hydrodynamics of the simulations, still we do not include AGN feedback, so they are not optimized for the study of the central regions of the clusters; secondly, we have checked that cutting the core we obtain a lower dispersion of our data in the $L - T$ plane. We stress that despite excluding the central region of the clusters in our analysis we can still draw robust conclusions from a cosmological point of view, avoiding the effects of detailed physical processes which can affect the inner parts. Moreover this cut is often used in observations to avoid problems with cool-core emission that can lead to a deviation from the self-similar scaling relation. Having generated luminosity and temperature catalogues of our sample, we can proceed with the analysis of the $L - T$ relation.

In the top panel of Fig. 3.9 we plot the $L-T$ relation at different redshifts ($z = 0$, $z = 0.5$ and $z = 1$) for the ΛCDM cosmology. Here we correct the luminosity using $E_z^{-1} \equiv H_0/H$, which is a factor containing all the predicted dependence on the cosmology (see *e.g.* Ettori et al., 2004). We can see that there are not substantial differences at the various redshifts, but in general at high redshift we lack clusters in the luminosity region below $10^{43}$ erg s$^{-1}$ and in the temperature region below 2 keV. This fact can be explained as a selection effect in our sample: at high redshift, only more evolved (and thus more luminous and hotter) clusters are massive enough to be included in our sample. We also provide a fit to our points, fitting the linear relation between the logarithms of luminosity and temperature. We find a slope of 1.81, which is slightly higher than the self-similar value of 1.5 expected for the soft band considered. Finally we plot a collection of observed data at different redshifts compiled by Pratt et al. (2009). The luminosities are taken exactly in the same way as we did, *i.e.* in the $[0.15 - 1]R_{500}$ region and in the $[0.5 - 2]$ keV band, while they use spectroscopically determined temperatures (see the details in Pratt et al., 2009). The slope of their best-fit relation is $2.53 \pm 0.16$, steeper than what we found. Despite the difference in the slope, we can see that in the high-temperature/high-luminosity region where we have a sufficient number of both observed and simulated objects, the agreement is very good. In any case, we stress that a direct comparison between simulations and observations is not the main target of this work. Here, we just want to show that our simulated clusters lie in a region in the $L - T$ plane which is the same as the observed objects. Regarding the differences we find in the low-temperature/low-luminosity region, we stress that it is not due to overcooling in the simulations, since we are cutting the core; more likely, this region is populated by objects with lower mass, for which the detailed physical processes acting in the inner regions (*e.g.* AGN feedback) have important effects also on the overall properties of the clusters (see *e.g.* Puchwein et al., 2008).

In the bottom panel of Fig. 3.9 we plot the evolution with redshift of the mean luminosity and temperature in the different cosmologies. We consider only the relaxed clusters at $z = 0$,

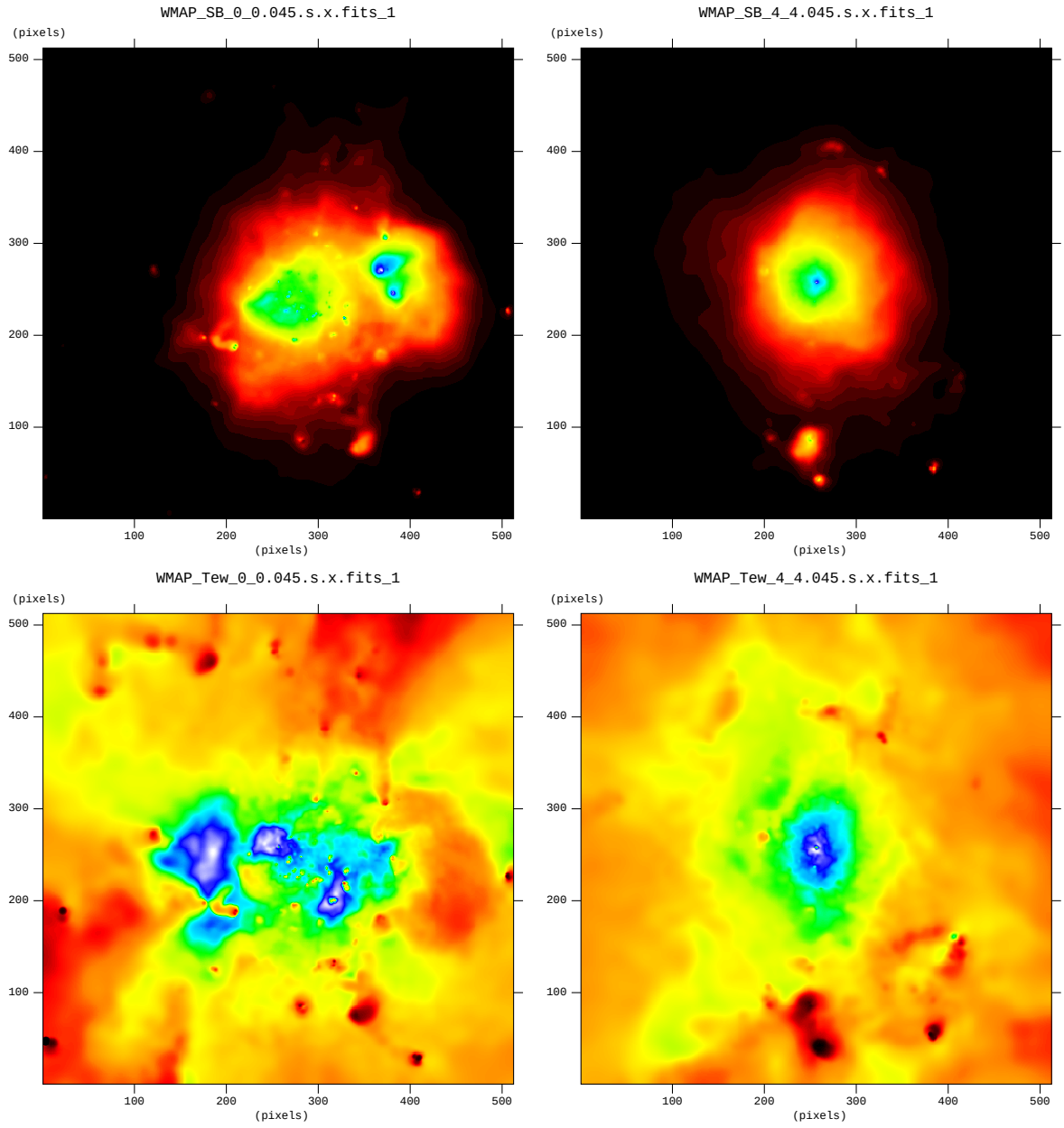


Figure 3.8: (Top panel) 2D maps of the X-ray luminosity in the $[0.5-2]$ keV soft band for two objects extracted from the $\Lambda$CDM box at $z = 0$, one non cool-core cluster (left) and one cool-core cluster (right). (Bottom panel) 2D maps of the X-ray emission weighted temperature in the $[0.5-2]$ keV soft band for the same two object as in the top panel. The size of each map is $(5\mathrm{Mpc})^2$.

$z = 0.5$ and $z = 1$. Then, for each cosmology, we select the ten most massive objects at each redshift, using $M_{200}$ for this selection. Actually, at $z = 1$ for the SUGRA model we only have six relaxed clusters, and we consider all of them. At this point, at each redshift, we evaluate the mean luminosity and temperature of the selected objects both in the region inside $R_{500}$ and in the region $[0.15 - 1]R_{500}$. We find that cutting the core results in both a lower mean luminosity and lower mean emission-weighted temperature. As a general trend, either including or cutting the core, both the mean luminosity and temperature increase with decreasing redshift, independently of the cosmological model. This is in somehow expected, since at late cosmic time the clusters are more evolved, and thus hotter and more luminous. The differences in the values of mean luminosity and temperature among the different cosmologies reflect the different histories experienced by objects in different dark energy environments, substantially following the mass function.

## 3.5 X-ray observable functions

Using the same maps built to study the X-ray $L - T$ relation, we can also analyse the X-ray luminosity function (XLF) and the X-ray temperature function (XTF) of our samples. Since the samples are mass selected (see Section 3.3), only the mass functions we have shown before can be considered complete. XLFs and XTFs in a sense reflect the mass functions, but cannot be considered complete for the selection effect discussed in the previous section. This means that at higher redshift, we are missing more and more clusters in the low-luminosity region of the XLF and in the low-temperature region of the XTF. We show in Fig. 3.10 the cumulative XLFs and XTFs of our sample at $z = 0$. We cut the plots at $0.1 \times 10^{44}$ erg s$^{-1}$ and 1 keV in order to be as complete as possible also in the low-luminosity and low-temperature regions. In the top panel of Fig. 3.10 we show the cumulative luminosity function. In the middle panel of the same figure we plot the ratios between the number of clusters in a given dark energy model with respect to ΛCDM in every luminosity bin. As in the case of the mass function, for each cosmology, we consider only bins in which we have more than one object. The results for three luminosity bins are also summarized in Table 3.3. In general, despite some noisy oscillations, the ratio is decreasing with increasing luminosity. Nevertheless, in the range between 0.5 and $1 \times 10^{44}$ erg s$^{-1}$ it increases and in three models out of four the number of objects is equal or even larger than in ΛCDM. This effect seems to be statistically significant in particular for RP. In any case, by looking only at very luminous objects, the differences with ΛCDM are significant for all models.

In the bottom panel of Fig. 3.10 we show the same as in the top panel, but for the cumulative temperature function (see also Table 3.3). In this case, the decrease of the ratio with increasing temperature is evident in all the dynamical dark energy cosmologies. Going from objects in the range between 1 and 3 keV to objects with temperatures higher than 3 keV, RP goes from 87% to 70%, SUGRA from 64% to 33%, EQp from 86% to 57%, and EQn from 78% to 43%.

In general, we see that the relative trend among the different cosmologies shown by the mass functions at $z = 0$ is almost preserved in the XLFs and XTFs: in a given mass, luminosity and temperature bin, ΛCDM forms more clusters than the other cosmologies do (except for RP in a luminosity bin, as noted before). On the other hand, SUGRA is the cosmological model that forms fewer clusters in each bin. EQp and EQn lie in between. This finding is confirmed by the bottom panels of Fig. 3.10 where we show the ratios between the XLFs and XTFs plotted in the top panels and the ones recovered by applying the $L - M$ relation at $z = 0$ for the ΛCDM cosmology to the mass functions of each dark energy model. This is

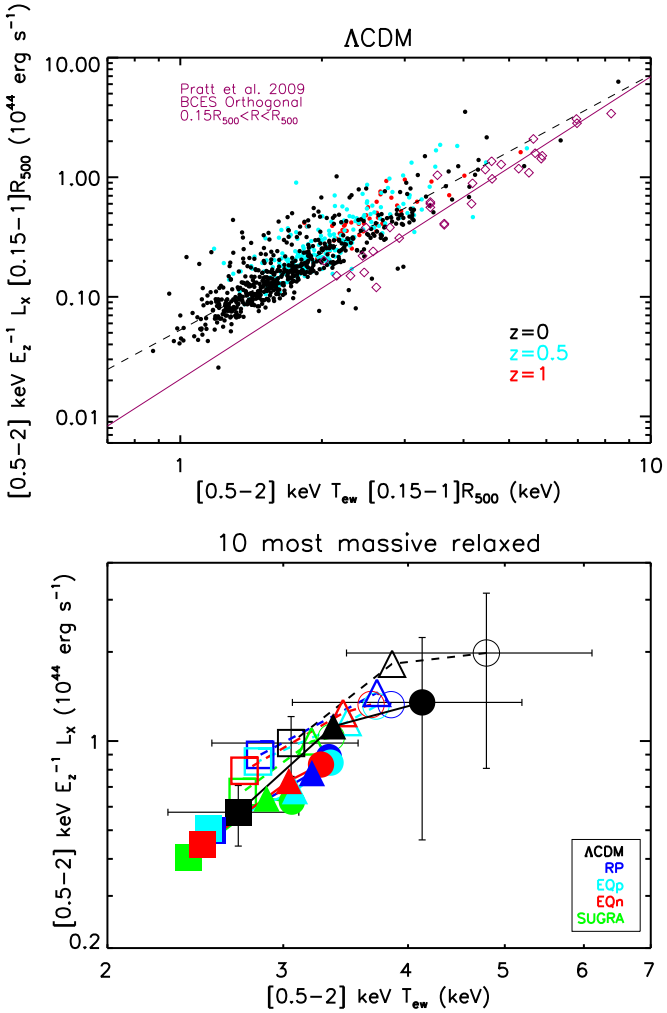


Figure 3.9: (Top panel) The X-ray $L-T$ relation in the $[0.5-2]$ keV band, evaluated in the $[0.15-1]R_{500}$ region at $z = 0$ (black), $z = 0.5$ (cyan), and $z = 1$ (red) for the ΛCDM cosmology. The dashed black line is the best-fit of our simulated data. The violet squares are a collection of observed data from Pratt et al. (2009), while the violet line is their best-fit of the same dataset. (Bottom panel) Redshift evolution of the mean luminosity and temperature in the $[0.5-2]$ keV band for the ten most massive relaxed objects in the ΛCDM (black), RP (blue), SUGRA (green), EQp (cyan), and EQn (red) cosmologies. Circles refer to objects at $z = 0$, triangles to objects at $z = 0.5$ and squares to objects at $z = 1$. Dashed lines and empty symbols indicate the evolution of the mean luminosity and temperature evaluated inside $R_{500}$, while solid lines and filled symbols refer to the same quantities evaluated in the $[0.15-1]R_{500}$ region. In both panels, the cosmological dependence is taken into account using the factor $E_z^{-1} \equiv H_0/H$ which multiplies the luminosity.

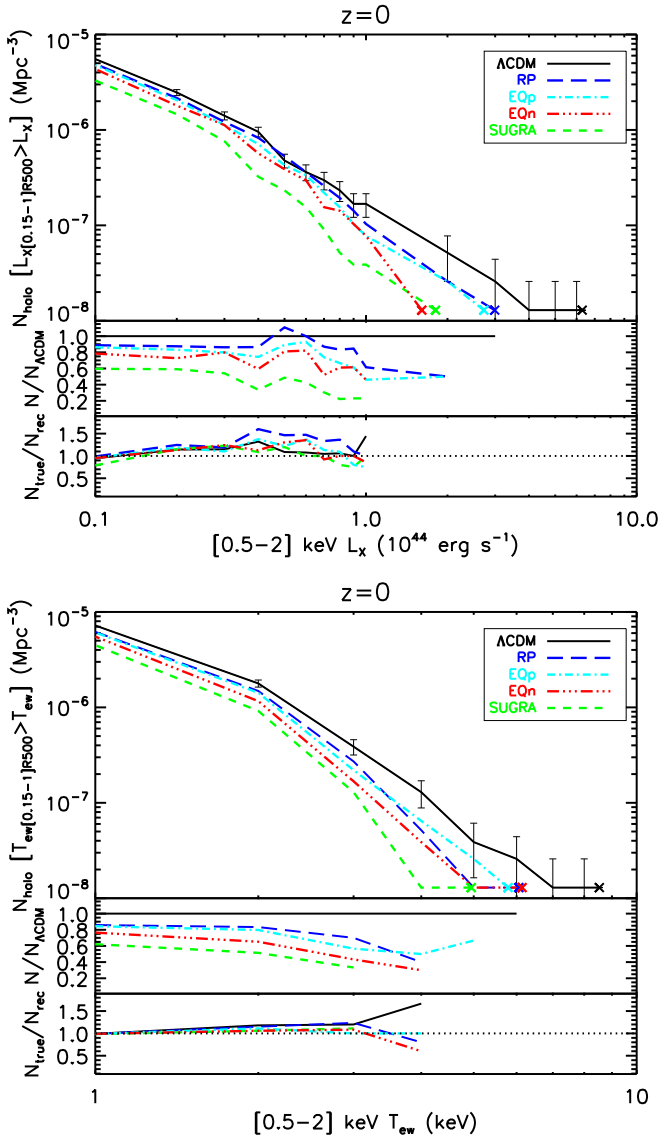


Figure 3.10: (Top panel) The X-ray luminosity function (XLF) in the $[0.5-2]$ keV band, evaluated in the $[0.15-1]R_{500}$ region at $z=0$ for the ΛCDM (black), RP (blue), SUGRA (green), EQp (cyan), and EQn (red) cosmologies. For each cosmological model the luminosity of the object with the highest luminosity is marked by a cross. Error bars (shown only for ΛCDM for clarity reasons) are Poissonian errors for the cluster number counts. In the middle panel the ratios between the luminosity functions for different dark energy cosmologies and the corresponding values for ΛCDM are shown. In the bottom panel we plot the ratio between the luminosity functions shown in the top panel and the ones recovered by applying the $L-M$ relation at $z=0$ for the ΛCDM cosmology to the mass function of each dark energy model. (Bottom panel) The same as in the top panel, but for the X-ray temperature function (XTF).

Table 3.3: Ratios between the number of clusters in the simulated volume for a given dark energy model with respect to $N_{\Lambda CDM}$ in the given $L_X$, $T_{ew}$, $M_{gas500}$, and $Y_{X500}$ bin.

| $z = 0$ | $N_{\Lambda CDM}$ | RP | SUGRA | EQp | EQn |
|---|---|---|---|---|---|
| $L_X$ [$10^{44}$ erg s$^{-1}$] | | | | | |
| $0.1 - 0.5$ | 391 | 0.87 | 0.61 | 0.86 | 0.78 |
| $0.5 - 1$ | 24 | 1.38 | 0.63 | 1.13 | 1.00 |
| $> 1$ | 13 | 0.62 | 0.23 | 0.46 | 0.46 |
| $T_{ew}$ [keV] | | | | | |
| $1 - 3$ | 528 | 0.87 | 0.64 | 0.86 | 0.78 |
| $> 3$ | 30 | 0.70 | 0.33 | 0.57 | 0.43 |
| $M_{gas500}$ [$10^{13}$ M$_\odot$] | | | | | |
| $1 - 5$ | 347 | 0.85 | 0.58 | 0.81 | 0.76 |
| $> 5$ | 14 | 0.50 | 0.21 | 0.43 | 0.50 |
| $Y_{X500}$ [$10^{13}$ M$_\odot$ keV] | | | | | |
| $1 - 5$ | 392 | 0.87 | 0.63 | 0.82 | 0.79 |
| $5 - 10$ | 55 | 0.98 | 0.49 | 0.96 | 0.96 |
| $> 10$ | 29 | 0.69 | 0.38 | 0.62 | 0.66 |

done to disentangle the differences in the XLFs and XTFs due to a different mass function and the ones due to baryon physics. The fact that the subsample considered in the bottom panel of Fig. 3.9 reproduces the XLF and XTF of Fig. 3.10 also seems to indicate that relaxed and massive objects are still a good representation of the whole sample. The general trend of the mass, luminosity and temperature functions seems to reflect the evolution with redshift of the dark energy equation of state parameter $w = w(z)$, as we showed in Fig. 3.1. ΛCDM tends to form massive clusters earlier than the other cosmologies, thus giving a larger number of evolved (*i.e.* with high luminosity and temperature) objects at $z = 0$. The XTF seems to better reflect the mass function, while the XLF is more influenced by baryonic physics, as we can clearly see from the behaviour of the RP cosmology. So, in principle, we can try to distinguish among different cosmologies by building the XTF of a sample of galaxy clusters. The problem is that if we check, for example, the sample from Pratt et al. (2009), there are very few clusters in the temperature range we have considered for our XTF. Being an X-ray selected sample, in general they have a higher temperature compared with our simulated objects, and so it is not easy to directly compare our results with their observational data.

In order to check whether other proxies could better trace the formation history of structures, we also analysed the X-ray $M_{gas500}$ and $Y_{X500}$ functions. $M_{gas500}$ is defined simply by the mass of X-ray emitting gas contained in $R_{500}$, while $Y_{X500} = M_{gas500} \times T_{ew}$, where $T_{ew}$ is evaluated in the $[0.15 - 1]R_{500}$ region. We plot these functions in Fig. 3.11. We see from Table 3.3 that, for $M_{gas500} > 5 \times 10^{13}$ M$_\odot$, $M_{gas500}$ is in principle a very powerful tool to distinguish between different cosmologies. In fact, all the models form at most 50% the number of objects formed by ΛCDM, and, since $M_{gas500}$ is quite an easy quantity to estimate from observations, it should be possible to rule out some models just by studying the $M_{gas500}$ function. The quantity $Y_{X500}$ does not seem to be as good as $M_{gas500}$, since the differences between ΛCDM and the other models are less pronounced, and also the behaviour in the different bins is not so smooth.

It is interesting to evaluate the volume that a cluster survey must cover to be able to discriminate using the local (*i.e.* at $z = 0$) cluster counts among the different dark energy models here considered. For that we assume Poissonian error bars and consider a $3\sigma$ level, where $\sigma$ is linked to the volume by

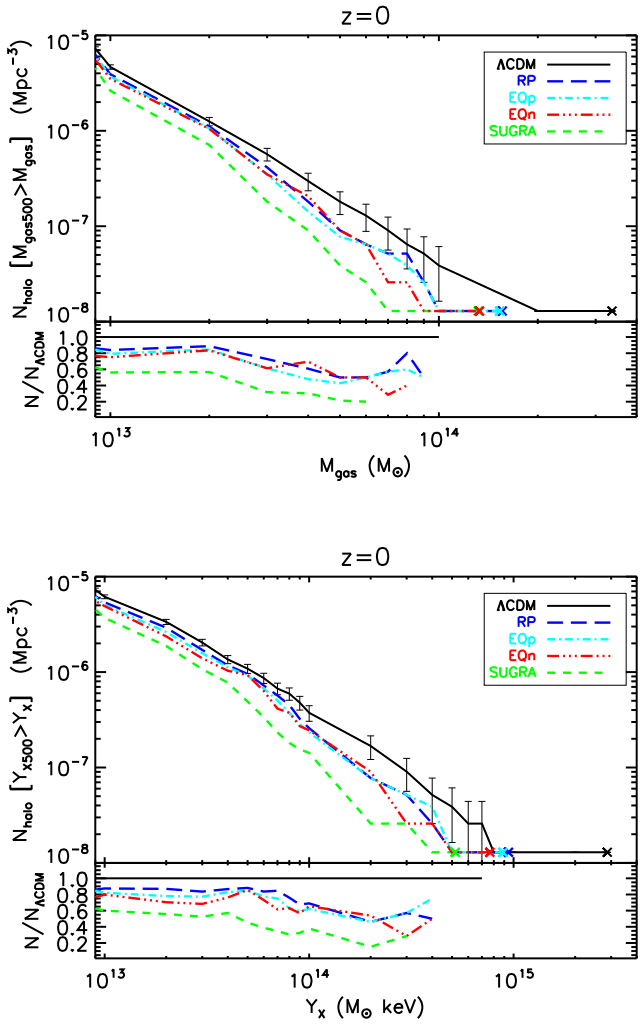


Figure 3.11: (Top panel) The $M_{gas500}$ function at $z = 0$ for the ΛCDM (black), RP (blue), SUGRA (green), EQp (cyan), and EQn (red) cosmologies. For each cosmological model the gas mass of the most massive object is marked by a cross. Error bars (shown only for ΛCDM for clarity reasons) are Poissonian errors for the cluster number counts. In the middle panel the ratios between the gas mass functions for different dark energy cosmologies and the corresponding values for ΛCDM are shown. (Bottom panel) The same as in the top panel, but for the $Y_{X500}$ function.

$$\sigma = \sqrt{Vol}\frac{|MF_{\Lambda\mathrm{CDM}} - MF_{\mathrm{DE}}|}{\sqrt{MF_{\Lambda\mathrm{CDM}} + MF_{\mathrm{DE}}}} \ , \tag{3.7}$$

where $MF$ can be the mass function, or any other X-ray observable function linked to cluster number counts. We plot the results for the mass function at $z = 0$ and $z = 1$ in Fig. 3.12, while the results for the XLF and XTF are shown in Fig. 3.13.
Using the mass function with a threshold of $5 \times 10^{14}$ $\mathrm{M}_{\odot}$, we find that cosmological volumes larger than $1.6 \times 10^7 (\mathrm{Mpc}\ h^{-1})^3$ are sufficient to distinguish between SUGRA and ΛCDM, while $6.4 \times 10^7 (\mathrm{Mpc}\ h^{-1})^3$ are required for EQn and $9.1 \times 10^7 (\mathrm{Mpc}\ h^{-1})^3$ are required for RP and EQp. Considering the XLF (with a threshold of $0.5 \times 10^{44}$ erg $\mathrm{s}^{-1}$), larger surveys are required: in fact volumes larger than $4.3 \times 10^7$, $3.4 \times 10^8$, $1 \times 10^9$, and $1.3 \times 10^9 (\mathrm{Mpc}\ h^{-1})^3$ are necessary to discriminate among SUGRA, EQn, EQp, and RP and ΛCDM, respectively. The situation is better when the XTF (with a threshold of 3 keV) is used: predictions for the ΛCDM model are different at $3\sigma$ level with respect to the ones for SUGRA, EQn, EQp, and RP, when volumes as large as $2.7 \times 10^7$, $4.3 \times 10^7$, $6.4 \times 10^7$, and $1.7 \times 10^8 (\mathrm{Mpc}\ h^{-1})^3$ are considered, respectively. This fact confirms the importance of XLF/XTF in tracing the number counts in a given cosmology, and again that the XTF is a better quantity to be used in that kind of studies, if compared to the XLF. We recall that we are not considering any selection function on XLF/XTF, being a proper treatment of any observational approach in defining an XLF/XTF beyond the purpose of the present work. If we move to $z = 1$, using the mass function with a threshold of $1.42 \times 10^{14} \mathrm{M}_{\odot}$, $2.7 \times 10^7 (\mathrm{Mpc}\ h^{-1})^3$ are still sufficient to distinguish between SUGRA and ΛCDM, while EQn, EQp, and RP need $6.4 \times 10^7 (\mathrm{Mpc}\ h^{-1})^3$, $1.7 \times 10^8 (\mathrm{Mpc}\ h^{-1})^3$, and $2.2 \times 10^8 (\mathrm{Mpc}\ h^{-1})^3$ to be distinguished from ΛCDM, respectively. Larger cosmological boxes and larger observational samples with higher resolution and sensitivity (*i.e.* lower flux limit), such as, *e.g.*, the one expected with eROSITA (Predehl et al., 2007) and WFXT (Giacconi et al., 2009), can provide better answers to the question.

## 3.6 The baryon fraction

In this section we focus on the baryon fraction $f_{bar} = f_{star} + f_{gas}$ of our simulated galaxy clusters, where $f_{star} \equiv M_{star}/M_{tot}$ and $f_{gas} \equiv M_{gas}/M_{tot}$. Since we are considering galaxy clusters in a cosmological context, it is better to re-express the star fraction $f_{star}$, the gas fraction $f_{gas}$, and the total baryon fraction $f_{bar}$ in units of the cosmic baryon fraction $\Omega_{0b}/\Omega_{0m} = 0.164$ adopted in these simulations. To do this we introduce the quantities

$$b_{star} \equiv \frac{f_{star}}{\Omega_{0b}/\Omega_{0m}} \ ; \quad b_{gas} \equiv \frac{f_{gas}}{\Omega_{0b}/\Omega_{0m}} \ ; \quad b_{bar} \equiv \frac{f_{bar}}{\Omega_{0b}/\Omega_{0m}} \ , \tag{3.8}$$

and indicate them as star, gas and baryon depletion parameter, respectively. In this section we analyse the dependence of these quantities on mass, redshift and distance from the centre of the object considered, as well as on the underlying cosmology.

In Fig. 3.14 we plot the distribution of $b_{bar}$, $b_{gas}$ and $b_{star}$ evaluated at $R_{200}$ for the whole sample at $z = 0$, $z = 0.5$, and $z = 1$ in order to check the spread of the values for the single objects. We see that at $z = 0$ there is a substantial overlapping among the different cosmologies, indicating that evolved objects have almost the same distribution whatever the underlying cosmological background is. The same is true looking at $z = 0.5$ and $z = 1$. We

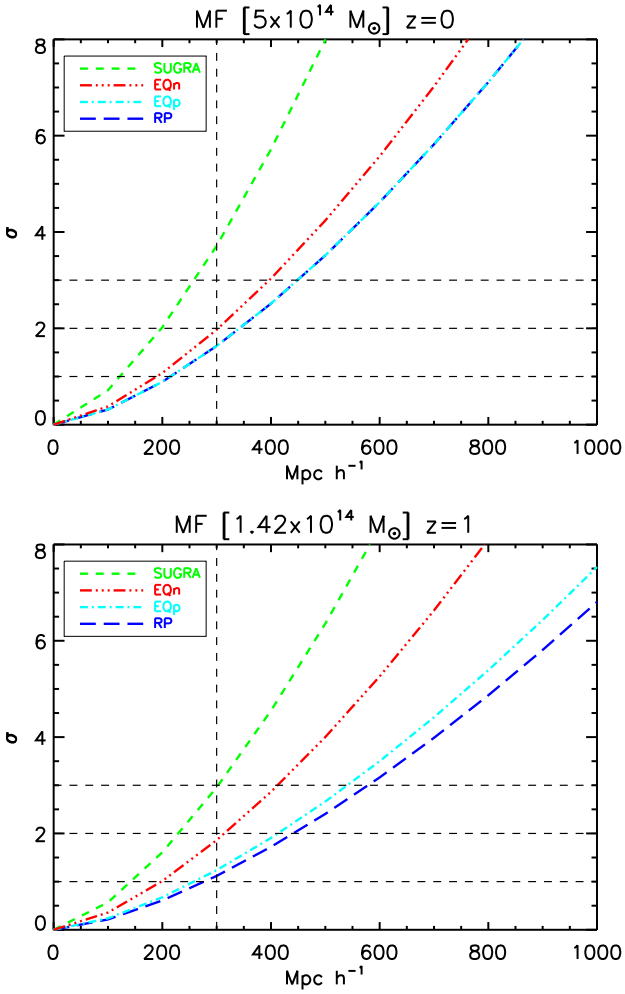


Figure 3.12: (Top panel) Confidence level as a function of box size to discriminate between the RP (blue), SUGRA (green), EQp (cyan), and EQn (red) cosmologies and the ΛCDM cosmology using the mass function with a threshold of $5 \times 10^{14}$ $M_\odot$ at $z = 0$. (Bottom panel) The same as in the top panel, but for the mass function with a threshold of $1.42 \times 10^{14}$ $M_\odot$ at $z = 1$.

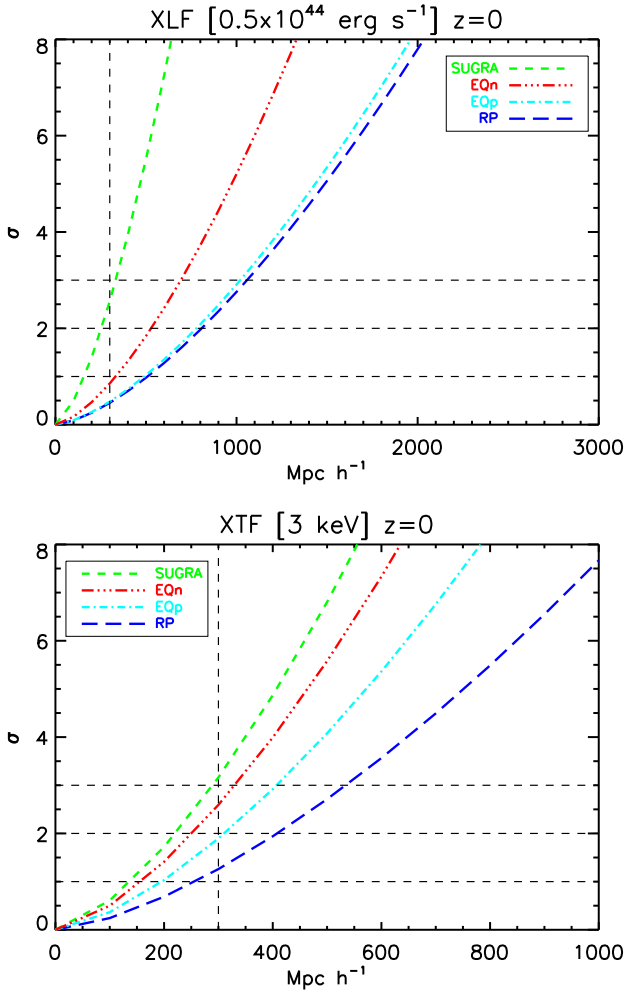


Figure 3.13: (Top panel) Confidence level as a function of box size to discriminate between the RP (blue), SUGRA (green), EQp (cyan), and EQn (red) cosmologies and the ΛCDM cosmology using the X-ray luminosity function (XLF) with a threshold of $0.5 \times 10^{44}$ erg s$^{-1}$ at $z = 0$. (Bottom panel) The same as in the top panel, but for the X-ray temperature function (XTF) with a threshold of 3 keV at $z = 0$.

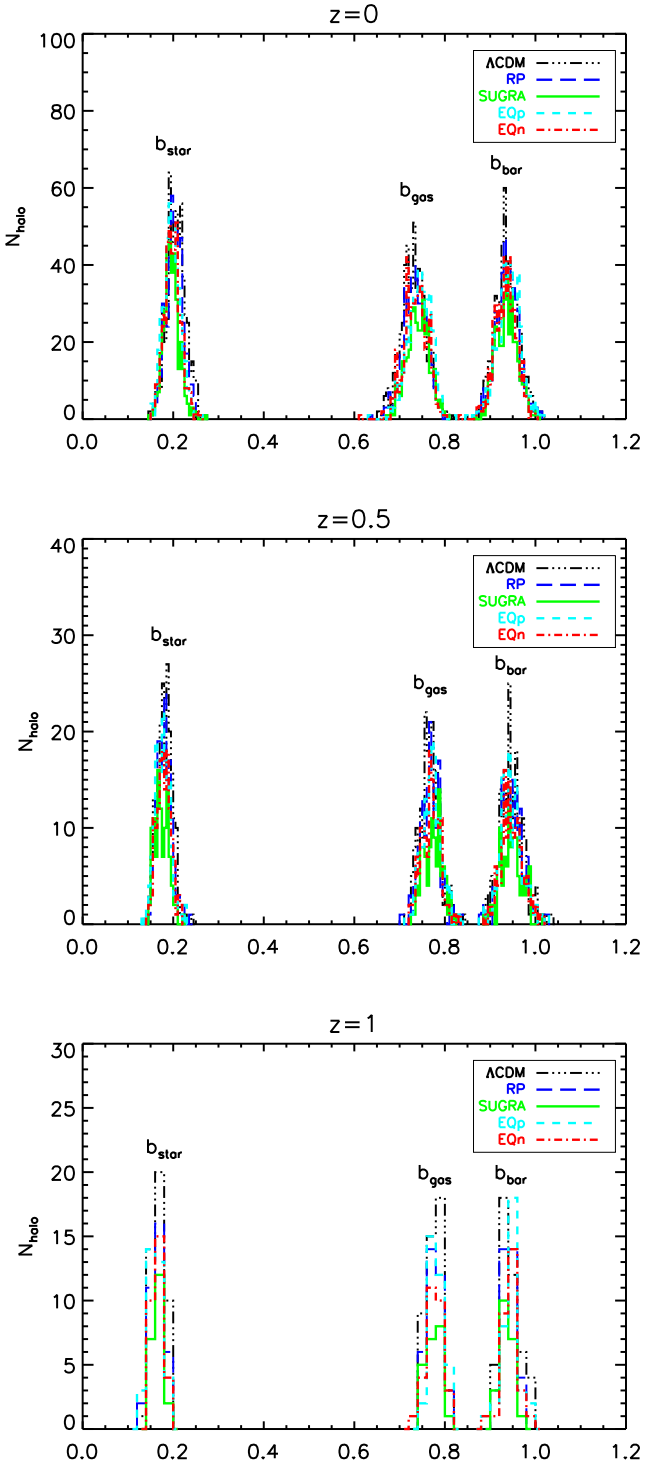


Figure 3.14: Distribution of $b_{bar}$, $b_{gas}$, and $b_{star}$ evaluated at $R_{200}$ for the ΛCDM (black), RP (blue), SUGRA (green), EQp (cyan), and EQn (red) cosmologies at $z = 0$ (top panel), $z = 0.5$ (middle panel), and $z = 1$ (bottom panel).

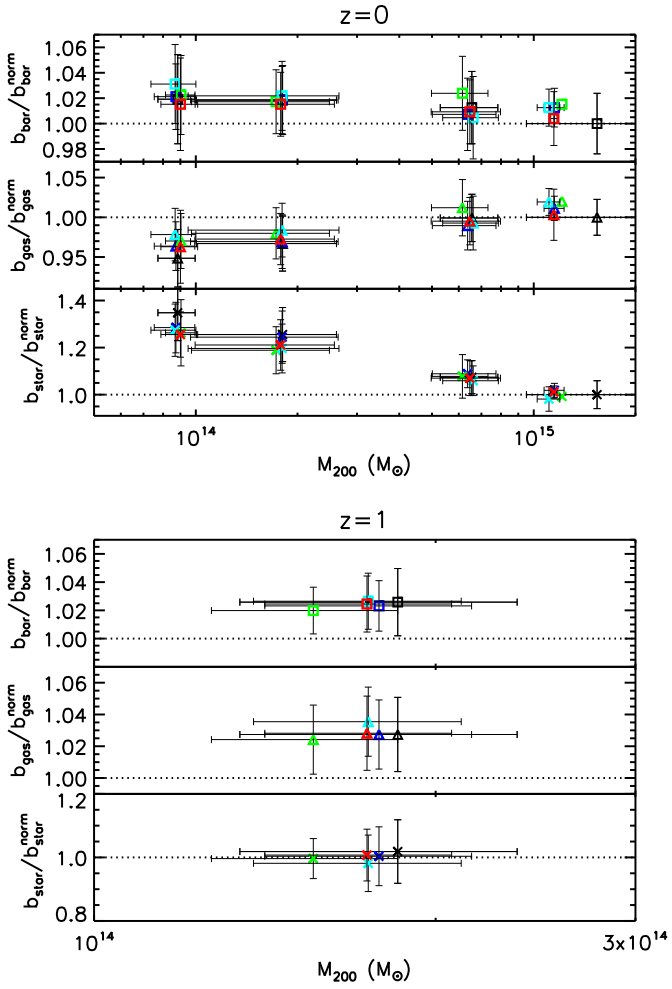


Figure 3.15: The evolution of stellar, gas and baryon depletion parameter evaluated at $R_{200}$ with mass at $z = 0$ (top panel) and $z = 1$ (bottom panel) for the ΛCDM (black), RP (blue), SUGRA (green), EQp (cyan), and EQn (red) cosmologies. Crosses, triangles, and squares indicate $b_{star}$, $b_{gas}$, and $b_{bar}$ respectively. The depletion parameters are expressed in units of $b_{bar}^{norm}$, $b_{gas}^{norm}$ and $b_{star}^{norm}$, the mean values for clusters with $M_{200} \geq 10^{15}\mathrm{M}_{\odot}$ in the ΛCDM cosmology at $z = 0$. Error bars are r.m.s. of the mean distribution.

can note a decrease of $b_{gas}$ going from $z = 1$ to $z = 0$, not completely compensated by an increase of $b_{star}$. The net effect is a decrease of $b_{bar}$ going from $z = 1$ to $z = 0$.

In Table 3.4 we summarize the mean value of $b_{star}$, $b_{gas}$, and $b_{bar}$ evaluated at $R_{2500}$, $R_{500}$, and $R_{200}$ for all the objects in the different cosmological models considered, at $z = 0$, $z = 0.5$, and $z = 1$. We see that, on the one hand, for any cosmological model, at any redshift, $b_{star}$ is a decreasing function of radius, going from $R_{2500}$ to $R_{200}$. On the other hand, $b_{gas}$ is an increasing function of radius. As a whole, $b_{bar}$ is slightly decreasing with radius. Fixing the radius, either $R_{2500}$, $R_{500}$, or $R_{200}$, $b_{star}$ increases going from $z = 1$ to $z = 0$, while $b_{gas}$ decreases. As we already noted from Fig. 3.14, $b_{bar}$ is slightly decreasing going from $z = 1$ to $z = 0$. These trends are general, and they hold for all the cosmological models considered.

In the top panel of Fig. 3.15 we plot, for each cosmology, the ratio between the mean values of $b_{bar}$, $b_{gas}$ and $b_{star}$ evaluated at $R_{200}$ in four different mass ranges at $z = 0$ and the mean value of $b_{bar}^{norm}$, $b_{gas}^{norm}$ and $b_{star}^{norm}$ for clusters having $M_{200} \geq 10^{15}\mathrm{M}_{\odot}$ in the ΛCDM

Table 3.4: Mean values of $b_{star}$, $b_{gas}$, and $b_{bar}$ evaluated at $R_{2500}$, $R_{500}$, and $R_{200}$ for all the objects in the different cosmological models considered, at $z = 0$, $z = 0.5$, and $z = 1$. N indicates the number of objects in the given model at the given redshift. Numbers in brackets are $1\sigma$ errors on the mean.

| Model | $z$ | N | $b_{star2500}$ | $b_{gas2500}$ | $b_{bar2500}$ | $b_{star500}$ | $b_{gas500}$ | $b_{bar500}$ | $b_{star200}$ | $b_{gas200}$ | $b_{bar200}$ |
|---|---|---|---|---|---|---|---|---|---|---|---|
| ΛCDM | 0 | 563 | 0.508 | 0.535 | 1.043 | 0.269 | 0.680 | 0.948 | 0.207 | 0.731 | 0.937 |
| | | | (0.072) | (0.067) | (0.065) | (0.032) | (0.037) | (0.036) | (0.021) | (0.027) | (0.026) |
| | 0.5 | 202 | 0.461 | 0.578 | 1.039 | 0.236 | 0.724 | 0.961 | 0.182 | 0.767 | 0.949 |
| | | | (0.063) | (0.055) | (0.065) | (0.025) | (0.028) | (0.032) | (0.017) | (0.022) | (0.027) |
| | 1 | 45 | 0.454 | 0.624 | 1.078 | 0.222 | 0.749 | 0.971 | 0.168 | 0.777 | 0.944 |
| | | | (0.082) | (0.063) | (0.068) | (0.029) | (0.027) | (0.035) | (0.016) | (0.018) | (0.022) |
| RP | 0 | 484 | 0.498 | 0.541 | 1.039 | 0.263 | 0.683 | 0.946 | 0.204 | 0.733 | 0.937 |
| | | | (0.069) | (0.066) | (0.063) | (0.029) | (0.037) | (0.036) | (0.019) | (0.026) | (0.024) |
| | 0.5 | 164 | 0.452 | 0.589 | 1.041 | 0.234 | 0.726 | 0.960 | 0.181 | 0.767 | 0.948 |
| | | | (0.061) | (0.059) | (0.069) | (0.025) | (0.031) | (0.032) | (0.016) | (0.022) | (0.026) |
| | 1 | 35 | 0.429 | 0.633 | 1.063 | 0.218 | 0.754 | 0.972 | 0.165 | 0.777 | 0.942 |
| | | | (0.070) | (0.062) | (0.073) | (0.026) | (0.025) | (0.031) | (0.015) | (0.017) | (0.016) |
| SUGRA | 0 | 352 | 0.520 | 0.549 | 1.069 | 0.260 | 0.693 | 0.953 | 0.196 | 0.740 | 0.937 |
| | | | (0.076) | (0.066) | (0.066) | (0.029) | (0.036) | (0.035) | (0.018) | (0.025) | (0.024) |
| | 0.5 | 105 | 0.442 | 0.602 | 1.044 | 0.226 | 0.736 | 0.962 | 0.174 | 0.773 | 0.947 |
| | | | (0.066) | (0.054) | (0.064) | (0.025) | (0.028) | (0.029) | (0.015) | (0.021) | (0.024) |
| | 1 | 21 | 0.435 | 0.628 | 1.063 | 0.215 | 0.750 | 0.964 | 0.164 | 0.774 | 0.939 |
| | | | (0.063) | (0.069) | (0.089) | (0.021) | (0.027) | (0.040) | (0.010) | (0.016) | (0.015) |
| EQp | 0 | 476 | 0.515 | 0.554 | 1.069 | 0.258 | 0.689 | 0.947 | 0.197 | 0.744 | 0.941 |
| | | | (0.078) | (0.068) | (0.075) | (0.030) | (0.037) | (0.036) | (0.018) | (0.026) | (0.026) |
| | 0.5 | 162 | 0.444 | 0.597 | 1.042 | 0.228 | 0.731 | 0.959 | 0.176 | 0.770 | 0.946 |
| | | | (0.061) | (0.058) | (0.61) | (0.024) | (0.031) | (0.033) | (0.016) | (0.022) | (0.026) |
| | 1 | 34 | 0.429 | 0.625 | 1.054 | 0.213 | 0.760 | 0.973 | 0.162 | 0.783 | 0.944 |
| | | | (0.072) | (0.064) | (0.078) | (0.026) | (0.026) | (0.031) | (0.015) | (0.016) | (0.018) |
| EQn | 0 | 431 | 0.508 | 0.545 | 1.053 | 0.258 | 0.689 | 0.947 | 0.199 | 0.736 | 0.934 |
| | | | (0.070) | (0.058) | (0.070) | (0.028) | (0.034) | (0.034) | (0.018) | (0.025) | (0.024) |
| | 0.5 | 140 | 0.452 | 0.599 | 1.052 | 0.234 | 0.729 | 0.963 | 0.179 | 0.769 | 0.948 |
| | | | (0.063) | (0.063) | (0.054) | (0.024) | (0.028) | (0.032) | (0.016) | (0.020) | (0.024) |
| | 1 | 29 | 0.427 | 0.626 | 1.053 | 0.216 | 0.753 | 0.969 | 0.166 | 0.777 | 0.943 |
| | | | (0.068) | (0.065) | (0.071) | (0.026) | (0.026) | (0.031) | (0.013) | (0.017) | (0.018) |

cosmology at $z = 0$ (*i.e.* 0.921, 0.757 and 0.165 respectively). We have considered four mass ranges: $M_{200} < 10^{14}$ M$_\odot$, $10^{14}$ M$_\odot \leq M_{200} < 5 \times 10^{14}$ M$_\odot$, $5 \times 10^{14}$ M$_\odot \leq M_{200} < 10^{15}$ M$_\odot$, and $M_{200} \geq 10^{15}$M$_\odot$. We have evaluated the quantities at $R_{200}$ instead of $R_{500}$ as in Section 3.4 because this radius is representative of the cluster as a whole, including the external regions, and indeed we want to check whether, in different cosmologies, these objects are a fair representation of the underlying background. The first thing we notice is that, in every mass bin, the values of $b_{bar}$, $b_{gas}$ and $b_{star}$ are similar, within error bars, among the different cosmologies. So we can refer to a single cosmology (*e.g.* ΛCDM) in order to study the mass dependence of these quantities. We see that $b_{bar}$ is almost constant, independently of mass. On the one hand, $b_{gas}$ shows a slight positive trend, of the order of 5%, going from low-mass to high-mass systems, but still compatible with a constant value within the error bars. On the other hand, $b_{star}$ shows a decrease up to 30% going from low-mass to high-mass clusters, not compatible with a constant value. In the bottom panel of Fig. 3.15 we plot, for each cosmology, the ratio between $b_{bar}$, $b_{gas}$ and $b_{star}$ evaluated at $R_{200}$ at $z = 1$ and the mean values for ΛCDM at $z = 0$ already used in the top panel. In this case we do not consider different mass ranges, since at this redshift the cluster abundance starts to be low and all the objects have $10^{14}$ M$_\odot \leq M_{200} < 5 \times 10^{14}$ M$_\odot$. Again, the cosmologies are completely equivalent within error bars.

Here we stress again that our simulations do not follow AGN feedback. It is known from literature (*e.g.* Puchwein et al., 2008) that the effect of this feedback is mass dependent, leading to a lowering in the baryon fraction in groups and low-mass clusters, without affecting significantly high-mass clusters.

We find in general a constant baryon fraction with respect to the mass. Some authors (*e.g.* Giodini et al., 2009) claim that in observed objects the total baryon fraction shows an increase with increasing mass. This difference with respect to our results could be due to the fact that some relevant physical processes are still not included in our cosmological simulations. Such processes may be able to affect the global properties of low-mass systems without changing the high-mass clusters. Not including them in the simulations does not permit to us to fully compare our results with observations. In particular, we note an overabundance of stars (which obviously influences the total baryon fraction) in low-mass objects.

Combining the top and bottom panels of Fig. 3.15, we can study the evolution with redshift of $b_{bar}$, $b_{gas}$ and $b_{star}$. Since the differences among various cosmologies at the same redshift are quite small, we rely on our reference ΛCDM model for the analysis of redshift evolution. For clusters with $10^{14}$ M$_\odot \leq M_{200} < 5 \times 10^{14}$ M$_\odot$, the mean value of $b_{bar}$ is almost constant, with a slight decrease of about 2%, going from $z = 1$ to $z = 0$. In particular, $b_{gas}$ decreases of less than 10%, while the increase of $b_{star}$ is of the order of 25%. A decrease of the baryon fraction with decreasing redshift was already found in other simulations (see *e.g.* Ettori et al., 2006), and a possible explanation is that at high redshift the radius at which the baryons accrete is smaller than at low redshift, and so a greater number of baryons can fall in the cluster potential well.

Finally, we study the star, gas, and baryon depletion parameters as a function of the distance from the centre of the cluster, defined as the position of the most bound particle. For each cosmology we select, as in Section 3.4, the ten most massive (in $M_{200}$) relaxed halos and generate the radial profile of the object obtained by stacking them. We do this at $z = 0$, $z = 0.5$ and $z = 1$. We recall that, at $z = 1$, for SUGRA we only have six objects. The resulting profiles, expressed in units of the cosmic baryon fraction $\Omega_{0b}/\Omega_{0m} = 0.164$, are shown in Fig. 3.16. At $z = 0$, in the outer regions near $R_{200}$, the five cosmologies are completely equivalent, with $b_{bar}$ having almost the cosmological value, while looking toward the centre

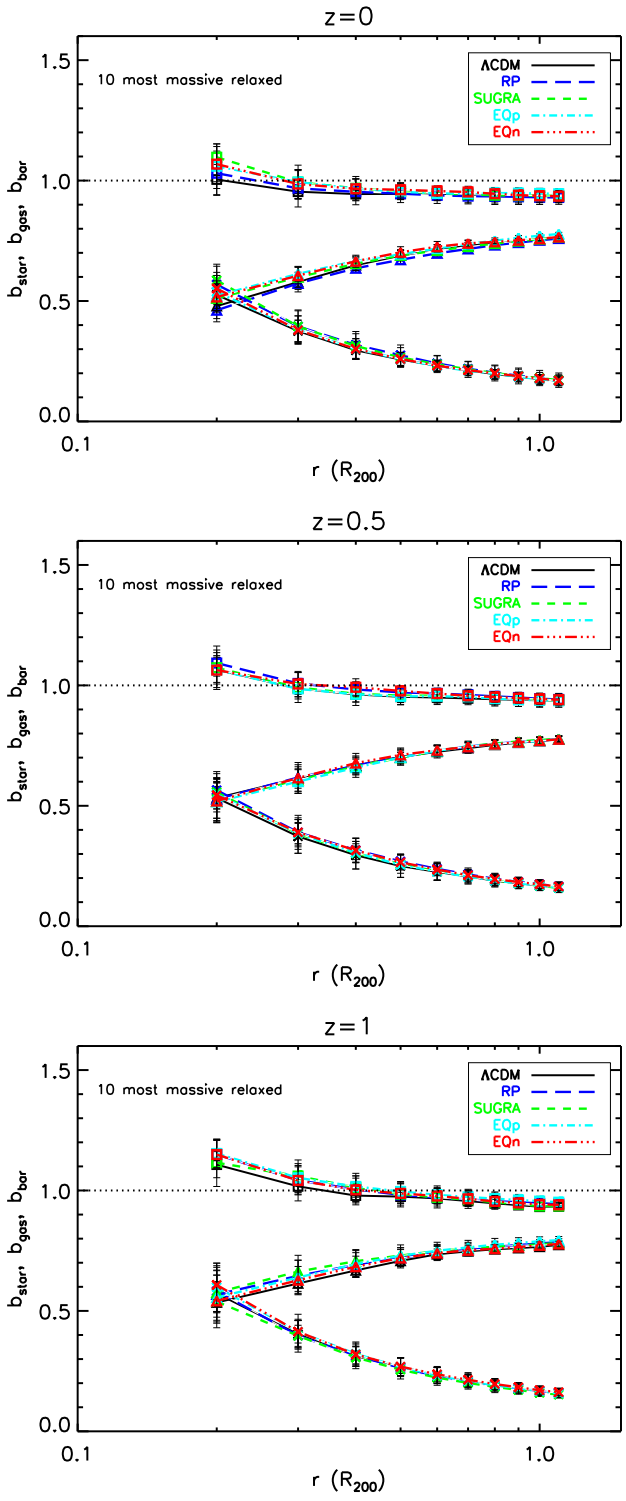


Figure 3.16: The evolution of stellar, gas and baryon depletion parameter with radius at $z = 0$ (top panel), $z = 0.5$ (middle panel), and $z = 1$ (bottom panel) for an object obtained by stacking the ten most massive relaxed clusters in the ΛCDM (black), RP (blue), SUGRA (green), EQp (cyan), and EQn (red) cosmologies. Crosses, triangles, and squares indicate $b_{star}$, $b_{gas}$, and $b_{bar}$ respectively. The depletion parameters are expressed in units of the cosmic baryon fraction $\Omega_{0b}/\Omega_{0m} = 0.164$. Error bars are r.m.s. of the mean distribution.

some differences can be seen. This fact means that, as a whole, evolved relaxed clusters contain the same amount of baryonic matter, independently of the underlying cosmological model, but that the matter can be redistributed inside them according to their formation history. This fact is confirmed by looking at $z = 0.5$ and in particular at $z = 1$, where the differences among the models are clear even in the outer regions, indicating a sort of self-regulating mechanism that leads to the same objects at $z = 0$ even if they can be very different at higher redshifts. Again, the same features appear both in the mean values of the whole sample and in more relaxed and massive objects, indicating that the latter are a fair representation of the clusters in a given cosmological model.

As a general rule for the radial profiles, it is confirmed the well known relative trend of the radial profile of gas and stars components, being the former increasing with radius and the latter decreasing, giving a total baryon fraction almost constant (but slightly decreasing) beyond $0.5R_{200}$. Then we note that the total baryon fraction at $z = 1$ is higher compared to $z = 0$, in particular in the inner regions of clusters. The effect is mainly due to a higher star fraction in the inner regions of clusters at $z = 1$. Another quite evident feature is that the radius at which the gas starts to dominate over the stars increases with increasing redshift. The explanation is that, as we have just seen, the gas fraction profile is almost independent of redshift, while the star fraction at a given radius increases with redshift, and so at higher redshift it remains the dominant baryonic component also at larger radii.

## 3.7 General properties: summary

In this chapter we have studied the general properties of the halos extracted from the *Padme* simulation set. From our analysis we draw the following conclusions.

- Mass function: at $z = 0$ the total mass function evaluated at $R_{200m}$ shows different behaviours in the different cosmologies, in particular in the normalization. The ΛCDM model tends to form more clusters of a given mass compared to the other cosmologies; SUGRA is the cosmology with the smallest abundance, while RP, EQp and EQn lie in between, with RP and EQp being the closest to ΛCDM. This fact directly reflects the redshift evolution of the equation of state parameter $w$ and of the growth factor, given the different assumed value of $\sigma_8$ in the various models. Actually, for extended quintessence models, a positive value of the coupling leads to a higher linear density contrast, and vice versa for a negative coupling. This would imply a higher mass function for models with negative coupling (*i.e.* EQn) than for models with positive coupling (*i.e.* EQp), keeping fixed all remaining parameters. In our case, this effect is somehow mitigated by the different $\sigma_8$ used. This trend is preserved also at $z = 0.5$ and $z = 1$. The differences among the models are more pronounced in the high-mass tail of the distribution. This is expected, because very massive objects form later and are representative of the different structure formation time scale of the considered cosmologies. We note here that our results are different from what has been found in the case of coupling with dark matter (Baldi & Pettorino, 2011), where there is an enhancement in the number counts of massive objects. Our mass functions for the ΛCDM model at $z = 0$ and $z = 0.5$ are in good agreement with observed data from Vikhlinin et al. (2009b) in the corresponding redshift bins.

- $L - T$ relation: we compare the $L - T$ relation of our simulated objects in the ΛCDM reference models with a collection of observed objects (Pratt et al., 2009). Despite the differences in the slope of the relation in the two cases (1.81 for our simulated

objects vs $2.53 \pm 0.16$ for their observed ones), we find that there is a good agreement in the high-temperature high-luminosity region where X-ray selected observed objects are found. The discrepancy in the low-temperature low-luminosity region is not worrying, because low-mass systems are globally more affected by physical mechanisms not yet fully understood and reproduced (*e.g.* Borgani et al., 2004), acting in the core. We also study the evolution with redshift of the $L - T$ relation for the ten most massive relaxed objects in each cosmology, both keeping and cutting the core. We find that cutting the core results in both a lower mean luminosity and lower mean emission-weighted temperature. In general, both the mean luminosity and temperature increase with decreasing redshift, independently of the cosmological model, because they trace the hierarchical growth of structures.

- X-ray observable functions: the relative behaviour observed in the mass functions is also qualitatively reproduced by the XLFs and XTFs evaluated in the $[0.5 - 2]$ keV band in the $[0.15 - 1]R_{500}$ region, with few exceptions. In particular, in the range of luminosity around $0.5 \times 10^{43}$ erg s$^{-1}$ RP tends to form 10% more clusters than ΛCDM. We also check the X-ray $M_{gas500}$ and $Y_{X500}$ functions as proxies for the mass function. We conclude that all the X-ray observable functions are more or less equivalent, with $T_{ew}$ and $M_{gas500}$ being slightly more stable than $L_X$ and $Y_{X500}$, in tracing the mass function and thus disentangle the growth of structures among different dark energy models. For each dark energy model we evaluate the volumes that a cluster survey must cover in order to be able to distinguish it from the concordance ΛCDM model, using the mass function, the XLF, and the XTF.

- Baryon fraction: the analysis of the $b_{star}$, $b_{gas}$, and $b_{bar}$ dependence on mass, redshift and distance from the cluster centre shows that there is no significant difference among the five cosmologies considered, if we limit ourselves to the values at $R_{200}$ and at $z = 0$. Therefore, at these conditions, $b_{bar}$ (and so the baryon fraction $f_{bar}$) can be safely used as a cosmological proxy to derive the value of other cosmological parameters. In addition, we do not find any clear positive trend of the total baryon fraction with mass, while we see a positive trend (of the order of 5%) of the gas fraction and a negative trend (of the order of 30%) of the star fraction going from low-mass to high-mass systems. Considering observations of real objects, in spite of finding the same trend for the gas and star fraction as we do, other authors (*e.g.* Giodini et al., 2009) claim that the total baryon fraction is increasing with increasing mass. Actually, for all the cosmological models here considered, we find a slight decrease in the total baryon fraction with increasing mass. Still, we have to recall that, despite the hydrodynamical treatments in the simulations is based on sophisticated physical models, we do not include AGN feedback in our simulations. It is known from literature (see *e.g.* Puchwein et al., 2008) that AGN feedback is mass dependent, in the sense that it globally affects more low-mass systems than high-mass systems. The net effect is the lowering of the total baryon fraction in low-mass objects while not affecting more massive clusters. Finally, we find a slight decrease (at most 5%) of the baryon fraction going from high to low redshift. A similar trend was already noted by Ettori et al. (2006) and a possible explanation is that at high redshift the radius at which the baryons accrete is smaller than at low redshift, and so a greater number of baryons can fall in the cluster potential well.

# Chapter 4

# *Padme* Simulation: $c - M$ relation

In this chapter we will present a comparison between dark matter only and hydrodynamical simulations in order to study the impact of baryon physics on the $c - M$ relation, also considering the possible consequences of the presence of a dynamical dark energy component. After introducing different methods to define the concentration in Section 4.1, along with a non-parametric definition in Section 4.2, we will compare our results for the ΛCDM model with other results from literature in Section 4.3. Then, for the different dark energy cosmologies, we will analyse the dark matter only runs in Section 4.4 and the hydrodynamical runs in Section 4.5. We will discuss the results in Section 4.6 and draw our conclusions in Section 4.7.

## 4.1 Fitting procedure

In this part of the work, we analyse both the dark matter only and the hydrodynamical runs of the *Padme* simulation set. As in the previous chapter, we consider all the halos that have $M_{200m} > 10^{14}$ $\mathrm{M}_\odot$ $h^{-1}$ but, since we want to extend the $c - M$ relation also to lower masses, we add the 200 objects with $M_{200m}$ closest to $7 \times 10^{13}$ $\mathrm{M}_\odot$ $h^{-1}$, $5 \times 10^{13}$ $\mathrm{M}_\odot$ $h^{-1}$, $3 \times 10^{13}$ $\mathrm{M}_\odot$ $h^{-1}$, and $10^{13}$ $\mathrm{M}_\odot$ $h^{-1}$. Starting from the centres of the halos, we construct radial profiles by binning the particles in radial bins.

For the concordance ΛCDM model, for each cluster at $z = 0$ in the dark matter only run, we perform a logarithmic fit, using Poissonian errors $(\ln 10 \times \sqrt{n_{dm}})^{-1}$ (where $n_{dm}$ is the number of dark matter particles in each radial bin, of the order of $10 - 10^3$ depending on the mass of the object), of the three-dimensional dark matter profile $\rho_{dm}(r)/\rho_c$ in the region $[0.1 - 1]R_{200}$ (where the value of $R_{200}$ is taken directly from the true mass profile) with a NFW profile (Navarro et al., 1996)

$$\frac{\rho_{dm}(r)}{\rho_c} = \frac{\delta_c}{(r/r_s)(1 + r/r_s)^2} \ , \tag{4.1}$$

where $\rho_c$ is the critical density, $r_s$ is the scale radius and $\delta_c$ is a characteristic density contrast. Then, instead of defining $c_{200} \equiv R_{200}/r_s$, we directly find the concentration parameter $c_{200}$ from the normalization of the NFW profile

$$\delta_c = \frac{200}{3} \frac{c_{200}^3}{\left[\ln(1 + c_{200}) - \frac{c_{200}}{1+c_{200}}\right]} \ . \tag{4.2}$$

We require the central density parameter $\delta_c$ to be greater than 100 and the scale radius $r_s$ to be within $[0.1 - 1]R_{200}$. We exclude the inner regions from the fit because we are limited in resolution inside a given radius. We indicate the dark matter concentration found in this way as $c_{200dm}$. We define the rms deviation $\sigma_{rms}$ as

$$\sigma^2_{rms} = \frac{1}{N_{bins}} \sum_{i=1}^{N_{bins}} [\log_{10}\rho_i - \log_{10}\rho_{NFW}]^2 \ , \tag{4.3}$$

where $N_{bins}$ is the number of radial bins over which the fit is performed.

In addition to the complete and relaxed samples discussed in Chapter 3, we create a sample of "super-relaxed" objects defined as the ones having both $x_{off}$ and $\sigma_{rms}$ lower than the median value extracted from the complete sample, namely 0.046 and 0.0358, respectively. We do this to check if strict restrictions on both the dynamical state and the shape of the profile of the objects can reduce the intrinsic scatter in the values of concentration. We stress that the definition of super-relaxed objects is dependent on the way we fit the profile. In the end, the complete sample, the relaxed sample and the super-relaxed sample at $z = 0$ are constituted by 1357, 923, and 411 objects, respectively.

We bin the objects in the complete sample in groups of 200, so that we have bins around $10^{13}$ $M_\odot$ $h^{-1}$, $3 \times 10^{13}$ $M_\odot$ $h^{-1}$, $5 \times 10^{13}$ $M_\odot$ $h^{-1}$, and $7 \times 10^{13}$ $M_\odot$ $h^{-1}$. For halos more massive than $10^{14}$ $M_\odot$ $h^{-1}$, we bin the objects starting from the low-mass ones, so that the most massive bin can contain less than 200 objects. For the relaxed and super-relaxed samples, we select the relaxed and super-relaxed objects inside each bin. Once we have $c_{200dm}$ for each object in each mass bin, since the distribution of $c_{200dm}$ is log-normal inside each bin, we evaluate the mean $M_{200}$ and the mean and rms deviation of $\log_{10}c_{200dm}$ in each bin, for all the three samples. In the following of the chapter, when we indicate the value of $c_{200dm}$ in a mass bin, we refer to 10 to the mean of $\log_{10}c_{200dm}$.

In Fig. 4.1 we plot $c_{200dm}$ for each object in the complete sample. We see that there is a large intrinsic dispersion in the values of the concentration inside each group of objects, which is marked with a different colour. For objects more massive than $10^{14}$ $M_\odot$ $h^{-1}$, the maximum value of $c_{200dm}$ clearly decreases with $M_{200}$. Only when we bin the objects and plot the mean value of $c_{200dm}$ in each mass bin we can see a general trend of concentration decreasing with increasing mass, even if the rms deviations are quite large.

In Fig. 4.2 we plot the $c_{200dm}$ in each mass bin for the complete, relaxed and super-relaxed samples, along with the number of objects in each bin. We note that, in all bins, more than 50% of the halos are relaxed and around 30% are super-relaxed. In each bin, the value of $c_{200dm}$ for the relaxed sample is higher than the one for the complete sample, and the value for the super-relaxed sample is even higher. In all three samples, $c_{200dm}$ is decreasing with increasing mass. In Fig. 4.2 we also show the scatter in $\log_{10}c_{200dm}$ in each bin for the complete, relaxed and super-relaxed samples. For the complete sample, the relative errors range from 30% to 40%, with a positive trend with mass. It means that inside each mass bin there are objects with different properties, in particular in the high-mass tail. For the relaxed sample, the relative errors reduce to 20% up to 30%, meaning that part of the scatter in the complete sample is due to objects in a particular dynamical state. If we move to the super-relaxed sample, we notice that the relative errors stay between 15% and 20%. On the one hand, that means that putting strong constraints on both the dynamical state and the shape of the profile of the halos allows us to halve the intrinsic scatter; on the other hand, even when considering the most relaxed and smooth objects in our sample we cannot reduce

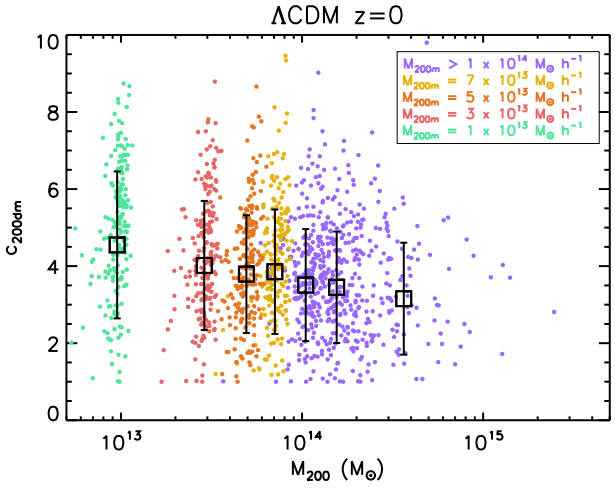


Figure 4.1: The values of $c_{200dm}$ for the complete sample of the ΛCDM model at $z = 0$. For each object, we plot $M_{200}$ and $c_{200dm}$. Different colours indicate different $M_{200m}$ ranges. The black squares indicate $c_{200dm}$ in each mass bin (see text for details). For each mass bin, we plot the mean $M_{200}$ and $c_{200dm}$ with rms deviation.

the intrinsic scatter below 15%. This fact reinforces the conclusions we have drawn from the complete sample.
As a check, for the complete sample of the ΛCDM model at $z = 0$ we also evaluate $c_{200dm}$ by fitting the NFW profile (4.1) in the range $[0.01 - 1]R_{200}$. We show the results for the values of $c_{200dm}$ and the relative error in $\log_{10} c_{200dm}$ in each mass bin in Fig 4.3. We see that, by fitting in the range $[0.01 - 1]R_{200}$, we obtain concentrations up to 10% higher than by fitting in the $[0.1 - 1]R_{200}$ range. Moreover, by fitting including the inner regions in the fit, the intrinsic scatter in concentration is lower by about 5%. These trends are almost independent of mass. Since we want to compare the dark matter only runs with the hydrodynamical ones, and in the hydrodynamical runs we do not completely resolve the baryonic physics on small scales, we will take a conservative approach and fit in the range $[0.1 - 1]R_{200}$. Still, it is important to know what happens if we consider also the inner regions, in particular if we want to compare our results with the ones in literature.

With the mean and rms deviation of $\log_{10} c_{200dm}$ in each bin at hand, we fit, for the complete, relaxed and super-relaxed samples, the binned $c - M$ relation using

$$\log_{10} c_{200} = \log_{10} A + B \log_{10} \left( \frac{M_{200}}{10^{14} \mathrm{M}_{\odot}} \right) , \tag{4.4}$$

where $\log_{10} c_{200}$ and $M_{200}$ are the mean values in each bin. For the error on the mean of $\log_{10} c_{200dm}$ in each bin, $\sigma_{\bar{c}}$, we use the rms deviation of $\log_{10} c_{200dm}$ divided by the square root of the number of objects in the bin. For each fit we also define the chi-squared as

$$\chi^2 = \sum_{i=1}^{N_{bins}} \left( \frac{\log_{10} c_{200_i} - \log_{10} c_{200_{fit}}}{\sigma_{\bar{c}_i}} \right)^2 , \tag{4.5}$$

where $N_{bins}$ is the number of mass bins over which the fit is performed and $\sigma_{\bar{c}}$ is the error defined above. Finally, we evaluate the reduced chi-squared $\tilde{\chi}^2$, *i.e.* the chi-squared divided

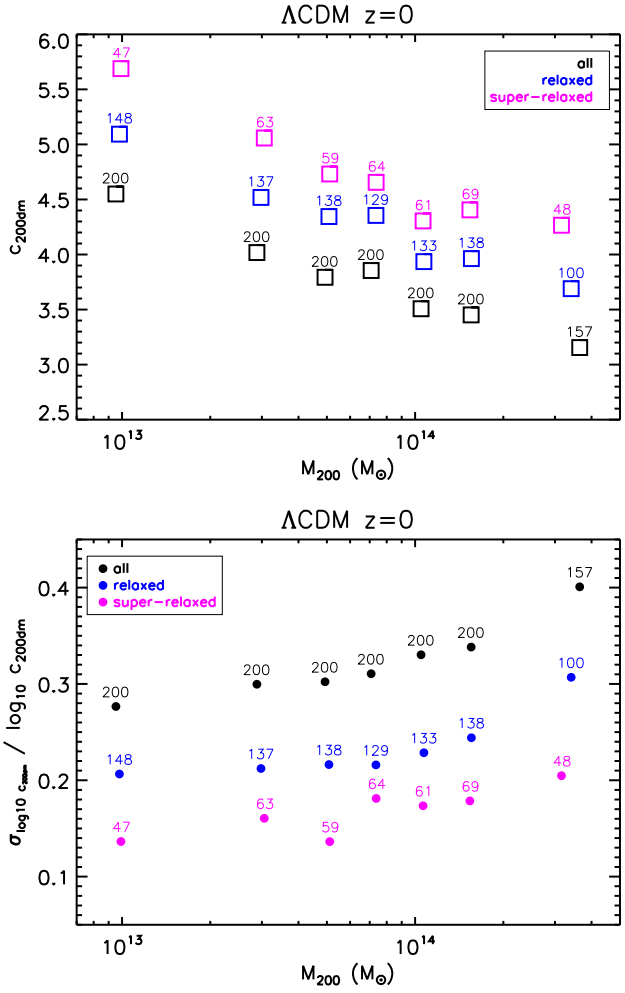


Figure 4.2: (Top panel) The values of $c_{200dm}$ in each mass bin for the complete (black), relaxed (blue) and super-relaxed (pink) samples of the ΛCDM model at $z = 0$. For each mass bin, we plot the mean $M_{200}$, $c_{200dm}$ and the number of objects in the bin. (Bottom panel) Relative error in $\log_{10} c_{200dm}$ in each mass bin for the complete (black), relaxed (blue) and super-relaxed (pink) samples of the ΛCDM model at $z = 0$. For each mass bin, we plot the mean $M_{200}$, the relative error $\sigma_{\log_{10} c_{200dm}} / \log_{10} c_{200dm}$ and the number of objects in the bin.

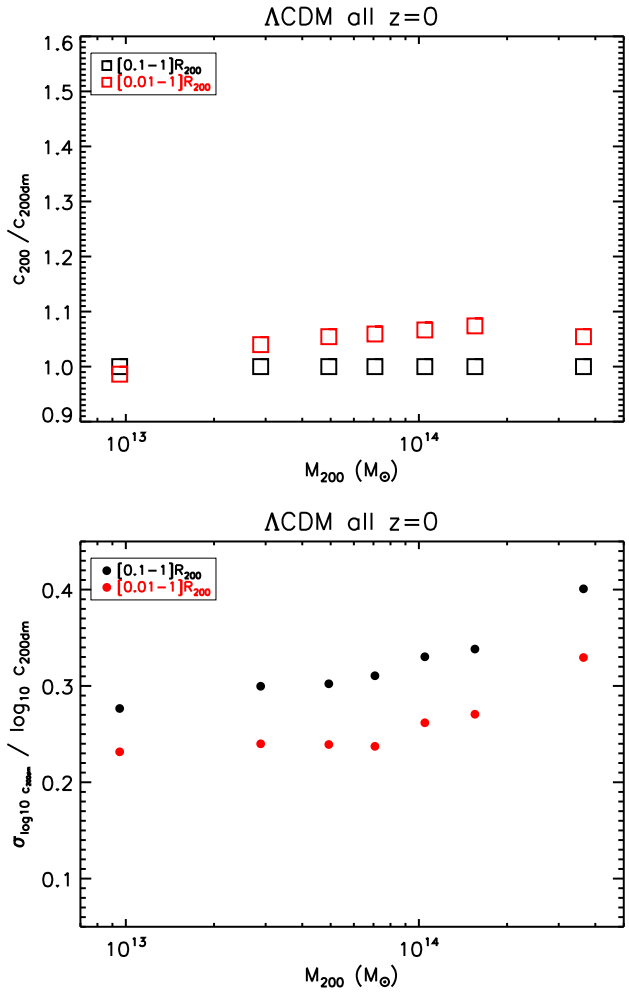


Figure 4.3: (Top panel) Ratio in each mass bin between $c_{200dm}$ evaluated from equation (4.2) by fitting equation (4.1) in the range $[0.1-1]R_{200}$ (black squares) and $c_{200dm,fit}$ evaluated by fitting in the range $[0.01-1]R_{200}$ (red points) and $c_{200dm}$ evaluated by fitting in the range $[0.1-1]R_{200}$, for the complete sample of the ΛCDM model at $z = 0$. (Bottom panel) Relative error in $\log_{10}c_{200dm}$ in each mass bin for the $[0.1-1]R_{200}$ fit (black) and the $[0.01-1]R_{200}$ fit (red) for the complete sample of the ΛCDM model at $z = 0$.

Table 4.1: Best-fit parameters, standard errors and reduced chi-squared $\tilde{\chi}^2$ of the $c - M$ relation (4.4) for dark matter only density profile fit in the region $[0.1 - 1]R_{200}$ for the complete, relaxed and super-relaxed samples of the ΛCDM model at $z = 0$.

| Model | $\sigma_8$ | $A$ | $\sigma_A$ | $B$ | $\sigma_B$ | $\tilde{\chi}^2$ |
|---|---|---|---|---|---|---|
| ΛCDM | 0.776 | dm | | | | |
| all | | 3.59 | 0.05 | −0.099 | 0.011 | 0.48 |
| relaxed | | 4.09 | 0.05 | −0.092 | 0.011 | 0.66 |
| super-relaxed | | 4.52 | 0.06 | −0.091 | 0.013 | 0.76 |

Table 4.2: Best-fit parameters and standard errors of the $c - M$ relation (4.4) for dark matter only density profile fit in the region $[0.1 - 1]R_{200}$, considering only objects with $M_{200m} > 10^{14}$ M$_\odot$ $h^{-1}$, for the complete, relaxed and super-relaxed samples of the ΛCDM model at $z = 0$.

| Model | $\sigma_8$ | $A$ | $\sigma_A$ | $B$ | $\sigma_B$ |
|---|---|---|---|---|---|
| ΛCDM | 0.776 | dm | | | |
| all | | 3.55 | 0.09 | −0.087 | 0.038 |
| relaxed | | 3.99 | 0.10 | −0.055 | 0.042 |
| super-relaxed | | 4.35 | 0.13 | −0.010 | 0.049 |

by the number of degrees of freedom, which is given by $N_{bins}$ minus the number of free parameters of the fit. We list the best fit values $A$ and $B$ for each sample, along with standard errors and reduced chi-squared, in Table 4.1. We see that, compared to the complete sample, the normalization $A$ increases by about 15% for the relaxed sample and by about 25% for the super-relaxed sample, while the slope $B$ does not change significantly, even if excluding unrelaxed objects results in a shallower slope. The values of the reduced chi-squared indicate that equation (4.4) is a good parametrization of the $c - M$ relation in logarithmic scale.

In order to understand the impact of low-mass object on the $c - M$ relation, we check how the best-fit values of the $c - M$ relation from equation (4.4) changes if we do not include the less massive objects. We report the results we obtain by considering only objects with $M_{200m} > 10^{14}$ M$_\odot$ $h^{-1}$ in Table 4.2. For all three samples, we find a flatter relation than when including also low-mass objects, with high standard errors on the slope. The normalizations are lower of few percentage points, while the relative errors are a factor of two higher compared to the case where low-mass objects are also considered. Moreover, in this case the slope is very sensible to the dynamical state of the objects included in the sample. Thus we conclude that the inclusion of low-mass objects is necessary to find a significant correlation between the concentration and the mass of the halos. We do not quote the reduced chi-squared in this case because just 3 mass bins are considered with 2 parameters to be fitted.

To compare our results with the ones found in literature, for the dark matter only profiles of the concordance ΛCDM model we also perform a logarithmic fit of equation (4.1) without using Poissonian errors. In this case we evaluate $c_{200}$ both from equation (4.2) and by directly defining $c_{200} \equiv R_{200}/r_s$ (using $R_{200}$ from the true mass profile), and indicate the two values as $c_{200dm,fit}$ and $c_{200dm,rec}$, respectively.

Moreover, in order to check the robustness of our fit, we perform a logarithmic fit, using Poissonian errors, of the dark matter profile times $r^2$, and a logarithmic fit, using Poissonian errors, of the dark matter profile times $r^3$.

Finally, we perform a logarithmic one-parameter fit, using Poissonian errors, of equation (4.1) re-expressed as

$$\frac{\rho_{dm}(r)}{\rho_c} = \frac{200}{3} \frac{c_{200}^3}{\left[\ln(1+c_{200}) - \frac{c_{200}}{1+c_{200}}\right]} \frac{1}{\left[\frac{c_{200}r}{R_{200}}\right]\left[1+\left(\frac{c_{200}r}{R_{200}}\right)\right]^2} , \tag{4.6}$$

where the only free parameter of the fit is directly $c_{200}$, since $R_{200}$ is the one taken from the true mass profile.
Only at comparison, we also evaluate the halos concentration following Prada et al. (2011), *i.e.* by solving

$$\frac{V_{max}}{V_{200}} = \left(\frac{0.216\ c}{f(c)}\right)^{1/2} , \tag{4.7}$$

where

$$V_{max} = \max\left[\frac{GM(<r)}{r}\right]^{1/2} , \tag{4.8}$$

$$V_{200} = \left(\frac{GM_{200}}{R_{200}}\right)^{1/2} , \tag{4.9}$$

and, for a NFW profile, $f(c)$ is given by

$$f(c) = \ln(1+c) - \frac{c}{1+c} , \tag{4.10}$$

We find that the best values $[\delta_c,\ r_s]$, and therefore $c_{200}$ from equation (4.2), found by fitting the dark matter profile times $r^2$ and the dark matter profile times $r^3$ are equal to the ones found from equation (4.1) with Poissonian errors, while the ones from equation (4.1) without Poissonian errors, from equation (4.6), and from equation (4.7) are different. We show these differences for the complete, relaxed, and super-relaxed samples in Fig. 4.4. For the complete sample, we see from Fig. 4.4 that the unweighted fit gives values of $c_{200dm}$ slightly higher compared to the Poisson weighted fits, with $c_{200dm,rec}$ always higher than $c_{200dm,fit}$. The values of $c_{200dm}$ found from the one-parameter fit of equation (4.6) are compatible with the ones found from equation (4.1) with Poissonian errors. All these models are compatible within few percentage points, while the method of Prada et al. (2011) gives systematically higher values, with a positive trend with mass. In the most massive bin, the difference between the concentrations is more than 20%. For the relaxed sample, the situation is similar, but the differences among the different fits are somewhat smaller. Even for the method based on equation (4.7), which is the one that gives very different results, the difference is at most around 10%. For the super-relaxed sample, the differences among the different fits almost disappear, with the exception of the method of Prada et al. (2011), which however now shows differences below 5% and, in the lowest mass bin, recovers values of the concentration even lower than the other methods.

In Table 4.3 we show the best-fit parameters, the standard errors and the reduced chi-squared of the $c-M$ relation, equation (4.4), for the different fits discussed above. As expected, for all the three samples, the differences in the normalization and slope are limited to a few

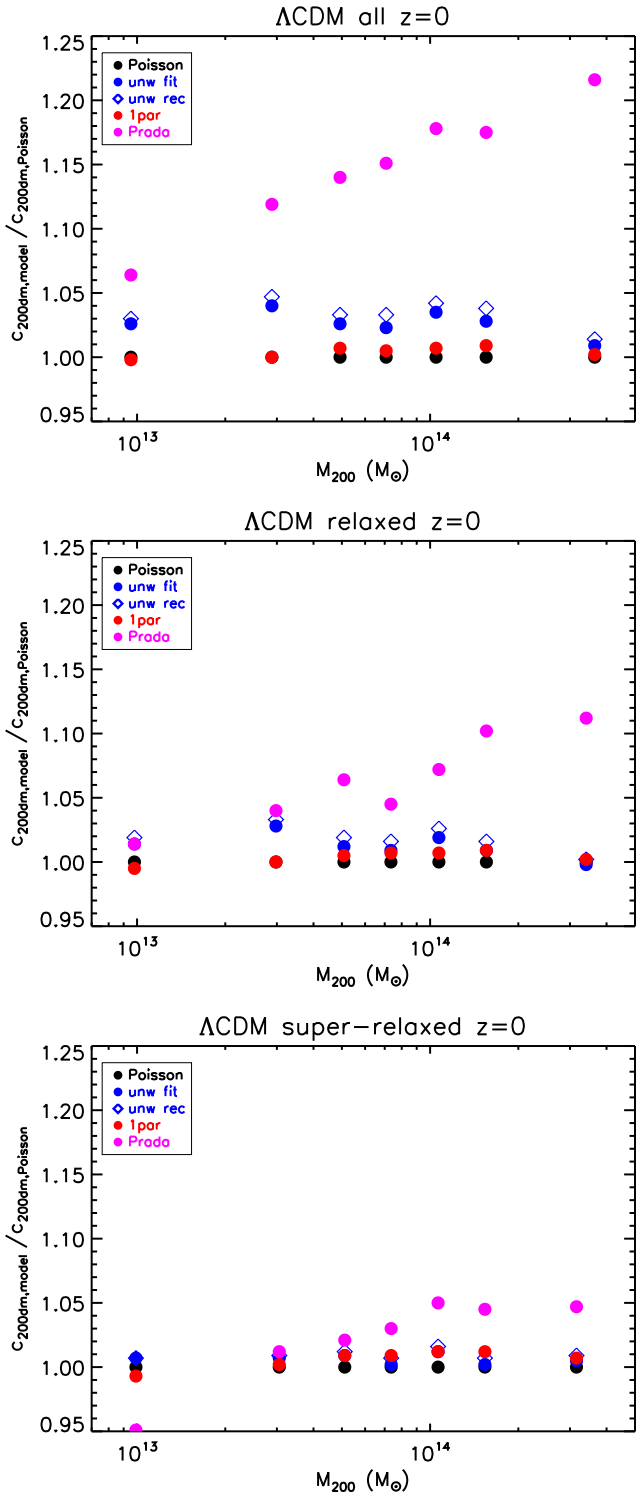


Figure 4.4: (Top panel) Ratio in each mass bin between $c_{200dm}$ (black points), $c_{200dm,fit}$ (blue points), $c_{200dm,rec}$ (blue diamonds), $c_{200dm}$ found by fitting equation (4.6) (red points), and $c$ recovered from equation (4.7) (pink points) and $c_{200dm}$ evaluated from equation (4.2) by fitting equation (4.1) using Poissonian errors, for the complete sample of the ΛCDM model at $z = 0$. (Middle panel) The same as in the top panel, but for the relaxed sample. (Bottom panel) The same as in the top panel, but for the super-relaxed sample.

Table 4.3: Best-fit parameters, standard errors and reduced chi-squared $\tilde{\chi}^2$ of the $c-M$ relation (4.4) for the different fits of the dark matter only density profile for the complete, relaxed and super-relaxed samples of the ΛCDM model at $z = 0$.

| Model | $\sigma_8$ | $A$ | $\sigma_A$ | $B$ | $\sigma_B$ | $\tilde{\chi}^2$ |
|---|---|---|---|---|---|---|
| ΛCDM | 0.776 | dm (all) | | | | |
| Poisson | | 3.59 | 0.05 | −0.099 | 0.011 | 0.48 |
| $c_{200dm,fit}$ | | 3.69 | 0.04 | −0.102 | 0.010 | 0.49 |
| $c_{200dm,rec}$ | | 3.71 | 0.04 | −0.101 | 0.010 | 0.57 |
| one-parameter | | 3.61 | 0.05 | −0.096 | 0.011 | 0.50 |
| Prada | | 4.18 | 0.04 | −0.063 | 0.008 | 0.67 |
| ΛCDM | 0.776 | dm (relaxed) | | | | |
| Poisson | | 4.09 | 0.05 | −0.092 | 0.011 | 0.66 |
| $c_{200dm,fit}$ | | 4.14 | 0.05 | −0.096 | 0.010 | 0.53 |
| $c_{200dm,rec}$ | | 4.17 | 0.05 | −0.095 | 0.010 | 0.55 |
| one-parameter | | 4.12 | 0.05 | −0.088 | 0.011 | 0.74 |
| Prada | | 4.40 | 0.04 | −0.065 | 0.008 | 0.90 |
| ΛCDM | 0.776 | dm (super-relaxed) | | | | |
| Poisson | | 4.52 | 0.06 | −0.091 | 0.013 | 0.76 |
| $c_{200dm,fit}$ | | 4.55 | 0.06 | −0.092 | 0.013 | 0.67 |
| $c_{200dm,rec}$ | | 4.56 | 0.06 | −0.091 | 0.013 | 0.66 |
| one-parameter | | 4.56 | 0.06 | −0.086 | 0.012 | 0.63 |
| Prada | | 4.69 | 0.06 | −0.060 | 0.010 | 0.45 |

precent, with the exception of the method discussed in Prada et al. (2011). For this method we find a flatter relation, due to the fact that it predicts higher concentrations for high-mass objects compared to the usual fit of the NFW profile (4.1). Moreover, also the normalization is higher (more than 15% for the complete sample, more than 5% for the relaxed sample, and less than 5% for the super-relaxed one), given that the concentration found from equation (4.7) is in general higher than the one found in the usual way. As already shown, the effect is stronger for the complete sample than for the relaxed and super-relaxed ones. The values of the reduced chi-squared indicate that equation (4.4) is a good parametrization of the $c - M$ relation also for these different definitions of the concentration.

Before moving to the hydrodynamical simulation, we sum up here our findings for the dark matter only run of the reference ΛCDM model. The intrinsic dispersion in the logarithmic values of $c_{200dm}$ for objects of similar mass is reduced by a factor of two if we limit our analysis to objects that are both relaxed and with a clear NFW-like shape of the dark matter profile. Still, at best, the intrinsic scatter is of the order of 15%. The more relaxed the objects in the sample, the higher the normalization $A$ of the $c - M$ relation equation (4.4), while the slope $B$ is almost independent of the dynamical state of the halos. This is no longer true if we focus our analysis to objects with $M_{200m} > 10^{14}$ $\mathrm{M}_\odot$ $h^{-1}$, for which the slope is shallower for the relaxed sample and almost flat for the super-relaxed one. If we limit ourselves in fitting the dark matter profile with a NFW profile, we almost recover the same values of $c_{200dm}$, $A$, and $B$, independently of the way we treat the errors on the fit and on the number of free parameters that we fit. Things do change if we use the method introduced in Prada et al. (2011), which systematically overestimates the concentration compared to the others, in particular for high-mass objects. This results in both higher values of $A$ and $B$ for this method. With this in mind, in the following of this chapter, in particular when we study the effect of dark energy on the $c - M$ relation, we will always consider $c_{200dm}$ recovered from equation (4.2) from the fit of equation (4.1) with Poissonian errors, and distinguish only

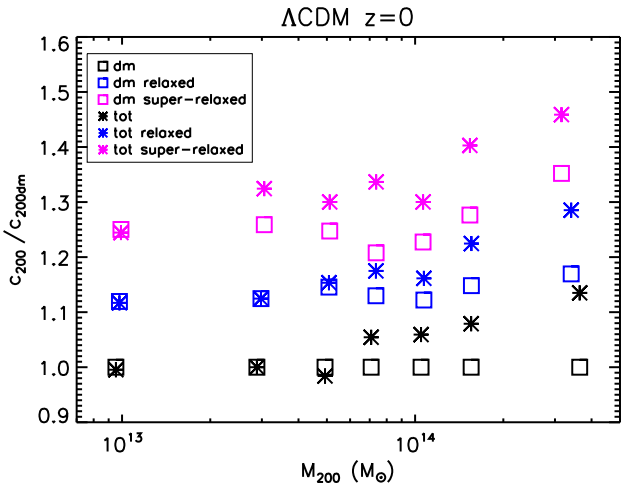


Figure 4.5: Ratio in each mass bin between $c_{200dm}$ (squares) and $c_{200tot}$ (stars) for the complete (black), relaxed (blue) and super-relaxed (pink) samples and $c_{200dm}$ for the complete sample of the ΛCDM model at $z = 0$.

between the complete and the relaxed sample, whose definition is independent of the way we find the concentration.

For the hydrodynamical run, we fit the total three-dimensional density profile $\rho_{tot} = \rho_{dm} + \rho_{gas} + \rho_{star}$ in the range $[0.1 - 1]R_{200}$ with equation (4.1), using Poissonian errors $(\ln 10 \times \sqrt{n_i})^{-1}$ for each component (where $n_i$ is the number of particles of the $i$-th species) and summing them in quadrature. We indicate the total matter concentration found from equation (4.2) with $c_{200tot}$. We show the differences between $c_{200dm}$ and $c_{200tot}$ for the complete, relaxed and super-relaxed samples in Fig. 4.5. We clearly see that, in all three samples, starting from objects with $M_{200m} > 10^{14}$ M$_\odot$ $h^{-1}$ the concentration in the hydrodynamical run is higher than in the dark matter only case, and the effect becomes more relevant at higher masses. This effect is less pronounced in objects with $M_{200m} < 10^{14}$ M$_\odot$ $h^{-1}$. Thus, the inclusion of baryons appears to affect more massive galaxy clusters than small groups. In order to check this fact, we evaluate the relative distribution of baryons and stars inside $R_{200}$ and in the range $[0.1 - 0.3]R_{200}$, that means the innermost part of the range in which we fit the NFW profile. We show the results in Fig. 4.6. We see that, while the total baryon fraction at $R_{200}$ is almost constant with mass, if we limit to the range $[0.1 - 0.3]R_{200}$ the baryon contribution to the total mass becomes more important for more massive objects. The same happens for the stars, which are known to concentrate in the internal regions of halos. Thus, in this simulation, the relative contribution of baryons and stars in the inner regions is more relevant in massive galaxy clusters than in small groups, and this fact leads to an increase in the concentration of massive objects when including baryonic physics in the simulations.

Then, we fit the $c - M$ relation (4.4) as in the dark matter only case. We list the best-fit parameters, standard errors and reduced chi-squared of the $c - M$ relation for the complete, relaxed, and super-relaxed samples in Table 4.4. For all samples, the normalization $A$ is from 5% to 10% higher compared to the dark matter only case, while the slope is shallower by about 30%. This is expected because, as we have already seen, in the hydrodynamical runs high-mass objects are more concentrated than objects of the same mass in the dark matter only simulations. For the hydrodynamical runs the values of the reduced chi-squared are quite high. This fact seems to indicate that baryons introduce some dependence that equation (4.4),

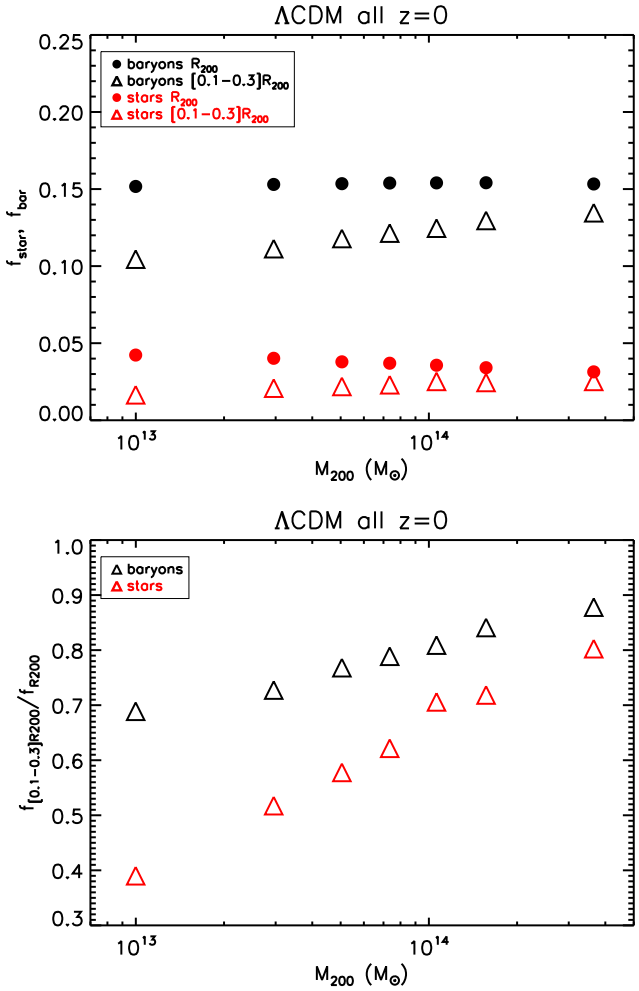


Figure 4.6: (Top panel) Star fraction $f_{star}$ (red) and total baryon fraction $f_{bar}$ (black) at $R_{200}$ (points) and in the $[0.1 - 0.3]R_{200}$ range (triangles) in each mass bin for the complete sample of the ΛCDM model at $z = 0$. (Bottom panel) Ratio in each mass bin between $f_{star}$ in the range $[0.1 - 0.3]R_{200}$ and $f_{star}$ at $R_{200}$ (red triangles) and between $f_{bar}$ in the range $[0.1 - 0.3]R_{200}$ and $f_{bar}$ at $R_{200}$ (black triangles) for the complete sample of the ΛCDM model at $z = 0$.

even though it remains a good parametrization, is not able to completely characterize.
Finally, in order to study the evolution with redshift of the $c - M$ relation, which is of fundamental importance if we want to distinguish among different cosmological models, we also consider objects at $z = 0.5$ and $z = 1$. We show the differences between $c_{200dm}$ and $c_{200tot}$ for the complete and relaxed sample of the ΛCDM model at $z = 1$ in Fig. 4.7. Even if the trend with mass is less clear than at $z = 0$, still we can see that, already at $z = 1$, $c_{200tot}$ is greater than $c_{200dm}$ in both samples.
When we consider also objects at $z = 0.5$ and $z = 1$, we fit a generalized form of the $c - M$ relation (4.4) with an explicit redshift dependence, namely

$$\log_{10} c_{200} = \log_{10} A + B \log_{10}\left(\frac{M_{200}}{10^{14}\mathrm{M}_{\odot}}\right) + C \log_{10}(1+z) \ . \tag{4.11}$$

We can perform this fit in two ways. Either we keep the best-fit values $A_0$ and $B_0$ found

Table 4.4: Best-fit parameters, standard errors and reduced chi-squared $\tilde{\chi}^2$ of the $c-M$ relation (4.4) for dark matter only and total density profile fit in the region $[0.1-1]R_{200}$ for the complete, relaxed and super-relaxed samples of the ΛCDM model at $z=0$.

| Model | $\sigma_8$ | $A$ | $\sigma_A$ | $B$ | $\sigma_B$ | $\tilde{\chi}^2$ |
|---|---|---|---|---|---|---|
| ΛCDM | 0.776 | all | | | | |
| dm | | 3.59 | 0.05 | −0.099 | 0.011 | 0.48 |
| tot | | 3.81 | 0.05 | −0.061 | 0.011 | 1.69 |
| ΛCDM | 0.776 | relaxed | | | | |
| dm | | 4.09 | 0.05 | −0.092 | 0.011 | 0.66 |
| tot | | 4.29 | 0.05 | −0.064 | 0.011 | 1.54 |
| ΛCDM | 0.776 | super-relaxed | | | | |
| dm | | 4.52 | 0.06 | −0.091 | 0.013 | 0.76 |
| tot | | 4.89 | 0.06 | −0.062 | 0.011 | 1.34 |

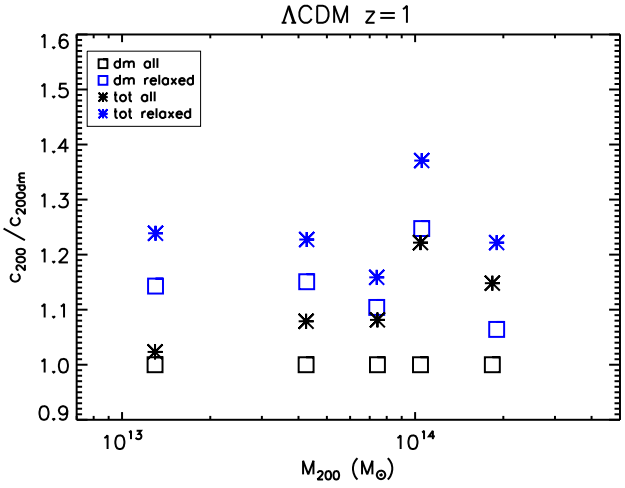


Figure 4.7: Ratio in each mass bin between $c_{200dm}$ (squares) and $c_{200tot}$ (stars) for the complete (black) and relaxed (blue) samples and $c_{200dm}$ for the complete sample of the ΛCDM model at $z=1$.

at $z=0$ fixed and fit only $C$ in equation (4.11), or we perform a three-parameter fit by keeping $A$, $B$ and $C$ free. We report the results of the different fits both for the complete and relaxed samples of the dark matter only and hydrodynamical simulations in Table 4.5. The first thing that we note is the fact that, in all cases, the redshift dependence is negative, meaning that objects of a given mass have lower concentration at higher redshift. If we leave the normalization and the slope free, we see that $A$ changes at most of few percentage points, while $B$ can vary significantly. The redshift dependence seems to be insensitive to both the way in which the fit is performed and the dynamical state of the halos, while it is different for dark matter only and total concentration, being steeper in the former case and shallower in the latter. In general, the reduced chi-squared of the fit of equation (4.11) are rather high, in particular for the hydrodynamical runs. This can be an indication that the redshift dependence we are considering is somehow too simple to fully reproduce the redshift evolution of the $c-M$ relation, and that the presence of baryons make this evolution more complex. In the following sections, we will constrain the normalization and slope at $z=0$, and then study the redshift evolution keeping $A$ and $B$ fixed.

Table 4.5: Best-fit parameters, standard errors and reduced chi-squared $\tilde{\chi}^2$ of the $c - M$ relation (4.11) for dark matter only and total density profile fit in the region $[0.1 - 1]R_{200}$ for the complete and relaxed samples of the ΛCDM model at $z = 0$, $z = 0.5$ and $z = 1$ both fixing $A$ and $B$ at the best-fit values at $z = 0$ and keeping all the parameters free.

| Model | $\sigma_8$ | $A$ | $\sigma_A$ | $B$ | $\sigma_B$ | $C$ | $\sigma_C$ | $\tilde{\chi}^2$ |
|---|---|---|---|---|---|---|---|---|
| ΛCDM | 0.776 | dm (all) | | | | | | |
| fixed | | 3.59 | — | −0.099 | — | −0.33 | 0.02 | 1.68 |
| free | | 3.63 | 0.04 | −0.077 | 0.008 | −0.32 | 0.03 | 1.41 |
| ΛCDM | 0.776 | dm (relaxed) | | | | | | |
| fixed | | 4.09 | — | −0.092 | — | −0.31 | 0.02 | 1.22 |
| free | | 4.13 | 0.05 | −0.080 | 0.008 | −0.31 | 0.03 | 1.24 |
| ΛCDM | 0.776 | tot (all) | | | | | | |
| fixed | | 3.81 | — | −0.061 | — | −0.26 | 0.02 | 2.40 |
| free | | 3.81 | 0.04 | −0.046 | 0.007 | −0.25 | 0.03 | 2.40 |
| ΛCDM | 0.776 | tot (relaxed) | | | | | | |
| fixed | | 4.29 | — | −0.064 | — | −0.26 | 0.02 | 1.97 |
| free | | 4.27 | 0.05 | −0.071 | 0.007 | −0.26 | 0.03 | 2.15 |

## 4.2 Model-independent concentration

All the fits we used in the previous sections are based on some assumptions that we made on the shape of the density profile. In principle, it should be useful to have a model-independent proxy for the concentration found from equation (4.2). Given the usual definition of the concentration, a natural quantity could be the ratio between two physical radii, characterized by a given overdensity. As already pointed out in Duffy et al. (2010), a good choice should be $R_{2500}/R_{500}$ which are commonly used in X-ray observations. For each object, we evaluate the ratio $R_{2500}/R_{500}$ taking $R_{2500}$ and $R_{500}$ directly from the true mass profile, without assumptions on the density profile. We bin the objects in mass as in the previous sections. The results for the complete, relaxed and super-relaxed samples, are shown in Fig. 4.8. The first thing that we note is that, for a given sample, the variation of $c_{200}$ is more than 30% while the variation of $R_{2500}/R_{500}$ is less than 10%. That means that the ratio between $R_{2500}$ and $R_{500}$ is less dependent on the mass of the halo when compared to $c_{200}$. The other thing we note is that objects with higher concentration, *i.e.* with higher $R_{200}/r_s$, also have higher $R_{2500}/R_{500}$. This result confirms the ones in Duffy et al. (2008), where a weak positive trend of $R_{500}/R_{2500}$ with $M_{500}$ was found. Finally, there is a clear dichotomy between the dark matter only and the total profile fits. At a given concentration, when including baryons, the ratio $R_{2500}/R_{500}$ is more than 5% higher with compared to the dark matter only case. Moreover, in the dark matter only case, the relation between $R_{2500}/R_{500}$ and $c_{200}$ closely follows the one predicted from equation (2.28), indicating that the halos are well described by a NFW profile. The different behaviour of the halos extracted from the hydrodynamical run suggests that, when we consider the total (dark matter plus baryons) density profile, the NFW profile is no longer a good approximation to the real profile.

## 4.3 Comparison with other works

In this section, we compare with previous works our results on the dark matter concentration obtained by fitting equation (4.1) in the range $[0.1-1]R_{200}$. We use objects at $z = 0$, $z = 0.5$, and $z = 1$ from the dark matter only simulations of the concordance ΛCDM model normalized with WMAP3 data. We recall that, by fitting the $c - M$ relation (4.11), we find that more

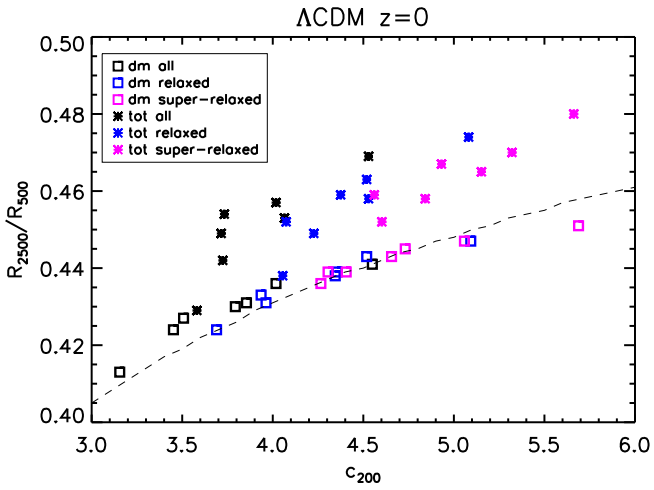


Figure 4.8: Comparison between $c_{200dm}$ (squares) and $c_{200tot}$ (stars) and $R_{500}/R_{2500}$ for the complete (black), relaxed (blue) and super-relaxed (pink) samples of the ΛCDM model at $z = 0$. The black dashed-line represents the prediction for a NFW profile.

Table 4.6: Comparison with other works. See text for details.

| Reference | $h$ | $\Omega_m$ | $\sigma_8$ | dm (all) | | | dm (relaxed) | | |
|---|---|---|---|---|---|---|---|---|---|
| | | | | $A$ | $B$ | $C$ | $A$ | $B$ | $C$ |
| This work (fixed $A$ and $B$) | 0.704 | 0.268 | 0.776 | 3.59 | −0.099 | −0.33 | 4.09 | −0.092 | −0.31 |
| This work (free $A$ and $B$) | 0.704 | 0.268 | 0.776 | 3.63 | −0.077 | −0.32 | 4.13 | −0.080 | −0.31 |
| Macciò et al. (2008) | 0.71 | 0.268 | 0.90 | 4.55 | −0.119 | — | 5.31 | −0.104 | — |
| | 0.73 | 0.238 | 0.75 | 3.60 | −0.088 | — | 4.13 | −0.083 | — |
| | 0.72 | 0.258 | 0.796 | 3.84 | −0.110 | — | 4.46 | −0.098 | — |
| Neto et al. (2007) | 0.73 | 0.25 | 0.9 | 4.85 | −0.11 | — | 5.45 | −0.10 | — |
| Duffy et al. (2008) | 0.742 | 0.258 | 0.796 | 4.06 | −0.097 | — | 4.81 | −0.092 | — |
| | 0.742 | 0.258 | 0.796 | 4.23 | −0.084 | −0.47 | 4.85 | −0.091 | −0.44 |
| Prada et al. (2011) | 0.70 | 0.27 | 0.82 | 5.31 | −0.074 | — | 5.55 | −0.08 | — |

massive objects are less concentrated than less massive ones and that objects at high redshift are less concentrated than objects at $z = 0$. Moreover, relaxed objects are more concentrated compared to the complete sample. All these findings qualitatively confirm what can be found in literature. For the sake of comparison with literature, some numbers are summarized in Table 4.6, where we have adjusted the quoted normalization $A$ to our pivot mass $10^{14}\mathrm{M}_\odot$ using the corresponding quoted slope $B$.

Macciò et al. (2008) make a comparison of the $c - M$ relation for all and relaxed objects in different ΛCDM cosmologies, namely the ones obtained using the parameters coming from WMAP1, WMAP3 and WMAP5. They fit the dark matter profile with a NFW profile. They span the mass range $10^{10}\ \mathrm{M}_\odot\ h^{-1} \lesssim M \lesssim 10^{15}\ \mathrm{M}_\odot\ h^{-1}$ and bin the objects in mass bins of 0.4 dex width. WMAP3 and WMAP5 have a lower matter density $\Omega_m$ and a lower power-spectrum normalization $\sigma_8$ than WMAP1. This means that halos of a given mass form later, and thus should be less concentrated. And indeed this is what they find, as it can be seen from Table 4.6. The higher $\sigma_8$ and $\Omega_m$, the higher the normalization and the steeper the slope of the $c - M$ relation. With respect to their results for the WMAP3 cosmology Macciò et al. (2008), we find the same values of the normalization both for the complete and relaxed samples, with a slightly steeper slope. We show this excellent agreement in Fig. 4.9.

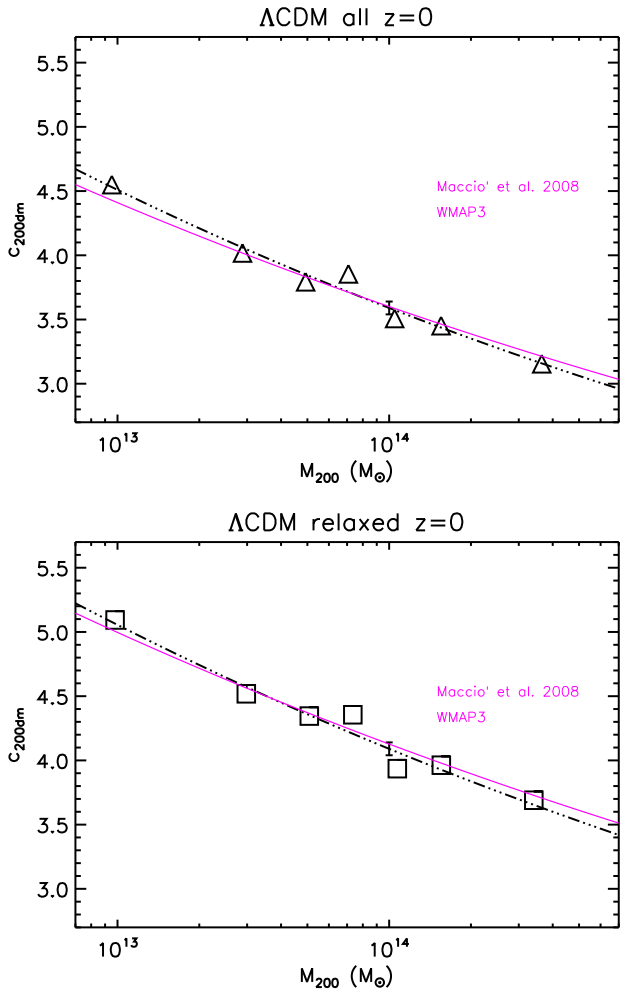


Figure 4.9: (Top panel) $c_{200dm}$ in each mass bin for the complete sample of the ΛCDM cosmology at $z = 0$. The black dotted-dashed line is our best-fit of $c - M$ relation (4.4) and the vertical bar is the error on the normalization as listed in Table 4.6. The pink solid line is relation of Macciò et al. (2008) for the WMAP3 cosmology. (Bottom panel) The same as in the top panel, but for the relaxed sample.

Neto et al. (2007) make a comparison, using halos extracted from the Millennium Simulation (MS) (Springel et al., 2005), between the complete sample and relaxed objects only. They fit the dark matter profile with a NFW profile in the $[0.05 - 1]R_{vir}$ range, without Poisson weighting. They span the mass range $10^{12}$ $M_\odot$ $h^{-1} \lesssim M \lesssim 10^{15}$ $M_\odot$ $h^{-1}$ and bin the objects in mass. They find that relaxed objects have more than 10% higher normalization compared to the whole sample, while the slope is 10% shallower. We find the same trend, but there is a discrepancy in the absolute numbers, both in the complete and relaxed samples. Indeed, they find normalizations that are more than 30% higher than ours, which can be explained with the higher $\sigma_8$, and a 10% steeper slopes.

Duffy et al. (2008) make a comparison with Neto et al. (2007) using WMAP5 (CMB only) data. They fit the dark matter profile with both a NFW and an Einasto profile in the $[0.05 - 1]R_{vir}$ range. We discuss the results for the NFW profile case. They span the mass range $10^{11}$ $M_\odot$ $h^{-1} \lesssim M \lesssim 10^{15}$ $M_\odot$ $h^{-1}$ and bin the objects in mass. In comparison with Neto et al. (2007), they find lower normalizations by about 15% due to a lower value of $\sigma_8$.

They also fit the $c-M$ relation taking into account the redshift evolution from $z = 0$ to $z = 2$, both for the complete sample and the relaxed objects only. They find a stronger dependence on redshift than what we find, both for the whole sample and relaxed systems. A possible explanation is that we fit in the range between $z = 0$ and $z = 1$, while they reach $z = 2$. If the redshift evolution is not constant with redshift, but it is weaker at low redshift, this could be a possible explanation for the different slope we find. They also find that the concentration of their halos is lower than the one inferred from X-ray observations and ascribed that fact to the effect of baryon physics that was missing in their simulations. However, in Duffy et al. (2010), they show that even including baryon physics in the simulations they cannot reproduce both observed concentrations and stellar fraction in galaxy groups and clusters. In general, at $z = 0$, when including metals and AGN feedback, they find lower concentrations compared to the dark matter only case, and the effect is more relevant in low-mass objects. When including only primordial cooling, they find higher concentrations compared to the dark matter only case, qualitatively in agreement with what we find in Fig. 4.5.
Prada et al. (2011), using the Bolshoi simulation (Klypin et al., 2011), evaluate the concentration of the halos using equation (4.7), binning the objects in $V_{max}$ and fitting a $c-\sigma(M, z)$ relation. They find that the concentration $c(\sigma)$ has a nearly universal U-shaped profile, with some small dependencies on redshift and cosmology. They also provide a fit of equation (4.4) for all their halos at $z = 0$. They find a higher normalization and a shallower slope in comparison with other works, as we do when we use equation (4.7), instead of equation (4.2), to evaluate the concentration. For relaxed halos, selected by $V_{max}$, they find a 5% higher normalization, as we do. Moreover, they find that the differences in concentrations for relaxed halos selected by $V_{max}$ are higher for high-mass objects than for low-mass ones.
In a more recent paper, Muñoz-Cuartas et al. (2011) fit the $c - M$ relation using a formula similar to equation (4.4), but incorporating the redshift dependence by letting $A$ and $B$ to be functions of redshift themselves. For the $c_{vir} - M_{vir}$ relation, at $z = 0$ they are able to reproduce the results of Macciò et al. (2008) with differences of the order of few percentage points.

We conclude this section noting that, when the values of the cosmological parameters are similar, our findings about the $c - M$ relation in the reference ΛCDM model are in good agreement with what already found in literature. So we can safely rely on our ΛCDM model as a reference, when comparing the impact of different dark energy models on the $c - M$ relation.

## 4.4 Dark energy models: results on the dark matter profiles

From now on, we start to compare the $c - M$ relation in the ΛCDM cosmology with the ones derived for the other cosmological models under investigation. The $c - M$ relation for galaxy clusters extracted from dark matter only simulations of different dark energy models, including RP and SUGRA, has been studied in Dolag et al. (2004). They fit a formula similar to equation (4.11), but keeping $C$ fixed to $-1$. They find that, when the same $\sigma_8$ is used for all the models, dark energy cosmologies have higher normalizations compared to ΛCDM, depending on the ratio between the growth factors through

$$A_{\rm DE} \rightarrow A_{\Lambda\rm CDM} \frac{D_{+,\rm DE}(z_{coll})}{D_{+,\Lambda\rm CDM}(z_{coll})} \ , \tag{4.12}$$

where the collapse redshifts $z_{coll}$ are evaluated following the prescriptions of Eke et al. (2001). When $\sigma_8$ values are normalized to CMB data, as we do in this work, dark energy cosmologies

have lower normalizations compared to ΛCDM. We find that, in order to recover the values of the normalization they quote in this case, equation (4.12) should be multiplied by the ratio between the values of $\sigma_8$, $\sigma_{8,\mathrm{DE}}/\sigma_{8,\Lambda\mathrm{CDM}}$. This fact goes in the same direction as what found in Macciò et al. (2008), where models with higher $\sigma_8$ also have a higher normalization of the $c - M$ relation.

We recall that to obtain the concentration we fit equation (4.1) in the range $[0.1 - 1]R_{200}$ using Poissonian errors and use the best-fit parameters to obtain $c_{200}$ from equation (4.2). Then we bin the objects in groups of 200, starting from less massive ones, and also define a relaxed sample by taking the relaxed objects inside each bin. Finally, we fit the binned $c - M$ relation with equation (4.4). We begin the comparison in this section with the dark matter only runs at $z = 0$, while in the following section we will study the hydrodynamical runs, also at higher redshifts.

In Table 4.7 we summarize the best-fit parameters, the standard errors and the reduced chi-squared of the $c - M$ relation (4.4) for the five cosmological models here considered, both for the complete and relaxed samples. For the complete sample, the differences in the normalization $A$ between ΛCDM and the other cosmological models are less tha 10%, with EQn being the only model having a higher normalization. The slope $B$ is within 5% of the ΛCDM value for all the models with the exception of EQn again, which shows a 30% flatter slope. For the slope the differences among the models, excluding EQn, are smaller than the standard errors, while for the normalization these differences are significant. If we limit ourselves to the best-fit values, given that the slopes are almost identical and that all the cosmological parameters except $\sigma_8$ are fixed, we expect that the normalizations should follow the values of $\sigma_8$, *i.e.* the higher $\sigma_8$ the higher the normalization (see Macciò et al., 2008), and $D_+$, *i.e.* the higher $D_+$ at $z_{coll}$ the higher the normalization (see Dolag et al., 2004). The quantity controlling the normalization is thus expected to be $\sigma_8 D_+(z_{coll})$. We plot the ratio between the value of $\sigma_8 D_+$ for a given dark energy model and the one for ΛCDM as a function of redshift in Fig. 4.10. Independently of the precise definition of $z_{coll}$, the cosmological model with the highest value of this quantity is ΛCDM, followed by RP, EQp, EQn, and SUGRA. We do expect the normalizations of the $c - M$ relation to follow the same order, with ΛCDM having the highest and SUGRA the lowest. Instead we see that, on the one hand, EQp which has the third highest $\sigma_8 D_+$ has the lowest normalization while, on the other hand, EQn which has the second lowest $\sigma_8 D_+$ has the highest normalization. The relative order of $\sigma_8 D_+$ and $A$ is preserved for ΛCDM, RP and SUGRA, as in Dolag et al. (2004). We hint that this behaviour is linked to the different evolution of the linear density contrast in extended quintessence models in comparison with ΛCDM and ordinary quintessence models, as pointed out in Subsection 2.1.2. In fact, in contrast with ΛCDM, RP and SUGRA, in EQ models $\delta_c$ does not approach the Einstein-de Sitter value during the matter-dominated era, but it is higher for positive values of the coupling constant $\xi$ and lower for negative values of $\xi$. For the relaxed sample, compared to ΛCDM, the differences in the normalization are less than 10%, while the differences in the slope can almost reach 15%, but they are compatible with the standard errors. Also in this case, the most extreme cosmologies are EQp and EQn, whose normalizations go in the opposite direction with respect to their $\sigma_8 D_+$. This fact reinforces the conclusions we have drawn from the complete sample. The values of the reduced chi-squared indicate that equation (4.4) is a good parametrization of the $c - M$ relation for almost all cosmological models. Only SUGRA has high values both for the complete and relaxed samples.

In a recent paper, Bhattacharya et al. (2011), using $N$-body numerical simulations of a ΛCDM cosmology, find indeed a dependence of $c_{200}$ on both $D_+$ and $\nu = \delta_c/\sigma(M, z)$. They evaluate

Table 4.7: Best-fit parameters, standard errors and reduced chi-squared $\tilde{\chi}^2$ of the $c-M$ relation (4.4) for dark matter only density profile fit in the region $[0.1-1]R_{200}$ for the complete and relaxed samples of the five different cosmological models at $z=0$.

| Model | $\sigma_8$ | A | $\sigma_A$ | $B$ | $\sigma_B$ | $\tilde{\chi}^2$ |
|---|---|---|---|---|---|---|
| | | dm (all) | | | | |
| ΛCDM | 0.776 | 3.59 | 0.05 | −0.099 | 0.011 | 0.48 |
| RP | 0.746 | 3.54 | 0.05 | −0.103 | 0.011 | 1.14 |
| SUGRA | 0.686 | 3.41 | 0.05 | −0.098 | 0.013 | 1.50 |
| EQp | 0.748 | 3.36 | 0.05 | −0.097 | 0.012 | 0.35 |
| EQn | 0.726 | 3.70 | 0.05 | −0.069 | 0.013 | 0.78 |
| | | dm (relaxed) | | | | |
| ΛCDM | 0.776 | 4.09 | 0.05 | −0.092 | 0.011 | 0.66 |
| RP | 0.746 | 4.08 | 0.05 | −0.081 | 0.011 | 0.92 |
| SUGRA | 0.686 | 3.94 | 0.06 | −0.081 | 0.012 | 1.55 |
| EQp | 0.748 | 3.84 | 0.05 | −0.097 | 0.011 | 1.32 |
| EQn | 0.726 | 4.25 | 0.06 | −0.081 | 0.013 | 0.51 |

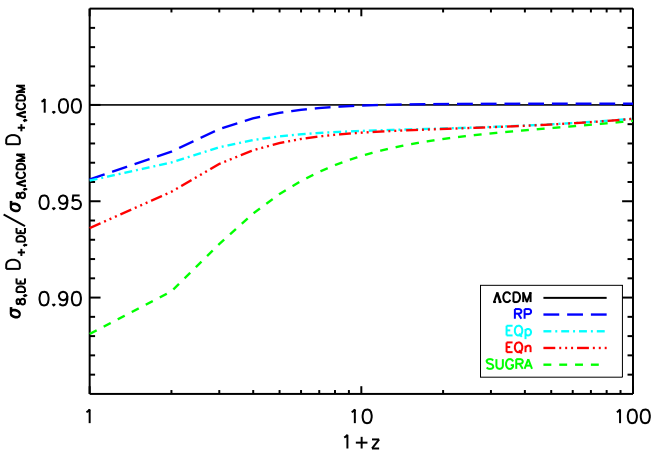


Figure 4.10: Ratio between the value of $\sigma_8 D_+$ for the ΛCDM (black), RP (blue), EQp (cyan), EQn (red), and SUGRA (green) cosmologies and the value for ΛCDM as a function of redshift.

the overall dependence of $c_{200}$ on the linear growth factor, both for their complete and relaxed samples, to be $D_+^{0.5}$. The dependence on the linear density contrast is also considered to be a power law, $\nu^a$. They find different values of $a$ for the complete and relaxed samples, namely $a=-0.35$ for the former and $a=-0.41$ for the latter. Thus, the higher the value of $D_+$ the higher the value of the concentration, and the lower the value of $\delta_c$ the higher the value of the concentration. Our findings on the EQp and EQn models are in agreement with this picture.

We plot the best-fits of the $c-M$ relation, along with the binned data for all the cosmological models, in Fig. 4.11. We clearly see that the results on the normalizations are due to differences in the concentrations over a wide mass range. If we look, for example, at the complete sample (top panel of Fig. 4.11), we see that the different slope of EQn is mainly originated by the less massive bin. But with the exception of this bin, EQn shows the highest concentration in almost all the mass bins, while in general EQp has the lowest concentration. For the relaxed sample (bottom panel of Fig. 4.11), the relative behaviour of the different cosmological models is even clearer, and indeed the differences in the slopes are

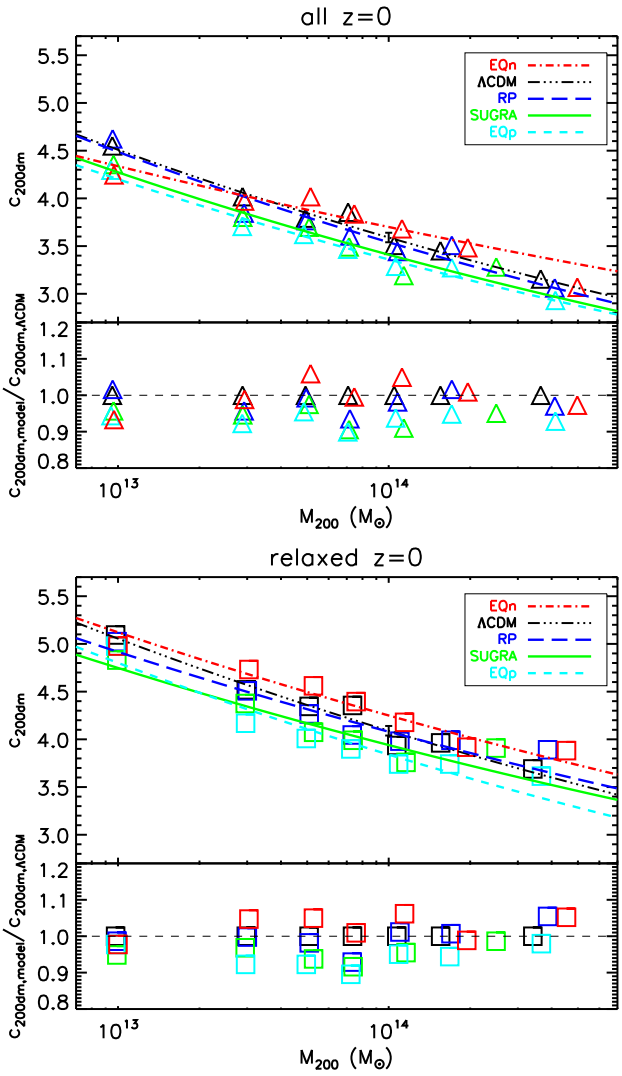


Figure 4.11: (Top panel) The values of $c_{200dm}$ in each mass bin for the complete sample of the ΛCDM (black), RP (blue), SUGRA (green), EQp (cyan), and EQn (red) cosmologies at $z = 0$. The lines of the corresponding colours are our best-fit of $c - M$ relation (4.4) and the vertical black bar is the error on the normalization of ΛCDM as listed in Table 4.6. The symbols in the low part of the panel are the ratios in each mass bin between $c_{200dm}$ for the model and $c_{200dm}$ for ΛCDM. The horizontal black dashed-line marks a unity ratio. (Bottom panel) The same as in the top panel, but for the relaxed sample.

less pronounced.

We also try to limit the fit of the $c - M$ relation to the halos with $M_{200m} > 10^{14}$ M$_\odot$ $h^{-1}$, in order to check the effect of including low-mass objects. We report the results in Table 4.8. For the complete sample, we note that the slopes and the normalizations are compatible to the fit including also low-mass objects, but that the standard errors are a factor of two higher for the normalization and a factor of four higher for the slope, meaning that the relation is less tight. Notable exceptions are EQn, which shows a steep slope, and SUGRA, which shows a positive trend of $c_{200dm}$ with mass, with a large error, and a consequently low normalization. The slope of EQn can be explained by the fact that, as we already pointed out, the lowest mass bin is the one with the lowest concentration, and excluding it from the fit results in a

Table 4.8: Best-fit parameters and standard errors of the $c - M$ relation (4.4) for dark matter only density profile fit in the region $[0.1 - 1]R_{200}$ for objects with $M_{200m} > 10^{14}$ $M_\odot$ $h^{-1}$ in the complete and relaxed samples of the five different cosmological models at $z = 0$.

| Model | $\sigma_8$ | $A$ | $\sigma_A$ | $B$ | $\sigma_B$ |
|---|---|---|---|---|---|
| | | dm (all) | | | |
| ΛCDM | 0.776 | 3.55 | 0.09 | −0.087 | 0.038 |
| RP | 0.746 | 3.54 | 0.11 | −0.080 | 0.046 |
| SUGRA | 0.686 | 3.18 | 0.12 | +0.035 | 0.060 |
| EQp | 0.748 | 3.35 | 0.10 | −0.080 | 0.044 |
| EQn | 0.726 | 3.74 | 0.11 | −0.114 | 0.048 |
| | | dm (relaxed) | | | |
| ΛCDM | 0.776 | 3.99 | 0.10 | −0.055 | 0.042 |
| RP | 0.746 | 4.00 | 0.12 | −0.017 | 0.045 |
| SUGRA | 0.686 | 3.73 | 0.13 | +0.051 | 0.059 |
| EQp | 0.748 | 3.76 | 0.11 | −0.027 | 0.046 |
| EQn | 0.726 | 4.19 | 0.13 | −0.079 | 0.053 |

steeper slope. The behaviour of SUGRA can be explained by the fact that this model lacks very massive objects (see Section 3.3), that are the ones with the lower concentration.

For the same reason, the $c - M$ relation for relaxed objects is flatter than when we include low-mass objects. This is expected, because we do not have the low-mass objects that have high concentration and we do not have the high-mass objects, which are in general more disturbed, that have low concentration. Thus, in this mass range, the relation is in general almost flat, with big uncertainties on the slope.

## 4.5 Dark energy models: results on the total profiles

In this section, we study the impact of baryon physics on the $c - M$ relation by analysing the hydrodynamical runs of our simulations for all the cosmological models under investigation. This allows us to understand the effects of the presence of a dynamical dark energy component on the internal matter distribution, including baryons, of the halos. We start this analysis with the objects at $z = 0$, then we will consider the redshift evolution of the $c - M$ relation by including also objects at $z = 0.5$ and $z = 1$. As we already explained in Section 4.1, first of all we fit equation (4.4) for the objects at $z = 0$, then, keeping fixed the best-fit values of $A$ and $B$, we fit equation (4.11) and evaluate the redshift evolution $C$.

In Table 4.9 we summarize the best-fit parameters, the standard errors and the reduced chi-squared of the $c - M$ relations (4.4) and (4.11) for the five cosmological models here considered, both for the complete and relaxed samples. For all the cosmologies, the values of $A$ are larger than in the dark matter only case, indicating that the inclusion of baryons leads to an increase in the concentration, while the standard errors remain the same. The slope is somewhat flatter than in the dark matter only case for all the cosmological models. We already noted both these features in the ΛCDM case (see Section 4.1), and the shallower slope can be explained by the fact that the increase in the concentration due to the presence of baryons is greater in high-mass objects than in low-mass ones. For the complete sample, the total $c - M$ relation reflects the one for dark matter, with the normalizations in the same order, apart from an exchange between EQp and SUGRA, and EQn having the highest value. The relaxed sample shows higher normalizations than the complete sample, as in the dark matter only case, while the slopes are very similar to the ones of the complete sample. Also

Table 4.9: Best-fit parameters, standard errors and reduced chi-squared $\tilde{\chi}^2$ of the $c-M$ relation (4.4) for total density profile fit in the region $[0.1-1]R_{200}$ for the complete and relaxed samples of the five different cosmological models at $z=0$, and of the $c-M$ relation (4.11) including also objects at $z=0.5$ and $z=1$, keeping the best-fit values of $A$ and $B$ found at $z=0$ fixed.

| Model | $\sigma_8$ | $A$ | $\sigma_A$ | $B$ | $\sigma_B$ | $\tilde{\chi}^2$ | $C$ | $\sigma_C$ | $\tilde{\chi}^2$ |
|---|---|---|---|---|---|---|---|---|---|
| | | tot (all) | | | | | | | |
| ΛCDM | 0.776 | 3.81 | 0.05 | −0.061 | 0.011 | 1.69 | −0.26 | 0.02 | 2.40 |
| RP | 0.746 | 3.72 | 0.05 | −0.073 | 0.012 | 1.06 | −0.15 | 0.02 | 1.98 |
| SUGRA | 0.686 | 3.68 | 0.06 | −0.057 | 0.013 | 0.70 | −0.05 | 0.02 | 3.68 |
| EQp | 0.748 | 3.69 | 0.05 | −0.085 | 0.012 | 0.88 | −0.20 | 0.02 | 2.99 |
| EQn | 0.726 | 3.94 | 0.05 | −0.052 | 0.012 | 1.55 | −0.21 | 0.02 | 1.77 |
| | | tot (relaxed) | | | | | | | |
| ΛCDM | 0.776 | 4.29 | 0.05 | −0.064 | 0.011 | 1.54 | −0.26 | 0.02 | 1.97 |
| RP | 0.746 | 4.24 | 0.05 | −0.075 | 0.010 | 2.86 | −0.15 | 0.02 | 1.84 |
| SUGRA | 0.686 | 4.25 | 0.06 | −0.045 | 0.011 | 1.14 | −0.08 | 0.02 | 1.11 |
| EQp | 0.748 | 4.13 | 0.05 | −0.091 | 0.010 | 2.02 | −0.16 | 0.02 | 2.79 |
| EQn | 0.726 | 4.48 | 0.05 | −0.057 | 0.012 | 1.62 | −0.16 | 0.02 | 1.02 |

in this case, in comparison with the order of $\sigma_8 D_+$, the extreme case are EQp and EQn, with ΛCDM, RP and SUGRA preserving the expected order. Thus, the trend with the linear density contrast we find in the dark matter only runs still holds in the hydrodynamical runs. The values of the reduced chi-squared indicate that for some models equation (4.4) is a good parametrization also for the $c-M$ relation of objects extracted from the hydrodynamical runs, at least when the complete sample is considered. For relaxed objects only SUGRA seems to be described quite well by this relation.

We plot the best-fits of the $c-M$ relation, along with the binned data for all the cosmological models, in Fig. 4.12. Also in this case, we see that differences in the concentration are present over a large mass range. For the complete sample, the lower normalization of SUGRA compared to RP is mainly due to low-mass objects, which flatten the relation. The same happens for the relaxed sample, where we also see a steepening in the relation from EQp, mainly due to high-mass objects.

As for the dark matter only case, we also limit our analysis at $z=0$ also to objects with $M_{200m} > 10^{14}$ $\mathrm{M}_\odot$ $h^{-1}$. We report the results in Table 4.10. We find that the normalizations are similar to the one found including also low-mass objects, but the standard errors are higher, and the slopes are generally flatter, with some exceptions. The most evident is SUGRA, for which the trend of $c_{200}$ with mass is increasing both in the complete and relaxed samples. For the complete sample, EQp and EQn show a steepening in the slope, a behaviour which is maintained by EQn also in the relaxed sample. For SUGRA, the explanation is the same as the dark matter only case, *i.e.* the lack of very high mass, low-concentration systems. For EQp and EQn, they show objects with low concentration in particular in the low-mass tail, so when excluding these objects, the result is a steepening in the slope (see Fig. 4.12). In all cases, the scatter in the relation is considerably higher than when we consider also low-mass objects, up to a factor of three in normalization and a factor of four in the slope.

For the hydrodynamical simulations, we also study the redshift evolution of the $c-M$ relation by fitting equation (4.11) keeping the values of $A$ and $B$ fixed to the best-fit values at $z=0$. We report the results in Table 4.9. For all the models, the evolution with redshift is negative, meaning that objects at higher redshifts have also lower concentrations. For the complete sample, the redshift dependence is stronger for ΛCDM than for the other cosmological models. The two EQ models have similar dependences, lower than ΛCDM, followed by

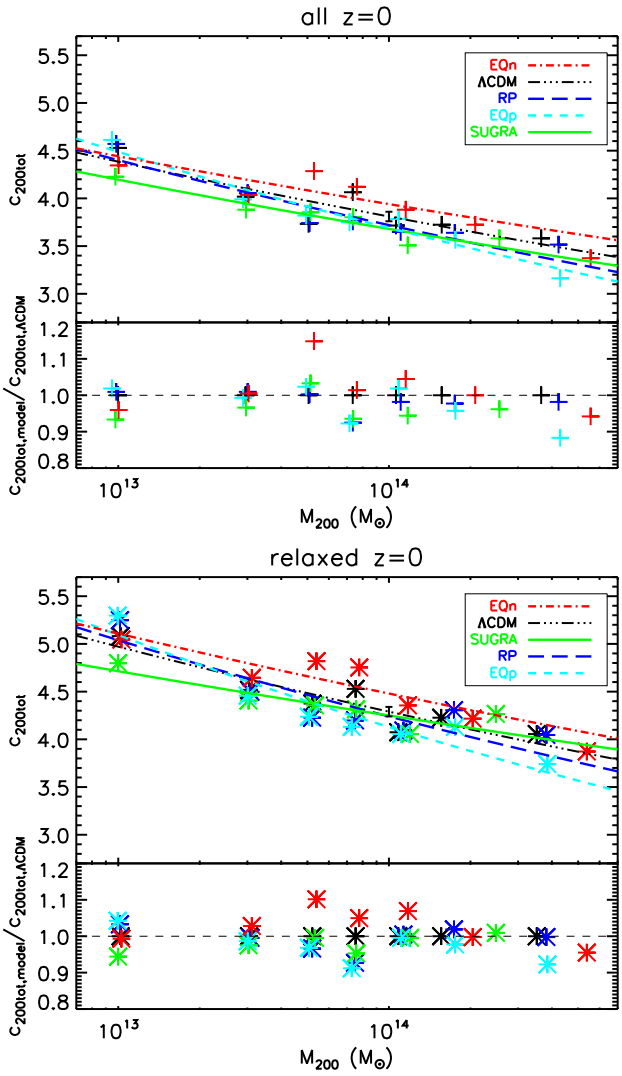


Figure 4.12: (Top panel) The values of $c_{200tot}$ in each mass bin for the complete sample of the ΛCDM (black), RP (blue), SUGRA (green), EQp (cyan), and EQn (red) cosmologies at $z = 0$. The lines of the corresponding colours are our best-fit of $c - M$ relation (4.4) and the vertical black bar is the error on the normalization of ΛCDM as listed in Table 4.6. The symbols in the low part of the panel are the ratios in each mass bin between $c_{200tot}$ for the model and $c_{200tot}$ for ΛCDM. The horizontal black dashed-line marks a unity ratio. (Bottom panel) The same as in the top panel, but for the relaxed sample.

RP and SUGRA, which shows a very weak evolution with redshift. If we focus on the relaxed sample, we see that the ΛCDM model still shows the strongest redshift dependence, analogous to the one for the complete sample. RP, EQp and EQn have similar evolutions, but while for RP it is the same as for the complete sample, for EQ models it is weaker. SUGRA have a flatter dependence compared to the other models, but more pronounced than for the complete sample. The values of the reduced chi-squared are rather high for all the cosmological models, both for the complete and relaxed samples. Two notable exceptions are the values for the relaxed samples of SUGRA and EQn. The results shown in Table 4.9 seem to indicate that equation (4.4), and its generalization (4.11), are only a limited parametrization of the $c - M$ relation of galaxy clusters extracted from hydrodynamical runs of cosmological simulations

Table 4.10: Best-fit parameters and standard errors of the $c-M$ relation (4.4) for total density profile fit in the region $[0.1-1]R_{200}$ for objects with $M_{200m} > 10^{14}$ $M_\odot$ $h^{-1}$ in the complete and relaxed samples of the five different cosmological models at $z = 0$.

| Model | $\sigma_8$ | $A$ | $\sigma_A$ | $B$ | $\sigma_B$ |
|---|---|---|---|---|---|
| | | tot (all) | | | |
| ΛCDM | 0.776 | 3.74 | 0.09 | −0.031 | 0.034 |
| RP | 0.746 | 3.67 | 0.11 | −0.027 | 0.040 |
| SUGRA | 0.686 | 3.49 | 0.13 | +0.027 | 0.061 |
| EQp | 0.748 | 3.83 | 0.10 | −0.130 | 0.041 |
| EQn | 0.726 | 3.94 | 0.12 | −0.083 | 0.045 |
| | | tot (relaxed) | | | |
| ΛCDM | 0.776 | 4.14 | 0.10 | −0.007 | 0.036 |
| RP | 0.746 | 4.17 | 0.11 | −0.004 | 0.041 |
| SUGRA | 0.686 | 4.00 | 0.15 | +0.069 | 0.061 |
| EQp | 0.748 | 4.14 | 0.11 | −0.054 | 0.043 |
| EQn | 0.726 | 4.41 | 0.14 | −0.068 | 0.052 |

including dynamical dark energy, and of its redshift evolution.

Finally, we check the evolution with redshift of the normalization $A$ both for the complete and relaxed samples for all the cosmological models. We do that by fitting the $c-M$ relation (4.4) by keeping fixed the slope at the best-fit value for the complete sample of ΛCDM at $z = 0$ (*i.e.* $B = -0.061$, see Table 4.9) and leaving only $A$ as a free parameter. We compare the different normalizations found by fitting equation (4.4) in this way for both the complete and relaxed samples at $z = 0$ and at $z = 1$. In this way, we freeze the slope at $z = 0$ for ΛCDM and force the other cosmological models, and objects at higher redshift, to adapt their normalization to this value. Thus we can have a snapshot of the imprint on dark energy on the concentration of the halos. We summarize the results in Table 4.11 and plot them in Fig. 4.13. Indeed we see that, for a given sample at $z = 0$, the normalization is decreasing going from ΛCDM to RP to SUGRA, as expected from $\sigma_8 D_+$. Then, as we already saw, the normalization of EQp is rather suppressed with respect to this simple expectation, while the one of EQn is enhanced, due to the different values of the linear density contrast $\delta_c$. If we move instead to $z = 1$, the relative behaviour of the different cosmological models changes. We find that, for both samples, the normalization is increasing going from ΛCDM to RP to SUGRA, while EQp is still suppressed and EQn is still enhanced. This finding is in agreement with the strong redshift evolution we found for ΛCDM and with the weak redshift evolution we found for SUGRA. There is an evolution from a low-normalization to a high-normalization relation for the first model, and vice versa for the latter. We show the values of the reduced chi-squared of the fit as a reference, but do not discuss them because we are imposing the slope for ΛCDM also to other models.

## 4.6 Dark energy models: discussion

In the final section of this chapter we discuss, for the different cosmologies, the results we have found for the dark matter only runs with the ones for the hydrodynamical runs. We start by comparing the normalization of the $c - M$ relation at $z = 0$ for the complete and relaxed samples in both runs. To do this, we fix the slope at the best-fit value for the complete sample of the dark matter only run for ΛCDM at $z = 0$ (*i.e.* $B = -0.099$, see Table 4.7) and we fit equation (4.4) with only $A$ as a free parameter. We summarize the results in

Table 4.11: Best-fit parameters, standard errors and reduced chi-squared $\tilde{\chi}^2$ of the $c-M$ relation (4.4), with $B$ fixed at the best-fit value for the complete sample of ΛCDM at $z = 0$, for total density profile fit in the region $[0.1 - 1]R_{200}$ for the complete and relaxed samples of the five different cosmological models at $z = 0$ and $z = 1$.

| | | $z = 0$ | | | | | | $z = 1$ | | | | | |
|---|---|---|---|---|---|---|---|---|---|---|---|---|---|
| Model | $\sigma_8$ | $A$ | $\sigma_A$ | $\tilde{\chi}^2$ | $A$ | $\sigma_A$ | $\tilde{\chi}^2$ | $A$ | $\sigma_A$ | $\tilde{\chi}^2$ | $A$ | $\sigma_A$ | $\tilde{\chi}^2$ |
| | | tot (all) | | | tot (relaxed) | | | tot (all) | | | tot (relaxed) | | |
| ΛCDM | 0.776 | 3.81 | 0.05 | 1.69 | 4.30 | 0.05 | 1.30 | 3.21 | 0.05 | 6.43 | 3.62 | 0.06 | 2.09 |
| RP | 0.746 | 3.74 | 0.05 | 1.08 | 4.27 | 0.05 | 2.69 | 3.43 | 0.06 | 4.27 | 3.84 | 0.08 | 2.05 |
| SUGRA | 0.686 | 3.67 | 0.05 | 0.58 | 4.20 | 0.05 | 1.28 | 3.49 | 0.07 | 1.81 | 3.85 | 0.08 | 0.43 |
| EQp | 0.748 | 3.74 | 0.04 | 1.49 | 4.20 | 0.05 | 3.13 | 3.26 | 0.06 | 6.09 | 3.70 | 0.07 | 2.72 |
| EQn | 0.726 | 3.92 | 0.05 | 1.38 | 4.47 | 0.05 | 1.37 | 3.48 | 0.07 | 3.43 | 4.02 | 0.08 | 1.69 |

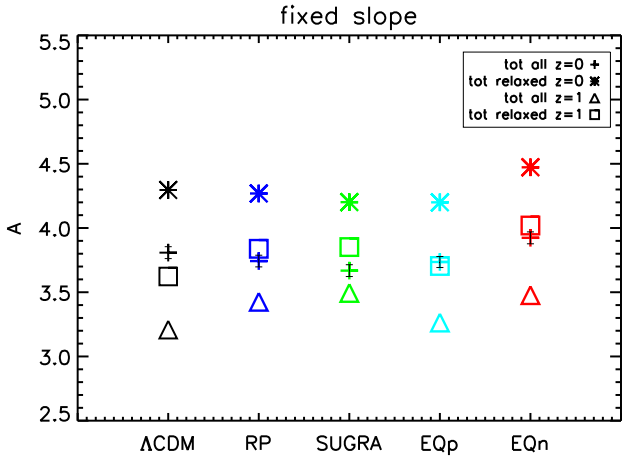


Figure 4.13: Best-fit normalization comparison for equation (4.4) with $B$ fixed at the best-fit value for the complete sample of ΛCDM at $z = 0$ for the ΛCDM (black), RP (blue), SUGRA (green), EQp (cyan), and EQn (red) cosmologies. Crosses: total profile fit $z = 0$, complete sample. Stars: total profile fit $z = 0$, relaxed sample. Triangles: total profile fit $z = 1$, complete sample. Squares: total profile fit $z = 1$, relaxed sample. The vertical bars are the standard errors for the normalization of the complete sample at $z = 0$.

Table 4.12 and plot them in Fig. 4.14, which contains almost all the information on the $c - M$ relation at $z = 0$ for the cosmological models under investigation. Indeed, we see that inside each sample, objects in the dark matter only runs have a lower normalization than objects in the hydrodynamical runs, independently of cosmology and dynamical state. Moreover, inside each run, relaxed objects have a higher normalization compared to the complete sample. Then, as a general trend, the normalization is decreasing going from ΛCDM to RP to SUGRA, independently of the run and the dynamical state. Finally EQn always has the highest normalization while EQp, at least for the dark matter only runs, alway has the lowest. In particular, EQn has the highest normalization also in hydrodynamical runs, while the suppression of the concentration in EQp is somehow mitigated in these runs. The behaviour of ΛCDM, RP and SUGRA is in agreement with the simple idea that the normalization of the $c - M$ relation is driven by the value of $\sigma_8 D_+$, but the one of EQp and EQn is not. We ascribe the behaviour of the two EQ models to the different evolution of the linear density contrast in the spherical collapse prescription, which is higher than the

Table 4.12: Best-fit parameters, standard errors and reduced chi-squared $\tilde{\chi}^2$ of the $c - M$ relation (4.4), with $B$ fixed at the best-fit value for the dark matter only complete sample of ΛCDM at $z = 0$, for dark matter only and total density profile fit in the region $[0.1 - 1]R_{200}$ for the complete and relaxed samples of the five different cosmological models at $z = 0$.

| Model | $\sigma_8$ | $A$ | $\sigma_A$ | $\tilde{\chi}^2$ | $A$ | $\sigma_A$ | $\tilde{\chi}^2$ | $A$ | $\sigma_A$ | $\tilde{\chi}^2$ | $A$ | $\sigma_A$ | $\tilde{\chi}^2$ |
|---|---|---|---|---|---|---|---|---|---|---|---|---|---|
| | | dm (all) | | | dm (relaxed) | | | tot (all) | | | tot (relaxed) | | |
| ΛCDM | 0.776 | 3.59 | 0.05 | 0.48 | 4.08 | 0.04 | 0.62 | 3.76 | 0.04 | 3.36 | 4.23 | 0.05 | 3.06 |
| RP | 0.746 | 3.55 | 0.04 | 0.97 | 4.08 | 0.04 | 0.62 | 3.76 | 0.04 | 3.36 | 4.23 | 0.05 | 3.06 |
| SUGRA | 0.686 | 3.41 | 0.04 | 1.20 | 3.89 | 0.04 | 1.69 | 3.58 | 0.04 | 2.77 | 4.09 | 0.04 | 5.56 |
| EQp | 0.748 | 3.36 | 0.04 | 0.30 | 3.83 | 0.04 | 1.11 | 3.66 | 0.04 | 0.96 | 4.11 | 0.04 | 1.77 |
| EQn | 0.726 | 3.65 | 0.04 | 1.56 | 4.21 | 0.05 | 0.74 | 3.86 | 0.05 | 3.81 | 4.39 | 0.05 | 3.46 |

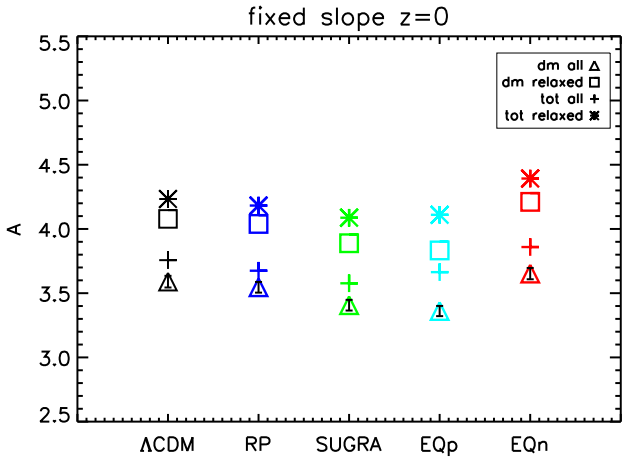


Figure 4.14: Best-fit normalization comparison for equation (4.4) with $B$ fixed at the best-fit value for the dark matter only complete sample of ΛCDM at $z = 0$ for the ΛCDM (black), RP (blue), SUGRA (green), EQp (cyan), and EQn (red) cosmologies. Triangles: dark matter profile fit, complete sample. Squares: dark matter profile fit, relaxed sample. Crosses: total profile fit, complete sample. Stars: total profile fit, relaxed sample.

Einstein-de Sitter value for EQp and lower for EQn (see Subsection 2.1.2), leading thus to a lower normalization for EQn and to a higher normalization fro EQp (see Section 4.4). We show the values of the reduced chi-squared of the fit as a reference, but do not discuss them because we are imposing the slope for ΛCDM also to other models.

Finally, we compare the concentrations obtained from the dark matter only runs with the one obtained from the hydrodynamical runs. We do this by taking the ratio between $c_{200tot}$ and $c_{200dm}$ in each mass bin both for the complete and relaxed samples at $z = 0$. We plot the results in Fig. 4.15. In the top panel we analyse the ratio for the complete sample. We see that all the cosmological models have $c_{200tot}/c_{200dm}$ increasing with increasing mass. This fact confirms that the baryon physics influences more the concentration of high-mass objects compared to low-mass ones (see Fig. 4.5). In particular, while ΛCDM, RP and SUGRA have $c_{200tot} < c_{200dm}$ in some low-mass bins, EQp and EQn have in general $c_{200tot} > c_{200dm}$, with a less pronounced evolution with mass. In the bottom panel we analyse the ratio for the relaxed sample. Here the situation is a bit different. All the cosmological models still show a general increase of $c_{200tot}/c_{200dm}$ with increasing mass, but the evolution is rather shallow. In particular, very massive objects in the RP, EQp and EQn models have low values

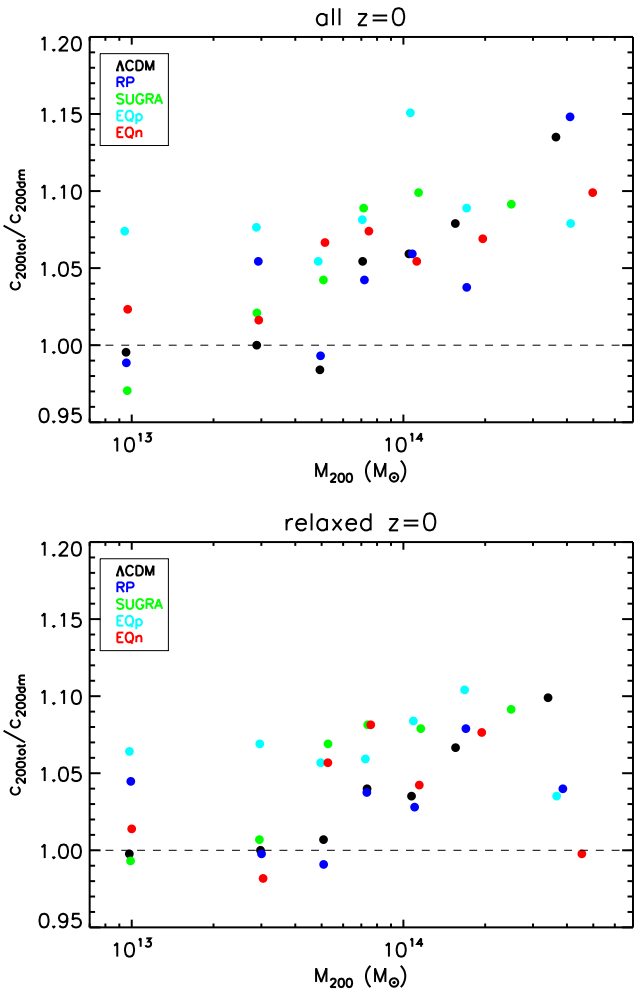


Figure 4.15: Ratio in each mass bin between $c_{200tot}$ and $c_{200dm}$ for the complete sample of the ΛCDM (black), RP (blue), SUGRA (green), EQp (cyan), and EQn (red) cosmologies at $z = 0$. The dashed black line traces the one-to-one relation. (Bottom panel) The same as in the top panel, but for the relaxed sample.

of these ratio. In any case, with few exceptions in some mass bins, we generally find that $c_{200tot} > c_{200dm}$ for all models. This analysis demonstrates that the inclusion of baryon physics in the simulations is unable to solve the discrepancy between the predicted and observed $c-M$ relation. Indeed, in none of the cases we have analysed, the effect of the baryons is to increase the concentration of low-mass objects without affecting the one of the high-mass ones. Of course a possible explanation of this fact can be that we do not include some kinds of feedback in our simulations, in particular AGN feedback. Still, Duffy et al. (2010) already showed that none of the different hydrodynamical treatments they tried was able to both explain the observed $c - M$ relation and the stellar fraction in galaxy clusters.

Nevertheless, we have seen that different dark energy models leave an imprint in the $c-M$ relation. In particular, as already noted by Dolag et al. (2004), in ordinary quintessence models, like our RP and SUGRA, the normalization of this relation compared to the ΛCDM one is driven by the value of $\sigma_8 D_+(z_{coll})$ with respect to the value for ΛCDM. We find that the same thing is no longer valid for extended quintessence models like our EQp and EQn. Indeed, in this cases we find that, in presence of a positive coupling, the value of the normalization

is lower than what expected from $\sigma_8 D_+(z_{coll})$ while in presence of a negative coupling it is increased. We interpret this behaviour as due to the different evolution of the linear density contrast in the spherical collapse model, as explained in Subsection 4.4. Unfortunately, given the discrepancies between the observed and the predicted $c - M$ relation, it is difficult to use the observed $c - M$ relation to disentangle different cosmological models through the imprints left by dark energy.

## 4.7 $c - M$ relation: summary

In this chapter we have studied the $c - M$ relation for the halos extracted from the *Padme* simulation set. From our analysis we draw the following conclusions.

- Concentration: the definition itself of the concentration of a halo can lead to very different results. For the reference ΛCDM model at $z = 0$, we see that the usual fit of a NFW profile, depending on the way in which the errors are weighted and the concentration is evaluated from the fit, gives values of the concentration with differences, at worst, of the order of 5%. The method used by Prada et al. (2011), instead, returns similar values of the concentration only for super-relaxed objects, while in general gives higher values of the concentration, up to 20%. The quantity $R_{2500}/R_{500}$, which is model independent, is found to be well correlated with the NFW value of the concentration for dark matter only simulations, indicating that dark matter halos are indeed well described by a NFW profile. In a given mass bin, the mean concentration is higher and the intrinsic scatter is lower for objects that are in a relaxed dynamical state and well described by a NFW profile. Halos extracted from the hydrodynamical runs have, in general, higher concentrations than their dark matter only counterparts. The effect is more evident in high-mass systems, due to a higher baryon fraction in the inner regions.

- $c - M$ relation: limiting our analysis to the ΛCDM model, there is a big intrinsic scatter in the values of the concentration for objects of a given mass, ranging from 15% up to 40% depending on mass and dynamical state. Nevertheless, if we consider the mean value of concentration in a given mass range, there is a good correlation between concentration and mass. The concentration is slightly decreasing with increasing mass, and this relation is well described by a power law, with two free parameters, the normalization and the slope. The normalization, that we define as the value of the concentration of a halo with a mass of $10^{14}$ $M_\odot$, is increasing going from the complete sample to the relaxed and super-relaxed samples. The slope is similar for the different samples considered. In general, we find a good agreement with the results from other works in literature.
  The normalization is higher for objects extracted from the hydrodynamical runs compared to the one of the dark matter only runs. The slope is flatter for the hydrodynamical simulations than for the dark matter only ones. This is expected because massive objects from the hydrodynamical simulations have higher concentrations than their dark matter only counterparts.

- Redshift dependence: the $c - M$ relation shows an evolution with redshift, with concentration decreasing with increasing redshift. For the ΛCDM model, considering also objects at $z = 0.5$ and $z = 1$, the redshift evolution is more pronounced for the dark matter only simulations than for the hydrodynamical ones, while it is similar for the complete and relaxed samples.

- Dark energy models: we find that the normalization of the $c - M$ relation in dynamical dark energy cosmologies is different from the ΛCDM one, while the slopes are more compatible. In particular, at $z = 0$, the differences in the normalizations of RP and SUGRA compared to ΛCDM reflect the differences in $\sigma_8 D_+$, with models having a higher $\sigma_8 D_+$ also having a higher normalization. This simple scheme is not valid for the EQp and EQn scenarios. In the former case, the normalization is lower than expected from $\sigma_8 D_+$, while in the latter it is higher, and indeed EQn is always the model with the highest normalization, regardless of the dynamical state of the objects or the runs they are extracted from. This behaviour is due to the different value of the linear density contrast in these models, being higher than the Einstein-de Sitter value of ΛCDM and ordinary quintessence models for EQp and lower for EQn.
  For objects extracted from the hydrodynamical runs, we also study the redshift evolution of the $c - M$ relation. We find different evolution for different dark energy models. ΛCDM has the strongest evolution, while SUGRA has the weakest, while RP lies in between. For these three models, the behaviour is similar for the complete and relaxed samples. EQp and EQn models, instead, show an evolution similar to ΛCDM for the complete sample and similar to RP for the relaxed sample. The interesting thing to note is that at $z = 0$ the normalization decreases from ΛCDM to RP to SUGRA, while at $z = 1$ the situation is completely reversed. Independently of redshift, EQp has always the lowest normalization while EQn has always the highest.

# Conclusions

In this work we have analysed a sample of galaxy clusters extracted from the *Padme* simulation set, a set of dark matter only and hydrodynamical simulations of different cosmological models with dynamical dark energy. We simulate a cosmological box of size $(300 \text{ Mpc } h^{-1})^3$, resolved with $(768)^3$ dark matter particles, including the same amount of gas particles in the hydrodynamical runs. The reference cosmology is a concordance ΛCDM model normalized to WMAP3 data. The others are two quintessence models, one with a RP and the other with a SUGRA potential, and two extended quintessence models, with a positive and a negative coupling between quintessence and gravity, indicated as EQp and EQn, respectively. All models have a different dark energy equation of state $w(z)$ and a different growth factor $D_+(z)$. Moreover EQp and EQn also have a different linear density contrast $\delta_c$. Since all models are normalized to CMB data, they have different $\sigma_8$, and thus different structure formation histories. The aim of this work is to study the imprints of the different dark energy models on large virialized objects like galaxy clusters.

First, we focus on the general properties of the considered objects, in particular the mass function, the X-ray $L - T$ relation, the X-ray luminosity and temperature functions (XLF and XTF respectively) and finally the baryonic fraction in terms of the depletion parameters $b_{star}$, $b_{gas}$ and $b_{bar}$ defined in equation (3.8). We select and study objects at three different redshifts, $z = 0$, $z = 0.5$, and $z = 1$, with $M_{200m} \geq 10^{14} \text{M}_\odot h^{-1}$. We also define a criterion to distinguish between relaxed and unrelaxed clusters.
We find that our ΛCDM model is in good agreement with the observed mass function of Vikhlinin et al. (2009a) and $L - T$ relation of Pratt et al. (2009), and can thus be used a reference to study other dark energy models. The other models form less clusters of a given mass with respect to ΛCDM, following the values of $\sigma_8$, and so have different mass functions. The differences we see in the mass functions remain also when the X-ray proxies for the mass are considered. In particular, the X-ray temperature and the $Y_X$ parameter, defined the gas mass times the X-ray temperature, are found to be good indicators of the mass function. So, in principle, X-ray observations of galaxy clusters can be used to disentangle among different dark energy models through the mass function.
The analysis of the baryon fraction shows that there are no significant differences in the global distribution of gas and stars inside halos in the cosmological models under investigation. Indeed, evolved and relaxed clusters, if studied in regions sufficiently far from the centre, reveal to be very similar despite the different dark energy models considered. It means that techniques that rely on $f_{gas}$ to derive other cosmological parameters can be safely used even in the case in which the underlying model is one of the quintessence models discussed in this work.

Then, we focus on the $c - M$ relation for objects extracted both from the dark matter only and hydrodynamical runs. In this case, we also consider halos with lower masses, down to $M_{200m} \approx 10^{13} \mathrm{M}_{\odot} h^{-1}$, and bin the objects in mass.
We find that the dark matter only $c - M$ relation for our reference ΛCDM model is in good agreement with the one of Macciò et al. (2008) for the WMAP3 cosmology, both for the complete and relaxed samples. Thus, we use ΛCDM as a guide to study the impact of dark energy on the $c - M$ relation. We find that RP and SUGRA have lower normalizations with respect of ΛCDM, following the values of $\sigma_8 D_+$. EQp and EQn do not follow this simple rule because they have also different $\delta_c$ with respect to the other models. In particular, we find a higher normalization for a lower $\delta_c$ (EQn) and a lower normalization for a higher $\delta_c$ (EQp). This is an important point, because in principle one can use the $c - M$ relation to break the degeneracy between models having the same $\sigma_8 D_+$.
In order to compare findings from our simulations to real data, we also study the $c - M$ relation for halos extracted from the hydrodynamical runs. We find that the impact of baryons on the $c - M$ relation is to increase the normalization and to flatten the slope, due to a high concentration of baryon in the inner regions of massive objects in our simulations. Still, the important features for dark energy we find in dark matter only runs are also present in the hydrodynamical runs. Unfortunately, there are still big discrepancies between the observed and predicted $c - M$ relations, both in slope and normalization, discrepancies that we cannot eliminate neither considering hydrodynamical simulations nor limiting the analysis to relaxed systems.

In the end, we can conclude that in models with dynamical dark energy considered in this work, the evolving cosmological background leads to different formation histories of galaxy clusters, but the baryon physics is not affected in a relevant way. So, on the one hand, galaxy clusters can effectively be used as a probe to distinguish among different dark energy models through their mass function or $c - M$ relation. On the other hand, the distribution of baryons inside cluster is similar in the different models, and thus $f_{gas}$ can be used to derive other cosmological parameters also in these cosmologies.

# Appendix A

# Notes on General Relativity

In this appendix we derive the important quantities of General Relativity used throughout this work. A comprehensive treatment of this topic can be found in Wald (1984).

## A.1 Notation

For a scalar field $\phi$, covariant differentiation is simply partial differentiation:

$$\nabla_a \phi = \phi_{;a} \equiv \partial_a \phi = \phi_{,a} \tag{A.1}$$

For a contravariant vector field $v^a$, we have:

$$\nabla_b v^a = v^a{}_{;b} \equiv \partial_b v^a + \Gamma^a{}_{cb} v^c \tag{A.2}$$

For a covariant vector field $u_a$, we have:

$$\nabla_b u_a = u_{a;b} \equiv \partial_b u_a - \Gamma^c{}_{ab} u_c \tag{A.3}$$

For a type (2,0) tensor field $T^{ab}$, we have:

$$\nabla_c T^{ab} = T^{ab}{}_{;c} \equiv \partial_c T^{ab} + \Gamma^a{}_{dc} T^{db} + \Gamma^b{}_{dc} T^{ad} \tag{A.4}$$

For a type (0,2) tensor field $T_{ab}$, we have:

$$\nabla_c T_{ab} = T_{ab;c} \equiv \partial_c T_{ab} - \Gamma^d{}_{ac} T_{db} - \Gamma^d{}_{bc} T_{ad} \tag{A.5}$$

For a type (1,1) tensor field $T_b{}^a$, we have:

$$\nabla_c T_b{}^a = T_b{}^a{}_{;c} \equiv \partial_c T_b{}^a = \Gamma^a{}_{dc} T_b{}^d - \Gamma^d{}_{bc} T_d{}^a \tag{A.6}$$

## A.2 General Relativity

*Spacetime is a manifold $M$ on which there is defined a Lorentz metric $g_{\mu\nu}$.*
*The curvature of $g_{\mu\nu}$ is related to the matter distribution in spacetime by Einstein's equation*

$$G_{\mu\nu} \equiv R_{\mu\nu} - \frac{1}{2} R g_{\mu\nu} = 8\pi G T_{\mu\nu} \ . \tag{A.7}$$

- A *manifold* is a set of pieces that "look like" open subsets of $\mathbb{R}^n$ such that these pieces can be "sewn together" smoothly.
- Lorentz metric signature: $(-,+,+,+)$
- $R_{\mu\rho} = R_{\mu\nu\rho}{}^{\nu}$ Ricci tensor, trace over the second and fourth (or first and third) indices of the Riemann tensor.
- $R = R_{\mu}{}^{\mu}$ scalar curvature, trace of the Ricci tensor.
- $T_{\mu\nu}$ stress-energy tensor.
- Bianchi identity $\nabla^{\mu} G_{\mu\nu} = 0$ implies local energy conservation.
- $\nabla_{\mu}$ (unique) derivative operator associated with $g_{\mu\nu}$, *i.e.* $\nabla_{\mu} g_{\nu\rho} = 0$.

For a perfect fluid

$$T_{\mu\nu} = \rho u_{\mu} u_{\nu} + p(g_{\mu\nu} + u_{\mu} u_{\nu}) \ , \tag{A.8}$$

where $u_{\mu}$ is the 4-velocity, *i.e.* the unit tangent (as measured by $g_{\mu\nu}$) to its world line, of a particle. Local energy conservation holds:

$$\nabla^{\mu} T_{\mu\nu} = 0 \ . \tag{A.9}$$

Klein-Gordon equation for a scalar field $\phi$ in curved spacetime:

$$\partial^{\mu} \partial_{\mu} \phi - m^2 \phi = 0 \ . \tag{A.10}$$

Stress tensor of the field:

$$T_{\mu\nu} = \partial_{\mu}\phi \partial_{\nu}\phi - \frac{1}{2} g_{\mu\nu} (\partial^{\rho}\phi \partial_{\rho}\phi + m^2 \phi^2) \ , \tag{A.11}$$

$$\nabla^{\mu} T_{\mu\nu} = 0 \ . \tag{A.12}$$

## A.3 Lagrangian formulation

Hilbert action

$$S_H = \int d^4x \mathcal{L}_H \ , \tag{A.13}$$

integral over spacetime of a Lagrangian density

$$\mathcal{L}_H = \sqrt{-g}R = \sqrt{-g}R_{\mu\nu}g^{\mu\nu} \ , \tag{A.14}$$

where $g$ denotes the determinant of $g_{\mu\nu}$. Given that

$$\delta(\sqrt{-g}) = -\frac{1}{2}\sqrt{-g}g_{\mu\nu}\delta g^{\mu\nu} \ , \tag{A.15}$$

the variation of the Hilbert action with respect to the metric $g_{\mu\nu}$ yields

$$\frac{\delta S_H}{\delta g^{\mu\nu}} = \sqrt{-g}(R_{\mu\nu} - \frac{1}{2}Rg_{\mu\nu}) = 0 \ , \tag{A.16}$$

Einstein's equation in vacuum.

Indeed

$$\begin{aligned} \delta\mathcal{L}_H &= \sqrt{-g}R_{\mu\nu}\delta g^{\mu\nu} + R_{\mu\nu}g^{\mu\nu}\delta(\sqrt{-g}) + \sqrt{-g}g^{\mu\nu}\delta(R_{\mu\nu}) = \\ &= \sqrt{-g}(R_{\mu\nu} - \frac{1}{2}Rg_{\mu\nu})\delta g^{\mu\nu} + \sqrt{-g}\nabla^\mu v_\mu \ , \end{aligned}$$

where

$$v_\mu = \nabla^\nu(\delta g_{\mu\nu}) - g^{\rho\sigma}\nabla_\mu(\delta g_{\rho\sigma}) \ . \tag{A.17}$$

When considering the variation of the Hilbert action, the term

$$\int d^4x\sqrt{-g}\nabla^\mu v_\mu \tag{A.18}$$

is the integral of a divergence, $\nabla^\mu v_\mu$, with respect to the natural volume element $d^4x$. Hence, by Stroke's theorem, this integral contributes only on a boundary term.
In presence of matter

$$\mathcal{L} = \frac{1}{\alpha_M}\mathcal{L}_H + \mathcal{L}_M \ , \tag{A.19}$$

where $\mathcal{L}_M$ is the Lagrangian density for matter.
The variation of the action

$$S = \frac{1}{\alpha_M} S_H + S_M = \int d^4x \left( \frac{1}{\alpha_M} \sqrt{-g} R + \mathcal{L}_M \right) \tag{A.20}$$

with respect to the metric $g_{\mu\nu}$ yields

$$\frac{\delta S}{\delta g^{\mu\nu}} = \frac{1}{\alpha_M} \sqrt{-g} (R_{\mu\nu} - \frac{1}{2} R g_{\mu\nu}) + \frac{\delta S_M}{\delta g^{\mu\nu}} = 0 \ ; \tag{A.21}$$

*i.e.*, for a perfect fluid,

$$T_{\mu\nu} = -\frac{\alpha_M}{8\pi G} \frac{1}{\sqrt{-g}} \frac{\delta S_M}{\delta g^{\mu\nu}} = \rho u_\mu u_\nu + p(g_{\mu\nu} + u_\mu u_\nu) \tag{A.22}$$

in order to recover Einstein's equation.
Lagrangian formalism of a Klein-Gordon scalar field $\phi$ in a Minkowski spacetime (*i.e.* four-dimensional flat Lorentz signature space)

$$\mathcal{L}_{KG} = -\frac{1}{2} (\partial_\mu \phi \partial^\mu \phi + m^2 \phi^2) \ , \tag{A.23}$$

where $\partial_\mu$ is the derivative operator associated with the flat metric $\eta_{\mu\nu}$.
The variation of the action

$$S_{KG} = \int d^4x \left[ -\frac{1}{2} (\partial_\mu \phi \partial^\mu \phi + m^2 \phi^2) \right] \tag{A.24}$$

with respect to the scalar field $\phi$ yields

$$\frac{\delta S_{KG}}{\delta \phi} = \partial_\mu \partial^\mu \phi - m^2 \phi = 0 \ , \tag{A.25}$$

Klein-Gordon equation.
In curved spacetime

$$\mathcal{L}_{KG} = -\frac{1}{2} \sqrt{-g} (g^{\mu\nu} \partial_\mu \phi \partial_\nu \phi + m^2 \phi^2) \tag{A.26}$$

and, if

$$\mathcal{L} = \frac{1}{\alpha_{KG}} \mathcal{L}_H + \mathcal{L}_{KG} \ , \tag{A.27}$$

then

$$T_{\mu\nu} = -\frac{\alpha_{KG}}{8\pi G} \frac{1}{\sqrt{-g}} \frac{\delta S_{KG}}{\delta g^{\mu\nu}} = \partial_\mu \phi \partial_\nu \phi - \frac{1}{2} g_{\mu\nu} (\partial^\rho \phi \partial_\rho \phi + m^2 \phi^2) \tag{A.28}$$

in order to recover Einstein's equation, with $\alpha_{KG} = 16\pi G$.

In general, for a Lagrangian of the form

$$\mathcal{L}_\phi = \sqrt{-g}\left(-\frac{1}{2}g^{\mu\nu}\partial_\mu\phi\partial_\nu\phi - V(\phi)\right) \tag{A.29}$$

the Euler-Lagrange equation

$$\partial_\mu\left(\frac{\partial\mathcal{L}_\phi}{\partial(\partial_\mu\phi)}\right) - \frac{\partial\mathcal{L}_\phi}{\partial\phi} = 0 \tag{A.30}$$

reads

$$-\partial_\mu\partial^\mu\phi + \frac{\partial V(\phi)}{\partial\phi} = 0\ . \tag{A.31}$$

Klein-Gordon equation (A.10) is recovered for

$$V(\phi) = \frac{1}{2}m^2\phi^2\ . \tag{A.32}$$

## A.4 Homogeneity and Isotropy

*Homogeneity* is the property of being identical everywhere in space, while *isotropy* is the property of looking the same in every direction.
In the case of a homogeneous and isotropic spacetime, the surfaces $\Sigma_t$ of homogeneity must be orthogonal to the tangents, $u^\mu$, to the world lines of the isotropic observers.
The spacetime metric, $g_{\mu\nu}$, induces a Riemannian metric, $h_{\mu\nu}(t)$, on each $\Sigma_t$ by restricting the action of $g_{\mu\nu}$ on each $p \in \Sigma_t$ to vectors tangent to $\Sigma_t$.

- (i) Because of homogeneity, there must be isometries of $h_{\mu\nu}$ which carry any $p \in \Sigma_t$ into any $q \in \Sigma_t$.
- (ii) Because of isotropy, it must be impossible to construct any geometrically preferred vectors on $\Sigma_t$.

(ii) implies that the Riemann tensor ${}^{(3)}R_{\mu\nu\rho}{}^\sigma$ constructed from $h_{\mu\nu}$ on $\Sigma_t$ satisfies

$${}^{(3)}R_{\mu\nu\rho\sigma} = Kh_{\rho[\mu}h_{\nu]\sigma} = \frac{K}{2}(h_{\rho\mu}h_{\nu\sigma} - h_{\rho\nu}h_{\mu\sigma})\ . \tag{A.33}$$

(i) [but also (ii)] implies that $K$ must be a constant.

A space where equation (A.33) is satisfied (with $K$ = constant) is called a *space of constant curvature*.

All positive values of $K$ (*closed* universe) are attained by the 3-spheres. In spherical coordinates, the metric of the unit 3-sphere is

$$dl^2 = d\psi^2 + \sin^2\psi(d\theta^2 + \sin^2\theta d\phi^2) \ . \tag{A.34}$$

The value $K = 0$ (*flat* universe) is attained by the ordinary three-dimensional flat space. In Cartesian coordinates, this metric is

$$dl^2 = dx^2 + dy^2 + dz^2 \ . \tag{A.35}$$

Finally, all negative values of $K$ (*open* universe) are attained by the three dimensional hyperboloids. In hyperbolic coordinates, the metric of the unit hyperboloid is

$$dl^2 = d\psi^2 + \sinh^2\psi(d\theta^2 + \sin^2\theta d\phi^2) \ . \tag{A.36}$$

Since the isotropic observers are orthogonal to the homogeneous surfaces, we may express the four-dimensional spacetime metric $g_{\mu\nu}$ as

$$g_{\mu\nu} = -u_\mu u_\nu + h_{\mu\nu}(t) \ , \tag{A.37}$$

where for each $t$, $h_{\mu\nu}(t)$ is the metric of either a sphere, flat Euclidean space, or a hyperboloid. Expressed in convenient coordinates, the spacetime metric takes the form

$$ds^2 = g_{\mu\nu}dx^\mu dx^\nu = -dt^2 + a^2(t)dl^2 \ , \tag{A.38}$$

where $t$ is the proper time of the isotropic observers and $dl^2$ is given either by (A.34), (A.35), or (A.36).
The general form of the metric (A.38) is called a *Robertson-Walker* cosmological model.
It can be shown that the Robertson-Walker metric (A.38) can be expressed in the form

$$ds^2 = dt^2 + a^2(t)\left[\frac{dr^2}{1-kr^2} + r^2(d\theta^2 + \sin^2\theta d\phi^2)\right] \ , \tag{A.39}$$

with $k = 0, \pm 1$.

## A.5 Dynamics of a Homogeneous, Isotropic Universe

The aim is now to substitute the spacetime metric (A.39) into Einstein's equation (A.7) to obtain predictions for the dynamical evolution of the Universe.
The most general form consistent with homogeneity and isotropy $T_{\mu\nu}$ can take is the perfect fluid form

$$T_{\mu\nu} = \rho u_\mu u_\nu + p(g_{\mu\nu} + u_\mu u_\nu) \ , \tag{A.40}$$

where $\rho$ and $p$ are the energy density and pressure (respectively) as measured in the rest frame, and $u^\mu$ is the four-velocity of the fluid. Because of isotropy, in comoving coordinates the four-velocity is

$$u^\mu = (1,0,0,0) \ , \tag{A.41}$$

and the energy-momentum tensor is then

$$T_{\mu\nu} = \begin{pmatrix} \rho & 0 & 0 & 0 \\ 0 & & & \\ 0 & & g_{\mu\nu}p & \\ 0 & & & \end{pmatrix} \ . \tag{A.42}$$

For matter (baryons and cold dark matter) $p = 0$, for radiation (photons and relativistic particles) $p = \rho/3$.
The task is to compute $G_{\mu\nu}$ from the metric (A.39) and equating it to $8\pi G T_{\mu\nu}$. A priori, 10 equations corresponding to the 10 independent components of a symmetric two-index tensor. However, on account of the spacetime symmetries, only two independent equations. Actually, "time-space" components of Einstein's equation are identically zero, off-diagonal "space-space" components must vanish, and the diagonal "space-space" components yield the same equations. Hence the independent components of Einstein's equation are simply

$$G_{tt} = 8\pi G T_{tt} = 8\pi G T_{00} = 8\pi G\rho \ , \tag{A.43}$$
$$G_{**} = 8\pi G T_{**} = 8\pi G a^{-2} T_{xx} = 8\pi G p \ , \tag{A.44}$$

where $G_{tt} = G_{\mu\nu}u^\mu u^\nu$ and $G_{**} = G_{\mu\nu}s^\mu s^\nu$, where $s^\mu$ is a unit vector tangent to the homogeneous hypersurfaces,

$$s^\mu = \frac{1}{a\sqrt{3}}(0,1,1,1) \ . \tag{A.45}$$

We can compute $G_{tt}$ and $G_{**}$ in terms of $a(t)$ using the coordinate basis components of the Christoffel symbol

$$\Gamma^c{}_{ab} = \frac{1}{2}\sum_d g^{cd}\left\{\frac{\partial g_{bd}}{\partial x^a} + \frac{\partial g_{ad}}{\partial x^b} - \frac{\partial g_{ab}}{\partial x^d}\right\} \ . \tag{A.46}$$

The nonvanishing components of the Christoffel symbol are merely

$$\Gamma^t{}_{xx} = \Gamma^t{}_{yy} = \Gamma^t{}_{zz} = a\dot{a} \ , \tag{A.47}$$

$$\Gamma^x{}_{xt} = \Gamma^x{}_{tx} = \Gamma^y{}_{yt} = \Gamma^y{}_{ty} = \Gamma^z{}_{zt} = \Gamma^z{}_{tz} = \frac{\dot{a}}{a} \ . \tag{A.48}$$

Indeed

$$\begin{aligned}
\Gamma^t{}_{xx} &= \frac{1}{2}\sum_d g^{td}\left\{\frac{\partial g_{xd}}{\partial x^x}+\frac{\partial g_{xd}}{\partial x^x}-\frac{\partial g_{xx}}{\partial x^d}\right\}= \\
&= \frac{1}{2}g^{tt}\left\{\frac{\partial g_{xt}}{\partial x^x}+\frac{\partial g_{xt}}{\partial x^x}-\frac{\partial g_{xx}}{\partial x^t}\right\}= \\
&= -\frac{1}{2}g^{tt}\frac{\partial g_{xx}}{\partial x^t}= \\
&= \frac{1}{2}\frac{\partial a^2(t)}{\partial t}=a\dot{a}\ ,
\end{aligned}$$

where the dot denotes the derivative with respect to the proper time $t$, *i.e.* $\dot{a}=da/dt$, and

$$\begin{aligned}
\Gamma^x{}_{xt} &= \frac{1}{2}\sum_d g^{xd}\left\{\frac{\partial g_{td}}{\partial x^x}+\frac{\partial g_{xd}}{\partial x^t}-\frac{\partial g_{xt}}{\partial x^d}\right\}= \\
&= \frac{1}{2}g^{xx}\left\{\frac{\partial g_{tx}}{\partial x^x}+\frac{\partial g_{xx}}{\partial x^x}-\frac{\partial g_{xt}}{\partial x^x}\right\}= \\
&= \frac{1}{2}g^{xx}\frac{\partial g_{xx}}{\partial x^t}= \\
&= \frac{1}{2}a^{-2}(t)\frac{\partial a^2(t)}{\partial t}=\frac{\dot{a}}{a}\ .
\end{aligned}$$

Hence, by

$$\begin{aligned}
R_{ac} &= \sum_b R_{abc}{}^b= \\
&= \sum_b \frac{\partial}{\partial x^b}\Gamma^b{}_{ac}-\frac{\partial}{\partial x^a}\left(\sum_b\Gamma^b{}_{bc}\right)+\sum_{e,b}\left(\Gamma^e{}_{ac}\Gamma^b{}_{eb}-\Gamma^e{}_{bc}\Gamma^b{}_{ea}\right) \qquad \text{(A.49)}
\end{aligned}$$

the independent Ricci tensor components are calculated to be

$$R_{tt}=-3\frac{\ddot{a}}{a}\ , \qquad \text{(A.50)}$$

$$R_{**}=a^{-2}R_{xx}=\frac{\ddot{a}}{a}+2\frac{\dot{a}^2}{a^2}\ . \qquad \text{(A.51)}$$

Indeed

$$\begin{aligned}
R_{tt} &= \sum_b \frac{\partial}{\partial x^b}\Gamma^b{}_{tt}-\frac{\partial}{\partial x^t}\left(\sum_b\Gamma^b{}_{bt}\right)+\sum_{e,b}\left(\Gamma^e{}_{tt}\Gamma^b{}_{eb}-\Gamma^e{}_{bt}\Gamma^b{}_{et}\right)= \\
&= -\frac{\partial}{\partial x^t}\left(\sum_x\Gamma^x{}_{xt}\right)+\sum_x\left(-\Gamma^x{}_{xt}\Gamma^x{}_{xt}\right)= \\
&= -3\frac{\partial}{\partial x^t}\Gamma^x{}_{xt}-3\Gamma^x{}_{xt}\Gamma^x{}_{xt}= \\
&= -3\frac{\partial}{\partial t}\frac{\dot{a}}{a}-3\frac{\dot{a}^2}{a^2}= \\
&= -3\frac{\ddot{a}a-\dot{a}^2}{a^2}-3\frac{\dot{a}^2}{a^2}=-3\frac{\ddot{a}}{a}\ ,
\end{aligned}$$

where $\ddot{a} = d\dot{a}/dt$, and

$$\begin{aligned} R_{xx} &= \sum_b \frac{\partial}{\partial x^b}\Gamma^b{}_{xx} - \frac{\partial}{\partial x^x}\left(\sum_b \Gamma^b{}_{bx}\right) + \sum_{e,b}\left(\Gamma^e{}_{xx}\Gamma^b{}_{eb} - \Gamma^e{}_{bx}\Gamma^b{}_{ex}\right) = \\ &= \sum_b \frac{\partial}{\partial x^b}\Gamma^b{}_{xx} + \sum_b\left(\Gamma^t{}_{xx}\Gamma^b{}_{tb} - \Gamma^t{}_{bx}\Gamma^b{}_{tx}\right) + \sum_b\left(\Gamma^x{}_{xx}\Gamma^b{}_{xb} - \Gamma^x{}_{bx}\Gamma^b{}_{xx}\right) = \\ &= \frac{\partial}{\partial x^t}\Gamma^t{}_{xx} + 3\Gamma^t{}_{xx}\Gamma^x{}_{tx} - \Gamma^t{}_{xx}\Gamma^x{}_{tx} - \Gamma^x{}_{tx}\Gamma^t{}_{xx} = \\ &= \frac{\partial}{\partial t}(a\dot{a}) + a\dot{a}^2\frac{\dot{a}}{a} = \\ &= \dot{a}^2 + a\dot{a} + \dot{a}^2 = a\dot{a} + 2\dot{a}^2 \ . \end{aligned}$$

Since

$$R = -R_{tt} + 3R_{**} = 6\left(\frac{\ddot{a}}{a} + \frac{\dot{a}^2}{a^2}\right) \ , \tag{A.52}$$

thus

$$G_{tt} = R_{tt} + \frac{1}{2}R = 3\frac{\dot{a}^2}{a^2} = 8\pi G\rho \ , \tag{A.53}$$

$$G_{**} = R_{**} - \frac{1}{2}R = -2\frac{\ddot{a}}{a} - \frac{\dot{a}^2}{a^2} = 8\pi G p \ . \tag{A.54}$$

Using (A.53), (A.54) can be rewritten as

$$3\frac{\ddot{a}}{a} = -4\pi G(\rho + 3p) \ . \tag{A.55}$$

Repeating the calculation for the cases of spherical and hyperboloid geometries, the general evolution equations for homogeneous, isotropic cosmology (*Friedmann equations*) are:

$$\frac{\dot{a}^2}{a^2} = \frac{8\pi G}{3}\rho - \frac{k}{a^2} \ , \tag{A.56}$$

$$\frac{\ddot{a}}{a} = -\frac{4\pi G}{3}(\rho + 3p) \ , \tag{A.57}$$

where $k = +1$ for the 3-sphere, $k = 0$ for flat space, and $k = -1$ for the hyperboloid. Defining the *Hubble constant*

$$H(t) \equiv \frac{\dot{a}}{a} \ , \tag{A.58}$$

the Friedmann equations (A.56) and (A.57) can be expressed by

$$H^2 = \frac{8\pi G}{3}\rho - \frac{k}{a^2} \ , \tag{A.59}$$

$$\dot{H} + H^2 = -\frac{4\pi G}{3}(\rho + 3p) \ . \tag{A.60}$$

Introducing the *critical density*

$$\rho_c \equiv \frac{3H^2}{8\pi G} \ , \tag{A.61}$$

and the *density parameter*

$$\Omega \equiv \frac{\rho}{\rho_c} \ , \tag{A.62}$$

the Friedmann equation (A.59) can be rewritten

$$\frac{k}{a^2} = H^2(\Omega - 1) \ , \tag{A.63}$$

and the space is closed ($k = 1$), flat ($k = 0$) or open ($k = -1$) according to whether $\Omega$ is greater than, equal to, or less than unity.
Since $k$ is constant,

$$a^2H^2(\Omega - 1) = a_0^2H_0^2(\Omega_0 - 1) \ , \tag{A.64}$$

where $a_0$, $H_0$, and $\Omega_0$ are the present-day values of $a$, $H$, and $\Omega$ respectively.

## A.6 Perfect Fluid Models

A perfect fluid, described by the energy-momentum tensor (A.40), forms the basis of the Friedmann models. In order to study the cosmological solutions for homogeneous, isotropic cosmology, one needs to specify an equation of state for the fluid in the form $p = p(\rho)$. In general,

$$p = w\rho \ . \tag{A.65}$$

Actually, $p$ and $\rho$ appearing in (A.40) are the sum of the pressures and densities of the different components of the cosmological fluid respectively, *i.e.*

$$p = \sum_i p_i \ , \tag{A.66}$$

$$\rho = \sum_i \rho_i \ , \tag{A.67}$$

where $p_i$ is the pressure and $\rho_i$ the density of the $i$-th component.
Each component has its own equation of state

$$p_i = w_i \rho_i \ . \tag{A.68}$$

If the evolution of the Universe is adiabatic, *i.e.*

$$d(\rho a^3) = -p da^3 \ , \tag{A.69}$$

then

$$a^3 d\rho = -(\rho + p) da^3 = a^3 d(\rho + p) - d\left[(\rho + p) a^3\right] \ , \tag{A.70}$$

and

$$a^3 \frac{dp}{dt} = -\frac{d\left[(\rho + p) a^3\right]}{dt} \ , \tag{A.71}$$

which can also be expressed as

$$\dot{\rho} + 3H(\rho + p) = 0 \ . \tag{A.72}$$

Using (A.65), the *continuity equation* (A.72) can be rewritten as

$$\dot{\rho} + 3\frac{\dot{a}}{a}\rho(1 + w) = 0 \ . \tag{A.73}$$

Integrating (A.73), we find

$$\rho = \rho_0 \exp\left[-3 \int_{a_0}^{a} \frac{1 + w}{a'} da'\right] \ , \tag{A.74}$$

being $\rho_0$ and $a_0$ the present-day values of $\rho$ and $a$, respectively.
For matter ($w_m = 0$) $\rho_m a^3 = \text{const.} = \rho_{0m} a_0^3$, for radiation ($w_r = 1/3$) $\rho_r a^4 = \text{const.} = \rho_{0r} a_0^4$.
Defining the density parameter for each component

$$\Omega_i \equiv \frac{\rho_i}{\rho_c} \ , \tag{A.75}$$

the Friedmann equation (A.59) can be rewritten

$$H^2 = H_0^2 \left[\sum_i \Omega_{0i} \exp\left(-3 \int_{a_0}^{a} \frac{1 + w_i(a')}{a'} da'\right) + \left(\frac{a_0}{a}\right)^2 (1 - \sum_i \Omega_{0i})\right] \ , \tag{A.76}$$

where $\Omega_{0i}$ is the present-day value of $\Omega_i$.
In terms of redshift $z$ and cosmic time $t$

$$z = \frac{a_0}{a} - 1 \ , \tag{A.77}$$

$$dt = -\frac{dz}{H_0 E_z (1+z)} \ , \tag{A.78}$$

where

$$\begin{aligned} E_z &= \frac{H}{H_0} = \\ &= \left[ \sum_i \Omega_{0i} \exp\left( 3 \int_0^z \frac{1+w_i(z')}{1+z'} dz' \right) + (1+z)^2 (1 - \sum_i \Omega_{0i}) \right]^{1/2} . \end{aligned} \tag{A.79}$$

# Bibliography


Abell G. O., 1958, ApJS, 3, 211

Acquaviva V., Baccigalupi C., Leach S. M., Liddle A. R., Perrotta F., 2005, Phys. Rev. D, 71, 104025

Allen S. W., et al., 2008, MNRAS, 383, 879

Allen S. W., Evrard A. E., Mantz A. B., 2011, ARAA, 49, 409

Allen S. W., Schmidt R. W., Ebeling H., Fabian A. C., van Speybroeck L., 2004, MNRAS, 353, 457

Allgood B., et al., 2006, MNRAS, 367, 1781

Amendola L., 2000, Phys. Rev. D, 62, 043511

Amendola L., Tsujikawa S., 2010, Dark Energy: Theory and Observations

Arnaud M., Pointecouteau E., Pratt G. W., 2007, A&A, 474, L37

Baldi M., 2011, MNRAS, 411, 1077

Baldi M., Pettorino V., 2011, MNRAS, 412, L1

Baldi M., Pettorino V., Robbers G., Springel V., 2010, MNRAS, 403, 1684

Bartelmann M., 2010, Classical and Quantum Gravity, 27, 233001

Bertotti B., Iess L., Tortora P., 2003, Nature, 425, 374

Bhattacharya S., Habib S., Heitmann K., 2011, ArXiv e-prints

Bianchi E., Rovelli C., 2010, arXiv:1002.3966

Blumenthal G. R., Faber S. M., Flores R., Primack J. R., 1986, ApJ, 301, 27

Boisseau B., Esposito-Farèse G., Polarski D., Starobinsky A. A., 2000, Physical Review Letters, 85, 2236

Borgani S., 2006, arXiv:0605575

Borgani S., et al., 2004, MNRAS, 348, 1078

Borgani S., Kravtsov A., 2009, arXiv:0906.4370

Bryan G. L., Norman M. L., 1998, ApJ, 495, 80

Bullock J. S., et al., 2001, MNRAS, 321, 559

Buote D. A., et al., 2007, ApJ, 664, 123

Cavaliere A., Fusco-Femiano R., 1976, A&A, 49, 137

Clifton T., Barrow J. D., Scherrer R. J., 2005, Phys. Rev. D, 71, 123526

Comerford J. M., Natarajan P., 2007, MNRAS, 379, 190

David L. P., Jones C., Forman W., 1995, ApJ, 445, 578

De Boni C., Bertin G., 2008, Nuovo Cimento B Serie, 123, 31

De Boni C., et al., 2011, MNRAS, 415, 2758

Dolag K., Borgani S., Schindler S., Diaferio A., Bykov A. M., 2008, SSR, 134, 229

Dolag K., et al., 2004, A&A, 416, 853

Duffy A. R., et al., 2010, MNRAS, 405, 2161

Duffy A. R., Schaye J., Kay S. T., Dalla Vecchia C., 2008, MNRAS, 390, L64

Eke V. R., Navarro J. F., Steinmetz M., 2001, ApJ, 554, 114

Ettori S., Dolag K., Borgani S., Murante G., 2006, MNRAS, 365, 1021

Ettori S., et al., 2004, MNRAS, 354, 111

Ettori S., et al., 2009, A&A, 501, 61

Ettori S., et al., 2010, A&A, 524, A68

Fedeli C., 2011, arXiv:1111.5780

Frenk C. S., White S. D. M., Davis M., Efstathiou G., 1988, ApJ, 327, 507

Gao L., et al., 2008, MNRAS, 387, 536

Gehrels N., 1986, ApJ, 303, 336

Giacconi R., et al., 2009, in Astro2010: The Astronomy and Astrophysics Decadal Survey, Science White Papers, no. 90, Galaxy clusters and the cosmic cycle of baryons across cosmic times, preprint (arXiv:0902.4857)

Giodini S., et al., 2009, ApJ, 703, 982

Gonzalez A. H., Zaritsky D., Zabludoff A. I., 2007, ApJ, 666, 147

Haardt F., Madau P., 1996, ApJ, 461, 20

Hammer F., Rigaut F., 1989, A&A, 226, 45

Hu W., Kravtsov A. V., 2003, ApJ, 584, 702

Hu W., Sawicki I., 2007, Phys. Rev. D, 76, 064004

Jarosik N., et al., 2011, ApJS, 192, 14

Jenkins A., et al., 2001, MNRAS, 321, 372

Jennings E., Baugh C. M., Angulo R. E., Pascoli S., 2010, MNRAS, 401, 2181

Jing Y. P., 2000, ApJ, 535, 30

Jing Y. P., Suto Y., 2002, ApJ, 574, 538

Jones C., Forman W., 1984, ApJ, 276, 38

King I., 1962, AJ, 67, 471

Klypin A. A., Trujillo-Gomez S., Primack J., 2011, ApJ, 740, 102

Kravtsov A. V., Vikhlinin A., Nagai D., 2006, ApJ, 650, 128

Li B., Mota D. F., Barrow J. D., 2011, ApJ, 728, 109

Macciò A. V., Dutton A. A., van den Bosch F. C., 2008, MNRAS, 391, 1940

Macciò A. V., Quercellini C., Mainini R., Amendola L., Bonometto S. A., 2004, Phys. Rev. D, 69, 123516

Moore B., Quinn T., Governato F., Stadel J., Lake G., 1999, MNRAS, 310, 1147

Mota D. F., Pettorino V., Robbers G., Wetterich C., 2008, Physics Letters B, 663, 160

Muñoz-Cuartas J. C., Macciò A. V., Gottlöber S., Dutton A. A., 2011, MNRAS, 411, 584

Navarro J. F., et al., 2010, MNRAS, 402, 21

Navarro J. F., Frenk C. S., White S. D. M., 1996, ApJ, 462, 563

Neto A. F., et al., 2007, MNRAS, 381, 1450

Oguri M., et al., 2012, MNRAS, p. 2189

Oyaizu H., Lima M., Hu W., 2008, Phys. Rev. D, 78, 123524

Perlmutter S., et al., 1999, ApJ, 517, 565

Perrotta F., Baccigalupi C., Matarrese S., 2000, Phys. Rev. D, 61, 023507

Pettorino V., Baccigalupi C., 2008, Phys. Rev. D, 77, 103003

Pettorino V., Baccigalupi C., Perrotta F., 2005, Journal of Cosmology and Astro-Particle Physics, 12, 3

Prada F., Klypin A. A., Cuesta A. J., Betancort-Rijo J. E., Primack J., 2011, arXiv:1104.5130

Pratt G. W., Croston J. H., Arnaud M., Böhringer H., 2009, A&A, 498, 361

Predehl P., et al., 2007, in Society of Photo-Optical Instrumentation Engineers (SPIE) Conference Series Vol. 6686 of Presented at the Society of Photo-Optical Instrumentation Engineers (SPIE) Conference, eROSITA

Press W. H., Schechter P., 1974, ApJ, 187, 425

Puchwein E., Sijacki D., Springel V., 2008, ApJ, 687, L53

Ratra B., Peebles P. J. E., 1988, Phys. Rev. D, 37, 3406

Riess A. G., et al., 1998, AJ, 116, 1009

Ryden B. S., Gunn J. E., 1987, ApJ, 318, 15

Salpeter E. E., 1955, ApJ, 121, 161

Schechter P., 1976, ApJ, 203, 297

Schmidt F., Lima M., Oyaizu H., Hu W., 2009, Phys. Rev. D, 79, 083518

Schmidt R. W., Allen S. W., 2007, MNRAS, 379, 209

Sheth R. K., Mo H. J., Tormen G., 2001, MNRAS, 323, 1

Sheth R. K., Tormen G., 1999, MNRAS, 308, 119

Smith S., 1936, ApJ, 83, 23

Spergel D. N., et al., 2007, ApJS, 170, 377

Springel V., 2005, MNRAS, 364, 1105

Springel V., et al., 2005, Nature, 435, 629

Springel V., Hernquist L., 2002, MNRAS, 333, 649

Springel V., Hernquist L., 2003, MNRAS, 339, 289

Springel V., White M., Hernquist L., 2001, ApJ, 549, 681

Tinker J., Kravtsov A. V., Klypin A., Abazajian K., Warren M., Yepes G., Gottlöber S., Holz D. E., 2008, ApJ, 688, 709

Vikhlinin A., et al., 2006, ApJ, 640, 691

Vikhlinin A., et al., 2009a, ApJ, 692, 1033

Vikhlinin A., et al., 2009b, ApJ, 692, 1060

Voit G. M., 2005, Reviews of Modern Physics, 77, 207

Wald R. M., 1984, General relativity

Weinberg N. N., Kamionkowski M., 2003, MNRAS, 341, 251

Wetterich C., 1988, Nuclear Physics B, 302, 645

Wetterich C., 1995, A&A, 301, 321

White D. A., Fabian A. C., 1995, MNRAS, 273, 72

Wintergerst N., Pettorino V., Mota D. F., Wetterich C., 2010, Phys. Rev. D, 81, 063525

Wojtak R., Łokas E. L., 2010, MNRAS, 408, 2442

Zel'dovich Y. B., 1970, A&A, 5, 84

Zhao H., Macciò A. V., Li B., Hoekstra H., Feix M., 2010, ApJ, 712, L179

Zwicky F., 1933, Helvetica Physica Acta, 6, 110

Zwicky F., 1937, ApJ, 86, 217

# Acknowledgments

I am deeply indebted to Lauro Moscardini and Stefano Ettori for the supervision of this work.

I am thankful to Klaus Dolag for providing access to, and support in using his simulations.

I am grateful to Valeria Pettorino and Carlo Baccigalupi for useful discussions on the models.

I thank Luca Amendola, Marco Baldi, Matthias Bartelmann, Veronica Biffi, Stefano Borgani, Cosimo Fedeli, Margherita Ghezzi, Carlo Giocoli, Amina Helmi, Massimo Meneghetti, Francesco Pace, Elena Rasia and Mauro Roncarelli for useful discussions.

Alexey Vikhlinin and Olga Cucciati are thanked for providing me with their data.

The comments of Carmen De Toffol helped improving the presentation of this work.

Quelli che... I miei genitori e mia nonna, grazie di tutto.

Quelli che... Mafalda.

Quelli che... La seconda lettera dell'alfabeto greco.

Quelli che... Parigi (ma anche Modena) val bene una messa.

Quelli che... Il Principato Autonomo del Rettilario.

Quelli che... Il Bang! (e il ribelle®), The Threemons, Il Nome del Gruppo,
Superida, il pirata zoppo, il PuffTorneo, Brandis Aelar Carric.

Quelli che... Gli amici di Milano (che ci sono sempre, anche quando io non ci sono),
gli amici di Trieste, gli amici di Monaco, gli amici sparsi per il mondo, le amiche.

Quelli che... Sambuca?!, Ah, la tauromachia!, Urca che botta!, Naked in the Lake,
il profumo della mela della Normandia, è un po' impegnativo, la maglia gialla, O Fabuloso,
il volo di ritorno il mese sbagliato, è un momento storico, le scuole, i congressi.

Quelli che... Strano, vai a un concerto?!

Quelli che... Cullati fra i portici cosce di mamma Bologna.

Quelli che... Qual è il gelato più buono di Bologna?

Quelli che... L'Osteria dell'Orsa.

Quelli che... Le compagne e i compagni.

Quelli che... Il mio gatto Birba, che va ancora in cerca di Puffi.

Quelli che... Il Grande Mazinga.